5-2012

Compressive Strength of Continuous Fiber Unidirectional Composites

Ronald Thompson
Clemson University, bartthompson99@gmail.com

COMPRESSIVE STRENGTH OF CONTINUOUS FIBER UNIDIRECTIONAL COMPOSITES

A Dissertation
Presented to
the Graduate School of
Clemson University

In Partial Fulfillment
of the Requirements for the Degree
Doctor of Philosophy
Mechanical Engineering

---

by
Ronald H. Thompson
May 2012

Accepted by:
Dr. Paul Joseph, Committee Chair
Dr. Vincent Blouin
Dr. Sherrill Biggers
Dr. Mica Grujicic
Dr. Timothy Rhyne

ABSTRACT

Dow and Rosen's work in 1965 formed an intellectual framework for compressive strength of unidirectional composites. Compressive strength was explained in terms of micro-buckling, in which filaments are beams on an elastic foundation. They made simplifying assumptions, with a two dimensional idealization and linearized material properties. This study builds on their model, recognizing that the shear mode of instability drives unidirectional compressive strength. As a necessary corollary, the predictive methods developed in this study emphasize correct representation of composite shear stiffness. Non-linear effects related to matrix material properties, fiber misalignment, three dimensional representation, and thermal prestrains are taken into account.

Four work streams comprise this study: first, development of a closed form analytical model; second, empirical methods development and model validation; third, creation and validation of a unit cell finite element model; and fourth, a patent application that leverages knowledge gained from the first three work streams.

The analytical model characterizes the non-linearity of the matrix both with respect to shear and compressive loading. This improvement on existing analyses clearly shows why fiber modulus affects composite shear instability. Accounting for fiber misalignment in the model and experimental characterization of the fiber misalignment continuum are important contributions of this study.

A simple method of compressive strength measurement of a small diameter monofilament glass-resin composite is developed. Sample definition and preparation are original, and necessary technologies are easily assessable to other researchers in this field. This study shows that glass fiber composites have the potential for high compressive strength. This potential is reached with excellent fiber alignment and suitable matrix characteristics, and results are consistent with model predictions.

The unit cell three dimensional finite element model introduces a boundary condition that only allows compressive and shear deformation, thus recognizing the actual deformation mechanism of a compressed unidirectional composite. A new approach for representing the resin matrix is employed, giving improved correlation to empirical measurements noted in the literature. A method of accounting for realistic composite imperfections is introduced.

The patent application work was fed by results from the first three areas. A new engineering structure is created in which buckling is beneficial. Post buckled behavior favorably affects other structural components in an overload situation.

The first three work streams form a coherent unit and are mutually supportive. The analytical model predictions are corroborated by the experimental measurements. Finite element model predictions are consistent with the analytical model predictions.

DEDICATION

Technology is created by combining the laws of science with the laws of mathematics. This is the mandate God gave mankind when He commanded "Subdue the earth." Technology showcases man's mastery of nature.

From such a perspective, this study represents simple obedience to God. In a very limited sense, my hope is that this study enables further technological conquest in the field of composites.

ACKNOWLEDGEMENTS

Many wonderful people have teamed to make this dissertation a reality. My advisor Dr. Paul Joseph has given spot-on management and direction. My committee members, Dr. Timothy Rhyne, Dr. Sherrill Biggers, Dr. Mica Grujicic, and Dr. Vincent Blouin have also given their time and talents. These professors graciously served as the official cadre overseeing this study.

Michelin Tire Corporation generously supported this work. Two Michelin scientists, Jean-Paul Meraldi and Antonio Delfino, were real motors, providing technical insight, advice, and test samples. Steve Cron, Scott Anderson, Zuqing Qu, and Eugene Wang, all of Michelin, extended invaluable assistance.

Owens Corning Corporation and Dassault Systemes Simulia Corporation provided testing resource and software guidance, respectively. I am especially appreciative to Dr. Ronit Kar Gupta of Simulia for his help.

My father and mother, Dr. Ron and Peggy Thompson were also strong supporters. My father has patiently waited for the day I would go back to school for that terminal degree.

A group of ladies meet on Friday mornings at Grace Baptist Church of Taylors to pray for college students. They prayed for me.

Finally, my family believed in me. Karina, my wife, never wavered in her encouragement. Anna, Nicole, and Christina, my three daughters, consistently expressed confident in my eventual success.

TABLE OF CONTENTS

Page

LIST OF TABLES

LIST OF FIGURES

List of Figures (Continued)

List of Figures (Continued)

List of Figures (Continued)

List of Figures (Continued)

CHAPTER ONE

PREFACE

Study scope

A composite material consists of at least two constituent materials with material properties that are typically significantly different. These constituent materials remain discernibly separate yet bonded together in the finished composite product. The individual constituents may have dimensions that are microscopic or macroscopic in scale. The engineering goal of a composite material is the creation of a new material that has one or more particular properties (density, stiffness, strength, or price) superior to that attainable with a single homogenous material.

The field of composite materials dates from antiquity. One ancient piece of literature that describes a composite material is the book of Exodus in the Bible. Reference is made to Hebrew slaves making bricks reinforced with straw, and then being forced to make bricks without straw.[1] The straw served as a fabrication aid, facilitating brick bonding and molding. Ancient Egyptian art depicts this process.

Modern composites began to come of age in the second half of the 20th century as carbon, glass, and Kevlar fibers entered commercial aviation and automotive markets. Rapid improvement in material properties and manufacturing techniques was achieved in this time period. For example, the

tensile stiffness of graphite fibers was 150 GPa when they entered the market in the early 1980s, and had reached 500+ GPa in the early 1990s.[2] Progress continues, pushed in part by the need for lower cost, lower mass structures in transportation industries.

This study applies to a small segment of the world of composites. Two composite families are investigated, with the particular research goal being comprehension and optimization of compression properties. Then, a practical study goal is addressed; the use of a specific composite as an element in a novel engineering structure.

The two general composite families studied are as follows:

- **Continuous Fiber Unidirectional Laminate Classic Composite**

In this study, "classic composite" defines the matrix material as having an elastic modulus $1/10^{th}$ to $1/100^{th}$ that of the fiber. Common matrix materials include thermoset and thermoplastic resins. Only thermoset resins are considered here, yet the principles developed apply to thermoplastic matrix materials also.

This study considers only continuous high performance fibers, which implies the use of high modulus and strength fibers such as boron, glass, and carbon. The most common employ of these materials is in laminate construction, in which thin layers (lamina) of unidirectional fiber are impregnated in a matrix material. This is known as "prepreg." A unidirectional laminate consists of multiple lamina of identical fiber direction. Bonding of lamina involves the

pressurized cure of the resin using an autoclave molding process[3]. Ideally, this geometry gives a transversally isotropic cross-section. In reality, a very thin layer of isotropic resin exists between each individual lamina.

- **Pultruded Monofilament Classic Composite**

"Monofilament" in this context is a reinforcement which has a monolithic cross section, with a transverse cross section on the order of 1 mm^2. It is manufactured in a continuous process, during which the fibers are under tension. Fibers pass though a resin bath and then through a die that defines the cross section shape. Resin polymerization occurs in-line immediately afterwards.[4]

A monofilament is neither a cord nor a cable. A cable consists of several isotropic cross-sections (with diameters on the order of 0.2 mm) having a twisted structure. Cables are often made of metallic materials. A cord consists of a large number of twisted fibers of small diameter (on the order of microns). Cords are made from organic compounds, such as polyester, aramid, and nylon.

A pultruded composite may have the same constituents as a laminate composite; i.e., the same fiber, fiber volume fraction, and matrix material. However, it may have different mechanical properties due to: (a) improved fiber alignment of the pultrusion process, and (b) the absence of interlaminar effects. This study addresses these effects as they relate to compressive strength.

This research was in part sponsored by Michelin Tire Corporation. Appropriately, the study has an applied research goal – the use of a classical composite as reinforcement in a large-deformation elastomeric structure.

Pneumatic tires, conveyor belts, and automotive V-belts are examples of engineering structures having cords, cables, and/or monofilaments as reinforcements, with elastomeric matrix materials. Comprehension of composite compressive properties gained in this research was used to create a patent application involving the use of a classical composite in an engineering structure. A real-world design challenge was addressed, with solutions developed.

Organization of this Dissertation

This dissertation consists of theoretical and experimental study of compressive strength of unidirectional classical composites, and the use of a classical composite in an elastomeric engineering structure. Chapter 2 provides a literature review of classical composite constituents and compressive behavior. Chapters 3 through 5 represent three independent manuscripts formatted for publication in scientific journals. While some redundancy of material was necessary, these chapters generally fit together as follows: Chapter 3 relates primarily to closed-form theory development and implementation in a mathematical model; Chapter 4 serves as a further confirmation of Chapter 3 by comparing experimental data to theory predictions; and Chapter 5 uses insights from Chapter 3 to develop micromechanical finite element modeling procedures. Finally, Chapter 6 contains general information pertaining to a patent application filed by Michelin Tire Corporation. As the patent had not published at the date of defense of this dissertation, the author was not authorized to disclose detailed

information. However, the spirit of the application and its relevance to knowledge gained in Chapters 3 - 5 are shown.

References

[1] The Bible. Exodus 5 :6-18.

[2] Grandidier, J-C, Ferron, G., Potier-Ferry, M. (1992). Microbucking and Strength in Long Fiber Composites: Theory and Experiments. *International Journal of Solids and Structures, Vol 29*, No. 14, pp 1753-1761.

[3]Daniel, I.M., Ishai, O. (2006*). Engineering Mechanics of Composite Materials, 2nd Ed.*, Oxford University Press, Inc., New York, pp. 35-39.

[4] Meyer, R. (1985). *Handbook of Pultrusion Technology*. Chapman and Hall, New York.

CHAPTER TWO

CLASSICAL COMPOSITE CHARACTERISTICS

Classical composites are well described in technical papers and in standard composite textbooks[1] as are constituent materials and current fabrication techniques.[2] [3] [4] There is no value in any broad treatise of these subjects. Rather, the goal of this section is to examine crucial characteristics of a classical composite as they relate to compression behavior.

Reinforcement Characteristics

Morphology of aramid and carbon fibers are broadly discussed in the literature and in composite handbooks[5] [6]. Particularly, aramid fiber molecular structure is identified as a culprit for observed poor compression behavior, with its high anisotropy and low shear stiffness and strength identified as fundamental to the observed poor compression performance.[7]

Carbon fiber morphology is also covered[8] with the degree of anisotropy correlated to extensional modulus. While having less orientation than aramid, carbon fiber exhibits a type of layering, similar to the layering of an onion skin. Different layers can also have differing degrees of axial orientation. This anisotropy can play a negative role in compression.

Conversely, glass fiber morphology sees little discussion in the literature. Glass fiber morphology discussion really must begin with a discussion of the chemistry of glass itself. The following overview was compiled from on-line sources.[9] [10]

Many solids have a crystalline structure on microscopic scales. The molecules are arranged in a regular lattice, as in Figure 2.1a. As the solid is heated the molecules vibrate about their position in the lattice until, at the melting point, the crystal breaks down and the materials begin to flow on a molecular level. There is a sharp distinction between the solid and the liquid state that is separated by a *first order phase transition*, i.e. a discontinuous change in the properties of the material such as density.

A liquid has *viscosity*, a measure of its resistance to flow. As a liquid is cooled its viscosity normally increases, but viscosity also has a tendency to prevent crystallisation. Usually when a liquid is cooled to below its melting point, crystals form and it solidifies; but sometimes the liquid can become *supercooled* and remain liquid below its melting point because there are no nucleation sites to initiate the crystallisation. If the viscosity rises enough as it is cooled further, the liquid may never crystallise. The viscosity rises rapidly and continuously, leading eventually to an **amorphous solid.** The molecules then have a disordered

a Molecular arrangement in a crystal

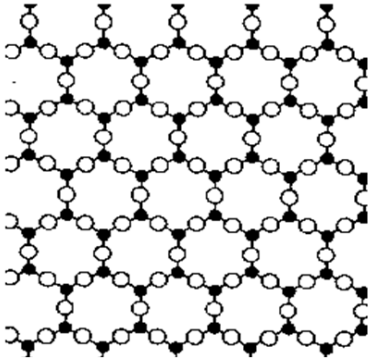

b Molecular arrangement in a glass

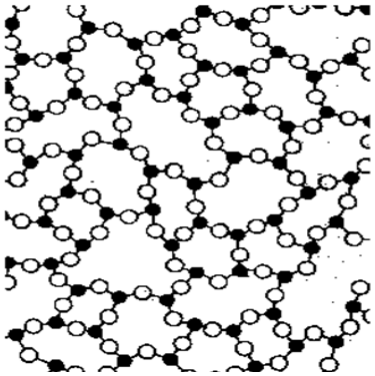

Figure 2.1: Molecular arrangement in crystals and glasses

arrangement, but sufficient cohesion to maintain some rigidity. In this state it is often called an amorphous solid or glass, with a molecular structure as shown in Figure 2.1b.

Glass could theoretically be considered a supercooled liquid because there is no first order phase transition as it cools. Yet, there is a *second order transition* between the supercooled liquid state and the glass state, so a distinction can be drawn. The transition is not as dramatic as the phase change that takes you from liquid to crystalline solids. There is no discontinuous change of density and no latent heat of fusion. The transition can be detected as a marked change in the thermal expansion and heat capacity of the material.

The situation at the level of molecular physics can be summarised by saying that there are three main types of molecular arrangement:

1. crystalline solids: molecules are ordered in a regular lattice
2. fluids: molecules are disordered and are not rigidly bound.
3. glasses: molecules are disordered but are rigidly bound.

The above morphological framework of understanding materials is extremely valuable in understanding macroscopic material properties. “Solids, liquids and gases” are really only ideal behaviours characterised by properties such as compressibility, viscosity, elasticity, strength and hardness. Real materials don't always behave according to such ideals.

Glass (rather, SiO_2) is one case in point. There is no clear answer to the question "Is glass solid or liquid?" In terms of molecular dynamics and

thermodynamics it is possible to justify various different views that it **is a highly viscous liquid, an amorphous solid (falling in category 3 above), or simply that glass is another state of matter that is neither liquid nor solid**.

The fact that glass does have the amorphous structure of Figure 2.1b results in *significant molecular mobility*. This mobility comes from the fact that glass has a very high viscosity and yet simultaneously has the ability to create molecular bonding. Fundamentally, glass should be capable of both high tensile and high compressive strains.

Glass fiber has elongation to break of between 4.5% to 5.5%, while carbon fibers vary from 1.5% to 1.8%. Boron fiber has elongation to break of about 0.9%. In terms of ultimate tensile strength, glass, boron, and carbon are roughly equivalent. The differences in elongation to break thus relate to differences in modulus.[11] Conversely, glass composite compressive strength has been measured to be significantly lower than that of both boron and carbon. This result is inconsistent with tensile results, and is also inconsistent with what is known about the morphology of glass itself.

Matrix Characteristics

Matrix material properties and choice criteria, such as modulus, ultimate elongation to break, and thermal characteristics, are covered extensively in the literature, in handbooks, and now in on-line sources. There is no need for in-depth treatment of this readily available data. However, the resins most

commonly used for classic composites will be considered, and properties that might impact compression behavior will be noted.

Epoxy resins are used extensively in composite materials, and are the most versatile of the commercially available matrix materials.[12] Epoxy resins have a broad range of physical properties, mechanical capabilities, and processing conditions. Although polyester and vinyl ester resins cost less, they provide somewhat inferior material properties. For example, the strain to break of a typical polyester resin is around 3%; a vinyl ester resin is around 4.5%, and epoxy resins can have as high as a 7% elongation to break.[13] In addition to reduced toughness, polyester and vinyl ester resins also have somewhat lower adhesive properties and micro-cracking resistance.

In general, for optimal composite performance, the mechanical properties of the resin should be chosen relative to the mechanical properties of the fiber. Resin tensile elongation to break should be at least as high as that of the reinforcement, although there are special cases in which the fibers provide stiffness only and will not see high ultimate stress levels. As an example, the high elongation to break of glass fiber can be fully exploited only with a suitable resin. Thus, glass fiber composites benefit more from a matrix material having a high elongation to break than would carbon or boron fiber composites.

Resin property influence on unidirectional continuous fiber composite compression characteristics is less obvious. However, as will be introduced in the next section and discussed in detail in Chapters 3 – 5, resin properties are

first order for compressive strength. Resin shear modulus, elongation to break, and uniaxial stress vs. strain non-linearity each play significant roles. The impact of each of these matrix material parameters depends on variables associated with the fiber, such as volume fraction, alignment, modulus, and strength.

Composite Compression Characteristics

Improved tensile behavior is the hallmark added value for much of the composite world. Indeed for many engineering structures, such as pressure vessels, loadings are predominately tensile. In this context, it is generally recognized that compression behavior and comprehension has tended to lag behind the advances in tensile performance.[14]

Handbook values for compression modulus and strength are generally lower that those reported for tension.[15] [16] [17] [18] What reasons are given in the literature for this observed performance? In 1965, pioneering work by Rosen *et al*.[19] idealized fibers as columns, held together by the shear stiffness of the matrix. Applying stability equations developed by Timoshenko[20], Rosen suggested a shear-induced microbuckling as the fundamental cause for degraded compressive modulus. Composite in-plane shear modulus was identified as the primary driver for compressive strength.

Rosen's theoretical result, however, overpredicted compressive strength. Since that time, researchers have advanced several explanations. More current references in the literature point to the role that small imperfections, such as fiber misalignment, play in the formation of kink bands[21] and microbuckling[22] [23]. Still

other references apply a combination of theory and curve-fitting to experimental data to predict compressive strength[24], while at least one composites textbook attributes the higher compressive strength of boron to higher fiber bending stiffness[25].

Complementary to Rosen, yet another theory applies measured fiber misalignment and measured in-plane composite shear stiffness to the prediction of compressive strength[26]. While quite simple in implementation, the theory has given good results when fiber misalignments are large and uniform. [27]

Finally, a recent paper has looked at this problem from another perspective, proposing a three-phase model to explain observed compression strength values for boron, carbon and glass composites.[28] The study assumed that a thin region of resin (denoted as “Interphase”) around the fibers has a lower modulus. If this region were to have a thickness of around 0.1 micrometers and a modulus that was 1/25th of the matrix modulus, the theoretical buckling stress would more closely match experimental results from the literature. Boron composite compressive strength (1.4 GPa), carbon (1.2 GPa) and glass (0.6 GPa) are somewhat better matched with this theory.

A straightforward mechanical consideration argues against this explanation, however. Composites using large diameter fibers, such as boron (100 micrometers), would have a much lower volume fraction of the proposed low modulus interphase than would a glass fiber composite (10 micrometers). This would lead to a much lower in-plane shear modulus for the glass composite.

This is not the case: glass and boron composites have roughly equal in-plane shear moduli yet very different compressive strength. The successful theory must explain both these facts simultaneously.

In summary, the literature indicates that composites generally do not perform as well in compression as in tension. Glass fiber composites in particular have low measured compressive strength. Disparate explanations are offered in the literature, including fiber misalignment, in-plane shear modulus nonlinearity, fiber bending stiffness, and a fiber/matrix of lower modulus. A detailed review of these explanations in presented in Chapter 3.

It seems there is a gap in comprehension of the compression behavior of classical composites, particularly for glass-resin composites. This is seen at a morphological level, which suggests that higher compression performance than that reported in the literature is possible. This lack of comprehension perhaps comes from a variety of areas, proposed as follows:

- Focus of composite optimization is often on tension, not compression.
- Glass fiber is considered lower-tech. It has lower performance in stiffness per unit mass than other more recent fibers. Emphasis has not been placed on understanding its compression behavior because there is less market need.
- Matrix elastic strain limit may be poorly chosen relative to the high elongation capability of glass fiber – with potential detriment in tension and compression.

- Resin properties may not be homogeneous, as noted in the three-phase model. However, large differences in interphase and matrix moduli are unlikely, as was earlier discussed.

References

[1] V. Vasilief, E. Morozov (2007). *Advanced Mechanics of Composite Materials*, *1st Ed*. Elsevier LTD.

[2] Deborah D. Chung, L. (1994). *Carbon Fiber Composites*. Butterworth-Heinemann: Oxford.

[3] Dave, R., Loos, A. (1999). *Processing of Composites*. Hanser/Gardner Publications: Cincinnati, OH.

[4]Reinhart, T.J., Clements, L. L. (1987). Introduction to Composites, In *Composites, Volume 1: Engineered Materials Handbook* (pp 27-37). ASM International.

[5] Lee, S. (1993). *Handbook of Composite Reinforcements*. VCH Publishers.

[6] Smith, W.S., Zweben, C. (1987). Properties of Constituent Materials, In *Composites, Volume 1: Engineered Materials Handbook* (pp 45-65). ASM International.

[7] Diefendorf, R.J. (1987). Carbon/Graphite Fibers, In *Composites, Volume 1: Engineered Materials Handbook* (pp 54-56). ASM International.

[8] Smith, W.S., Zweben, C. (1987). Properties of Constituent Materials, In *Composites, Volume 1: Engineered Materials Handbook* (pp 50-51). ASM International.

[9] http://plc.cwru.edu/tutorial/enhanced/files/polymers/orient/Orient.htm.

[10] http://math.ucr.edu/home/baez/physics/General/Glass/glass.html.

[11] Daniel, I.M., Ishai, O. (2006*). Engineering Mechanics of Composite Materials***,** *2nd Ed.,* Oxford University Press, Inc., New York, pg 374.

[12] May, C.A. (1987). Epoxy Resins, In *Composites, Volume 1: Engineered Materials Handbook* (pp 66-67). ASM International.

[13] www.azom.com.

[14] Rosen, B.W. (1987). Analysis of Material Properties, In *Composites, Volume 1: Engineered Materials Handbook* (pp 196-199). ASM International.

[15] May, C.A. (1987). Epoxy Resins, In *Composites, Volume 1: Engineered Materials Handbook* (pg 76). ASM International.

[16] Gay, D. (1991). *Materiaux composites, 3e Edition revue et augmentee*. Editions Hermes.

[17] Lee, S. (1993). *Handbook of Composite Reinforcements*, VCH Publishers.

[18] Jones, R. (1975). *Mechanics of Composite Materials*, McGraw-Hill, New York.

[19] Dow, N.F., Rosen, B.W. (1965). Evaluations of Filament-reinforced Composites for Aerospace Structural Applications. *NASA CR-207*.

[20] Timoshenko, S., Gere, J. (1961). *Theory of Elastic Stability***,** *2d Ed*. McGraw-Hill, New York.

[21] Fleck, N., Deng, L., Budiansky,B. (1995). Prediction of Kink Width in Compressed Fiber Composites. *Journal of Applied Mechanics, 62*, 329-337.

[22] Marissen, R., Brouwer, H. (1999). The Significance of Fibre Microbuckling for the Flexural Strength of a Composite. *Composites Science and Technology, 59*, Issue 3, pp. 327-330.

[23]Grandidier, J-C, Ferron, G., Potier-Ferry, M. (1992). Microbucking and Strength in Long Fiber Composites: Theory and Experiments*. International Journal of Solids and Structures 29*, No. 14, pp 1753-1761.

[24] Lo, K.H., Chim, E.S-M. (1992). Compressive Strength of Unidirectional Composites. *Journal of Reinforced Plastics and Composites, 11*, 838-96.

[25] Lee, S. (1993). *Handbook of Composite Reinforcements*, VCH Publishers, pp. 96-112.

[26] Daniel, I.M., Ishai, O. (2006*). Engineering Mechanics of Composite Materials*, *2nd Ed***.** Oxford University Press, Inc., New York, pp. 107-109.

[27] Cho, J., Chen J.Y., Daniel, I.M. (2007). Mechanical enhancement of carbon fiber/epoxy composites by graphite nanoplatelet reinforcement. *Acta Materialia Inc*., Elsevier Ltd.

[28] Dharan, C., Lin, C. (2007). Longitudinal Compressive Strength of Continuous Fiber Composites. *Journal of Composite Materials*, *41*, 1389.

CHAPTER THREE

CRITICAL COMPRESSIVE STRESS FOR CONTINUOUS FIBER UNIDIRECTIONAL COMPOSITES

Introduction

Since Rosen and Dow[1] proposed unidirectional composite microbuckling in 1965, researchers have searched for a comprehensive method by which to estimate compressive strength of unidirectional composites. Noting that Rosen and Dow's model over-estimated compressive strength, other models have been proposed that: assume highly localized microbuckling of fibers[2], fiber/matrix bond failure[3], or initial fiber waviness deduced from kink band geometry[4]. These models are generally semi-empirical and require testing of actual composites in order to determine key parameters required by the predictive analytical model.

More recently, Daniel[5] developed a model relating the in-plane tangent composite shear modulus, G_{12} , to composite critical stress. The model accounted for filament misalignment, and was applied successfully by Cho, *et al.*[6] to composites having known large misalignment. For this case, G_{12} was shown to decrease with increasing compressive stress, which is the correct trend based on measured strength. However, for the case of perfect alignment, their model simplifies to that of Dow and Rosen, as their original equation for the lowest energy buckling state is an idealized 2D expression for G_{12} at zero shear strain.

Dharan *et al*.[7] recently proposed a low-modulus interphase layer between the fiber and the matrix as an alternative explanation for lower measured strength values. Using an energy-minimization approach, the critical stress was derived assuming a thin, low modulus interphase. The final equation for critical stress is an idealized 2D expression for G_{12}, assuming an interphase. In this respect, it is equivalent to Rosen and Dow's development. Yet, empirical data show that the first order 2D approximation for G_{12} is already an under prediction, even when no interphase is assumed[8]. The proposed low modulus interphase, which correctly lowers the predicted value of compressive strength, incorrectly further lowers G_{12}. The problem to be solved is both the under prediction of initial G_{12} and the over prediction of compressive strength.

The current study addresses this apparent contradiction by extending the method of Daniel and co-workers. Starting from basic composite constituent properties and geometry, an analytical model is presented that calculates G_{12} as a function of increasing compressive stress. It is shown that when the magnitude of G_{12} equals that of the compressive stress, lateral instability occurs, and the compressive strength is reached.

Unit cell static analysis

The proposed model approaches the problem of longitudinal compressive strength of a unidirectional composite from a simple static equilibrium analysis. With Rosen's assumptions for the shear mode, one has a composite with a compressive modulus (E_1) that is high compared to the in-plane shear modulus

(G_{12}). Rosen further assumed that in-plane shear strain (β) did not vary in the direction transverse to the loading (x_2) and that the buckled wavelength was large. This enforces a pure shear deformation. Referring to Figure 3.1, the static equilibrium of an associated 2D unit cell of homogeneous properties is shown for the condition at which instability occurs.

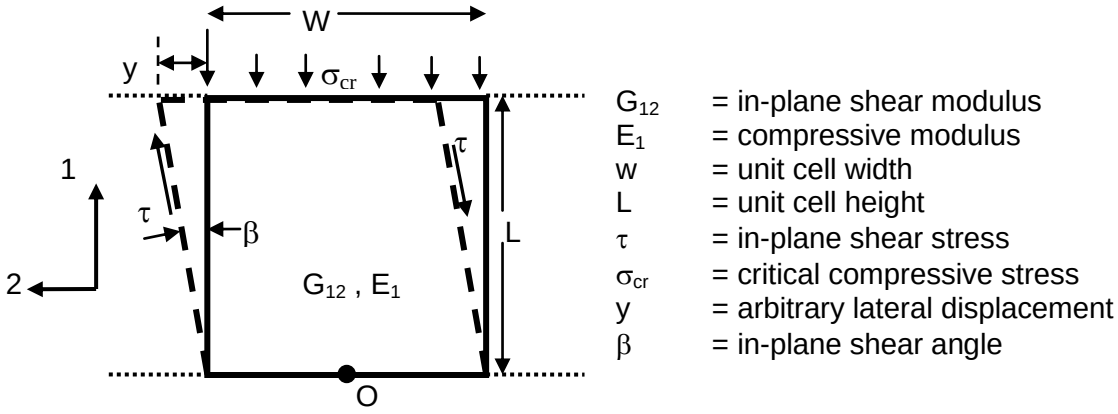

Figure 3.1: Shear instability for a general orthotropic material

Summing moments around Point O:

$$\sigma_{cr} W\, y = L\, \tau\, W \tag{1}$$

Noting that shear stress $\tau = \beta\, G$ and, for small angles $y / L = \beta$:

$$\sigma_{cr} = G_{12} \tag{2}$$

The unit cell approach can easily be applied to an idealized 2D bi-material composite composed of a fiber and matrix. A static summation of moments can be shown to result in Equation (3):

$$\sigma_{cr} = \frac{G_m}{1-v_f} \tag{3}$$

This is Rosen and Dow's original result, using their assumptions of very large fiber shear stiffness and very large fiber buckled wavelength. It is also a 2D idealization of Equation (2). Resistance to shear instability is supplied by the matrix; the fiber serves only as a matrix stress multiplier, and fiber bending stiffness is completely neglected.

The unit cell approach is easily applied to multiple layers of matrix materials each having different modulus. Multiple matrix layers can be represented as a homogeneous material having an equivalent shear modulus. The equivalent modulus is calculated by the rule of mixtures. For two matrix materials of thickness t_i and t_m, with shear modulus G_i and G_m:

$$\sigma_{cr} = \frac{G_{eq}}{1 - v_f}, \qquad where\ G_{eq} = \frac{t_i + t_m}{\frac{t_i}{G_i} + \frac{t_m}{G_m}} \tag{4}$$

Equation (4) can be shown to be equivalent to that obtained by Dharan, who used an energy minimization approach similar to Rosen's original development to analyze interphase effects. The added utility of the unit cell analysis is that it *underscores the direct relationship between G_{12} and critical compressive stress.* Accordingly, the ensuing model development focuses on determining G_{12}, and how composite constituents and the compressive loading event interact to continuously modify G_{12} until the point of lateral instability is reached.

Combined Stress Model

Equation (2) is the general governing equation for shear mode instability. Of great importance, as Daniel noted, the composite shear modulus, G_{12} is *not a constant* due to matrix nonlinearity. The shear modulus of the matrix, G_m, is a function of the matrix stress state. Accordingly, the combined stress model calculates matrix stress and *tangent* modulus as a function of applied composite compressive stress σ_1. Figure 3.2 provides a schematic overview of this process.

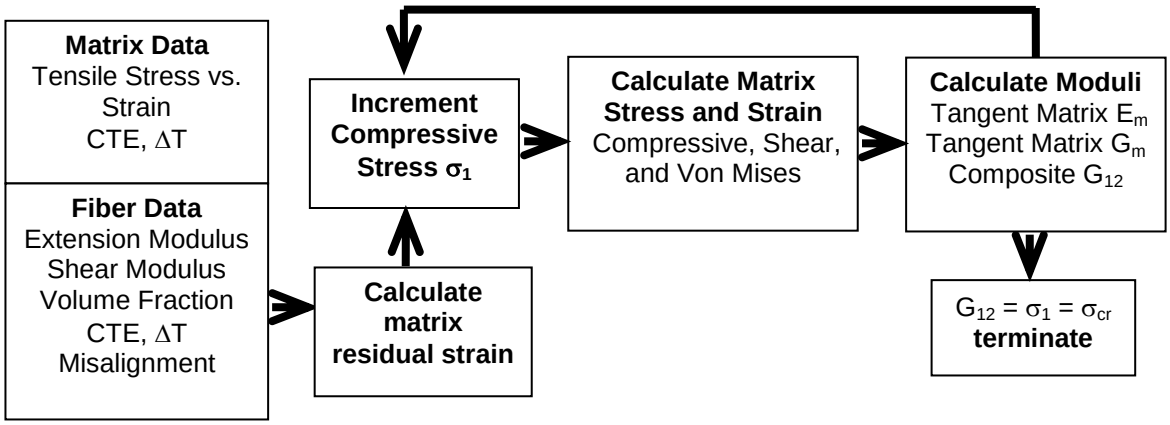

Figure 3.2: Combined Stress Model Flowchart

The heart of the flowchart in Figure 3.2 is the calculation of matrix stress and the ensuing calculation of composite G_{12} as a function of applied composite compressive stress σ_1. The ensuing development focuses on establishing the stress state of the matrix, and then estimating the tangent modulus of the matrix. From the tangent matrix modulus and other composite constituent properties, the expression for composite G_{12} will be defined.

Matrix Stress State as function of applied compressive stress σ_1

For a unidirectional laminate under an imposed compressive stress, the matrix stress state can be approximated by plane stress, as shown in Figure 3.3. The stress component subscript "m" refers to the stress in the matrix as opposed to the applied stresses on the composite.

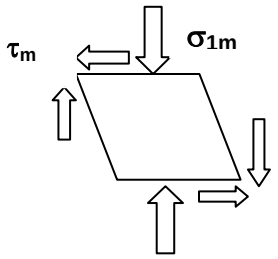

σ_{1m} = matrix compressive stress in fiber direction. This is an **imposed strain** due to fiber compression.

τ_m **=** matrix shear stress. This is an **imposed stress** due to fiber misalignment and imposed compressive stress.

Figure 3.3: Matrix stress state for imposed compressive stress

Matrix shear stress τ_m

In Rosen's original development, fibers were considered perfectly aligned. When alignment imperfection is added, shear stress is induced as a first order effect. As shown by Daniel, *et al.* (2006), misalignment φ with respect to the loading direction induces shear stress τ_{12} as a function of composite compressive stress σ_1 and in-plane shear stiffness G_{12}. For small angles:

$$\tau_{12} = -\sigma_1(\varphi + \Delta\varphi) \tag{5}$$

where Δφ is the additional fiber rotation cause by the shear stress, which is calculated from Equation (6):

$$\Delta\varphi = \frac{\tau_{12}}{G_{12}} \tag{6}$$

Using the step – stress approach of the Combined Stress Model, Equations (5) and (6) are employed to calculate τ_{12} and $\Delta\varphi$ as functions of applied compressive stress, σ_1.

Equation (6) requires G_{12}, which is nonlinear due to matrix nonlinearity. To relate G_{12} to matrix shear modulus, G_m, the relationship between the matrix and composite stress state is needed. As employed in a similar problem by Cho, *et al.* (2007), the matrix shear stress τ_m relates to composite shear stress τ_{12} as follows:

$$\tau_m = k_\tau \tau_{12} \quad \text{where } k_\tau = \frac{1 - V_f\left(1 - \frac{G_m}{G_f}\right)}{1 - \left(\frac{4V_f}{\pi}\right)^{0.5}\left(1 - \frac{G_m}{G_f}\right)} \tag{7}$$

With matrix τ_m known, the corresponding tangent shear modulus, G_m, can be found from testing of the neat resin. Given G_m, composite G_{12} can be approximated using the well-known Halpin-Tsai equation. Assuming a round filament cross section:

$$G_{12} = G_m \frac{1 + \eta V_f}{1 - \eta V_f} \text{ where } \eta = \frac{\frac{G_f}{G_m} - 1}{\frac{G_f}{G_m} + 1} \tag{8}$$

Equations (7) and (8) thus limit necessary inputs to fiber and resin constituent properties.

Matrix compressive stress σ_{1m}

Matrix compressive stress in the fiber direction results from residual thermal strain and from mechanical strain due to compressive loading. These two strains will be separately considered, then combined and transformed into the associated stress.

Thermal residual strain

Matrix residual strain is a complex phenomenon, depending strongly on manufacturing processes.[9] [10] The primary driver for thermal residual strain is the mismatch between fiber and matrix coefficients of thermal expansion (CTE), with the fiber generally having a lower CTE than the matrix. The stress-free state is generally assumed at an elevated cure temperature. At room temperature, the matrix develops a longitudinal tensile stress and the fiber a compressive stress, which are dependent on complex processes that occur during cooling. This study addresses the first order analysis by accounting for thermal effects using the simple linear result given below, for which the longitudinal matrix thermal residual strain ϵ_{1mt} is approximated as[11]:

$$\epsilon_{1mt} = (\mathrm{CTE_m} - \mathrm{CTE_c})\Delta T \tag{9}$$

$$\mathrm{CTE_c} = \frac{\mathrm{CTE_f}\,\mathrm{E_f}\,v_f + \mathrm{CTE_m}\,\mathrm{E_m} v_f}{\mathrm{E_f}\,v_f + \mathrm{E_m} v_m}$$

where subscripts c, m, and f denote the CTE of the composite, matrix, and fiber, respectively.

Compressive strain

The longitudinal compressive stress results in a matrix compressive strain ϵ_{1mc}. This is approximated by Equation (10):

$$\epsilon_{1mc} = \frac{\sigma_1}{v_f E_f + v_m E_m} \tag{10}$$

The term $v_f E_f$ is typically large compared to $v_m E_m$ since $E_f >> E_m$. Thus, even for the case of a tangent matrix modulus E_m approaching zero, the normal strain in the matrix, ϵ_{1mc}, is bounded. The compressive stress imposes a bounded compressive strain.

Conversely, composite shear stress τ_{12} is imposed, per Equation (5), which results in an imposed matrix shear stress, per Equation (7). For the case of G_m approaching zero, G_{12} also approaches zero. Additional fiber rotation becomes unbounded, per Equation (6), resulting in an unbounded imposed shear stress. One interpretation of this is shear instability.

Superposition of thermal and compressive effects

The compressive strain adds to the initial thermal residual strain. Integration of modulus over strain provides the matrix stress:

$$\sigma_{1m} = \int_{\epsilon_{1mt}}^{\epsilon_{1mt}+\epsilon_{1mc}} E_m(\sigma_{1m}, \tau_m) d\epsilon \tag{11}$$

where E_m is tangent matrix modulus for the specific matrix stress state.

Matrix tangent modulus given $\boldsymbol{\tau_m}$ and $\boldsymbol{\sigma_{1m}}$

For small strains, it will be assumed that matrix nonlinearity for a combined stress state can be quantified by using the von Mises stress in a uniaxial test. With known τ_m and σ_{1m}, the von Mises matrix stress is given by:

$$\sigma_{vmm} = \sqrt{\sigma_{1m}^2 + 3\tau_m^2} \tag{12}$$

From test data, the matrix uniaxial stress, $\boldsymbol{\sigma}$, vs. uniaxial strain, $\boldsymbol{\epsilon}$, is known:

$$\sigma = f(\epsilon) \rightarrow \mathbf{E_m} = \mathbf{f}'(\epsilon) \tag{13}$$

The inverse of Equation (13) calculates stress as a function of strain:

$$\epsilon = g(\sigma) \tag{14}$$

Equation (12) gives the matrix von Mises stress for the combined loading event of Figure (3); Equation (14) gives the equivalent uniaxial strain at constant deviatoric stress; Equation (13) calculates the tangent modulus at this uniaxial strain.

Given the matrix uniaxial modulus, the shear modulus at small deformations is:

$$G_m = \frac{E_m}{2(1+\upsilon)}, \quad \text{where } \upsilon = \text{Poisson's ratio} \tag{15}$$

Equations (5) through (15) can be solved using a step load numerical procedure, as schematized in Figure 2. Evolution of G_{12} with respect to σ_1 is the final result, with shear instability at $\sigma_1 = G_{12}$. Complete details are provided in Appendix A. An example showing the employ of each equation in calculation of the salient variables is also given.

Validation test case

Matrix stress-strain character and fiber alignment data are necessary inputs for the proposed model. Studies in the literature generally do not include such data from actual composites for which compressive strength was measured. Therefore, to test model performance, a glass/resin unidirectional composite was constructed using standard methodologies. Specific attention was given to characterization of the matrix modulus and the fiber alignment.

Basic constituents consisted of:

- Vinyl ester resin Atlac 590. Initial tensile modulus E_m = 3.5 GPa. Ultimate σ_t = 90 MPa, CTE = 3×10^{-5}
- Owens Corning Advantex Glass fiber. E_f = 78 GPa, G_f = 30.5 GPa, CTE = 5×10^{-6}
- V_f = 0.50

Construction and Characterization

Pre-preg construction followed the standard procedure of winding the single end roving filament around a 300 x 300 mm steel frame, then applying the uncured resin. After partial cure under laboratory light and ambient temperature, the pre-preg was cut from the frame, then cut to 250 x 75 mm strips. Each

individual laminate layer was 0.22 mm thick. Twelve layers were combined in a mold of 250 x 75 mm dimensions. The mold was placed in a press, and cured at 180 C, under 2 bar pressure, for 60 minutes. Five unidirectional laminate samples of 140 x 12.5 x 2.64 mm were then cut from this plaque, as necessary for ASTM D6641 protocol.

Additional test samples were constructed from the same plaque, and then machined for microscopic analyses. A representative cross section is shown in Figure 3.4.

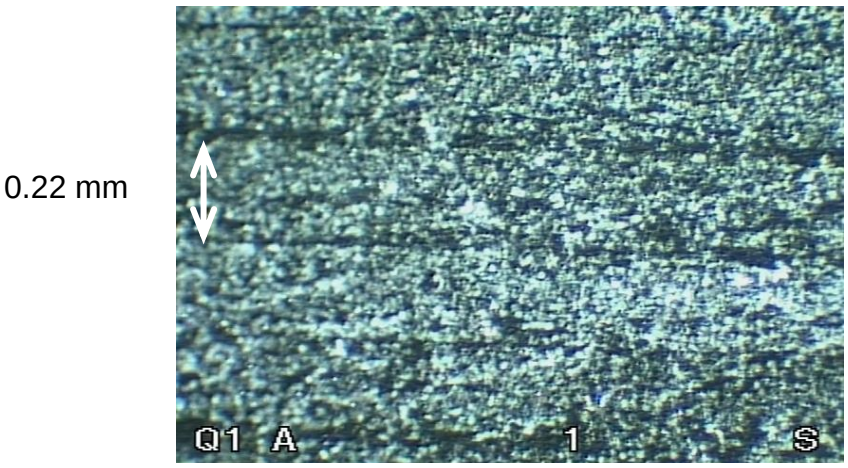

Figure 3.4: Validation case cross section

While individual pre-preg layers are discernable, the interlaminar distance is only around 20 μm thick. The section approximates a transversally isotropic material, with $G_{13} = G_{12}$. However, the presence of any interlaminar thickness serves to reduce G_{13}; thus, calculated values of G_{12}, and associated compressive strength calculations based on G_{12} will likely be upper bound estimates.

FEA of 3 point beam test to determine matrix extensional modulus characteristics

Samples of neat resin Atlac 590 were tested in ASTM D790. Specimen dimensions are 30 mm length, 10 mm width, and 1.35 mm thick. Measured center deflection at sample failure was above 5 mm. This was not small compared to the beam length of 30 mm.

Accordingly, Abaqus 6.10 was used with the **Nlgeom** flag set to "1", thus updating the stiffness matrix to account for geometry changes. Plane stress quadratic elements without reduced integration (CPS8) were used. The material law was Abaqus' standard hyperelastic formulation using Marlow strain energy potential. Model geometry was a 2D plane stress representation.

With Marlow strain energy potential for hyperelastic materials, the option permitting uniaxial test data was used. By iteration, the uniaxial stress vs. strain relation was found such that the FEA prediction matched the measured beam center deflection vs. load. The final modulus curve is shown in Figure 3.5a, while the measured vs. predicted center beam deflection is shown in Figure 3.5b. The initial modulus at zero strain was 3.5 GPa, which matched the publicly available data sheet. The FEA prediction for the maximum tensile stress was 90.5 MPa at 4% strain. This compared favorably to datasheet information of 90 MPa for tensile strength at 4% strain.

With this data, Equations (13) and (14) can be established via a simple polynomial fit. The only additional unknown necessary for Equation (5) is initial

filament misalignment. All other necessary information is contained in the composite consituents.

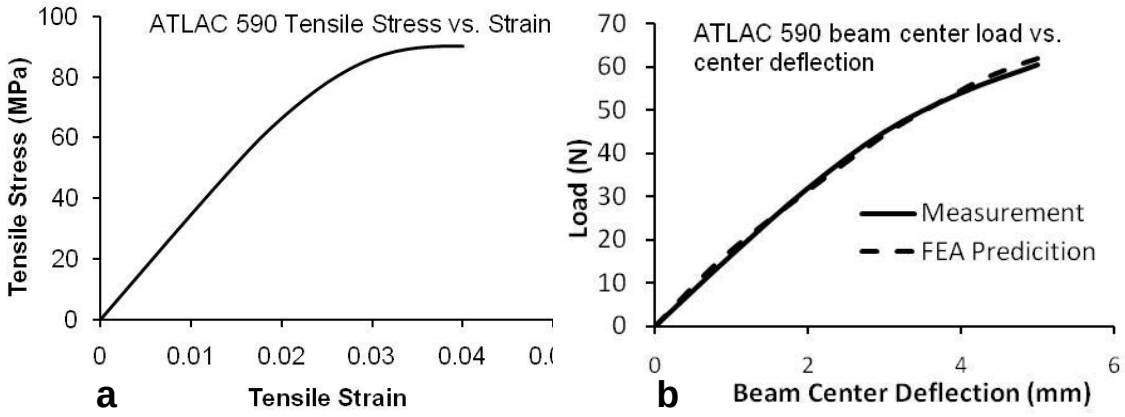

Figure 3.5: Atlac 590 modulus and 3-point beam load vs. deflection

Misalignment characterization

Filament misalignment is of 1st order importance, as shown by Daniel (2006), Budiansky (1983), Frost[12], and others. To measure this, an individual pre-preg layer was fully cured and microscopically analyzed for filament misalignment. This is a conservative condition for misalignment, as the molding process results in additional slight filament disturbances and therefore misalignment. Figure 3.6 shows a microscopic image of filament alignment. Grid spacing is 100 μm. The entire image represents a section of approximately 0.5 x 0.5 mm.

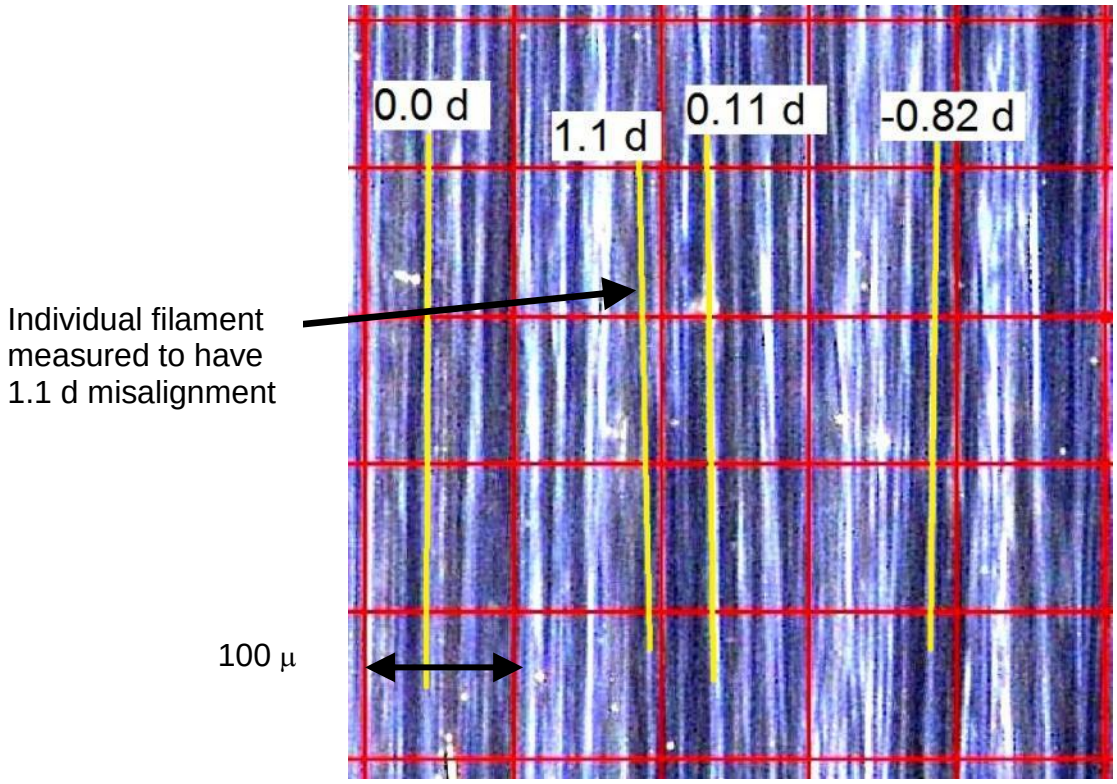

Figure 3.6: Validation test case pre-preg misalignment

To measure misalignment, the sample orientation was first aligned with the microscopic grid. Imaging software permitted angle measurement of individual filaments relative to the grid orientation. A positive orientation was defined as counterclockwise from vertical. Four such measurements are shown in Figure 6. Twelve such segments of 0.5 x 0.5 mm were analyzed, with a total of 492 filament misalignments individually measured.

Only filaments that were clearly visible for a vertical distance of at least 300 μm were considered. This was not arbitrary for two reasons. First, theoretically, a glass filament of 15 μm diameter and 300 μm length has a length to width ratio of 20:1. Filament bending stiffness becomes negligible, and the

conditions for Figure 3.1 and Equation (2) are satisfied. This necessary condition becomes compromised at shorter filament lengths. Second, comparatively few filaments were clearly identifiable over a length greater than 500 μm; thus, limiting measurements to filaments that were visible over greater lengths would have greatly reduced the sample size.

Alignment data were treated in the following steps:

1. Individual filament misalignment angles were measured.
2. Misalignment average was calculated as **-0.096** degrees
3. Average misalignment was subtracted from each measure, giving a corrected average=0.
4. Absolute values of corrected filament misalignments from (3) were taken.
5. Histogram of step 4 was calculated.
6. Polynomial fit of step 5 was calculated, using cumulative V_f as function of misalignment.

Step 3 enforced zero macroscopic compression-shear coupling, while Step (4) completely allowed microscopic induced matrix shear, per Equation (5). The rationale for this was that few crossed filaments of positive and negative misalignment were observed; the general case was that filaments with like misalignment signs were grouped together. Absolute values of measured filament misalignment from Step 4 are shown in Figure 3.7.

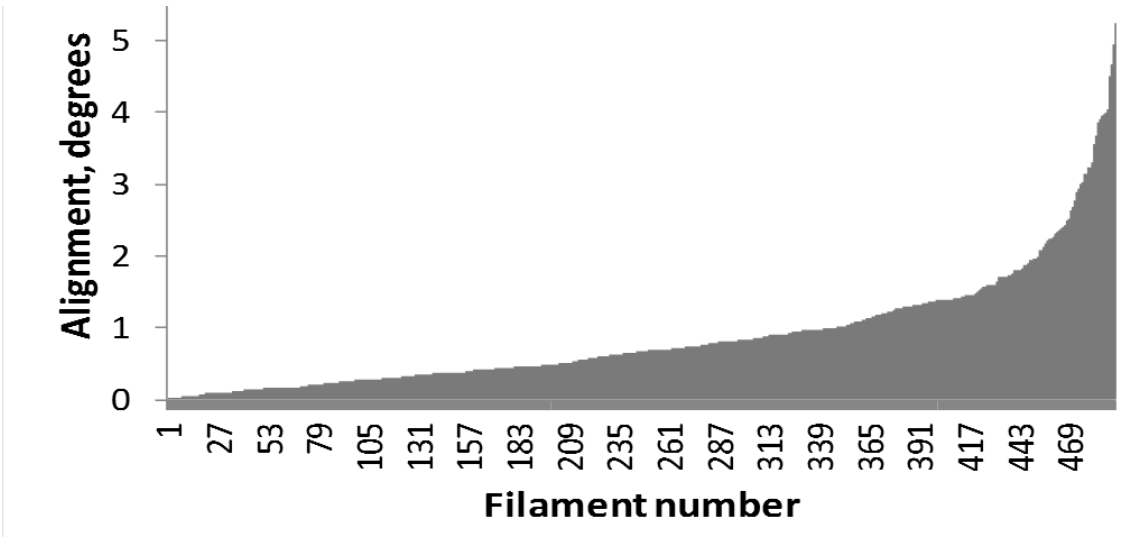

Figure 3.7: Pre-preg individual filament misalignments

This distribution can be expressed as cumulative volume fraction vs. measured misalignment. A 4th order polynomial provides a mathematical representation, as shown in Figure 3.8.

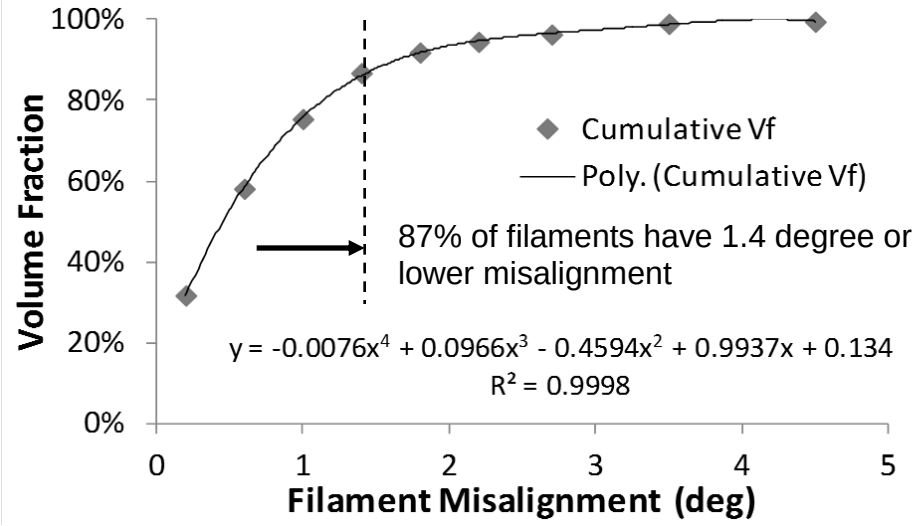

Figure 3.8: Cumulative volume fraction vs. filament misalignment

As indicated, Figure 3.8 shows that 87% of filaments have a misalignment of 1.4 deg or less, while 13% have a misalignment of 1.4 deg. or greater.

With alignment known, the next step was calculating compressive strength as a function of *homogeneous* misalignment. Given test case constituents and matrix characteristics, the Combined Stress Model calculated strength as a function of misalignment, as presented in Figure 3.9.

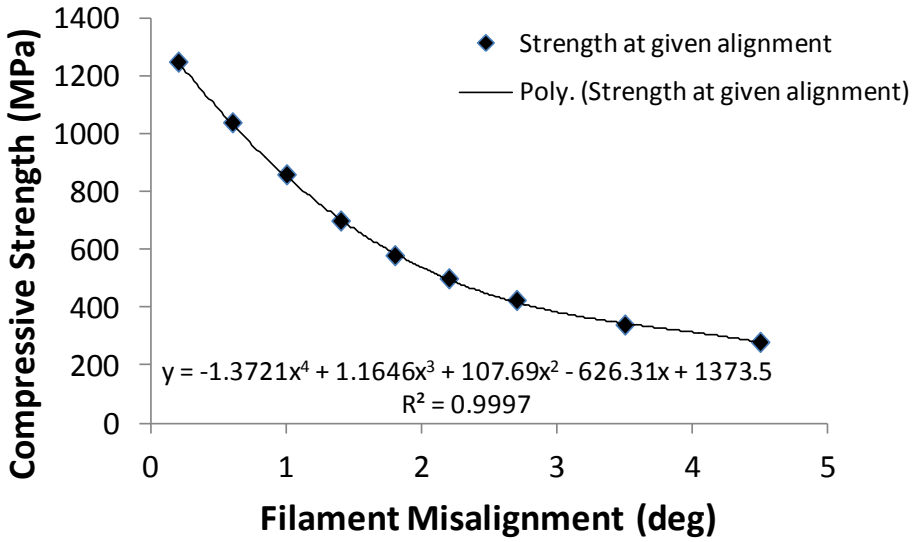

Figure 3.9: Compressive strength vs. homogeneous misalignment

Composite tensile strength has been modeled as multiple elements in tension, in which filament imperfections result in some filaments breaking at a lower stress than others.[13] Compressive strength can be treated similarly, where the imperfection is due to misalignment. For small misalignment angles, stiffness remains constant; thus, the composite can be modeled as many parallel columns, each having the same modulus, yet different strength. A simple example using 4 parallel columns is shown in Figure 3.10.

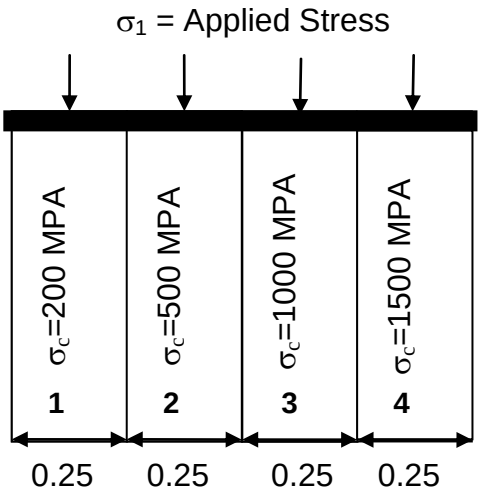

Figure 3.10: A compressed composite column consisting of 4 parallel columns of identical modulus and section area, but different compressive strengths

Strength calculation of the composite column is straightforward, yet requires clarity in the definition of cross section areas. The *applied stress* σ_1 is calculated relative to the initial total area of the composite column. As the column is loaded, individual columns progressively fail, as their compressive strength, σ_c, is reached. This causes the intact section area to decrease. The actual stress supported by the intact section is assumed to correspond to a uniform redistribution of the load. Knowing the strength distribution within the composite column, Table 3.1 shows how to calculate the strength of the composite column. As shown in Table 3.1, the stress σ_1 is highest when Columns 1 and 2 have failed and Column 3 is at the point of failure, with σ_1 = 500 MPa.

	Column 1	Column 2	Column 3	Column 4
Compressive Stress σ_c at failure (MPa)	200	500	1000	1500
Intact Section	1.0	0.75	0.50	0.25
Applied stress σ_1 on composite column (MPa)	200 x1.0 =**200**	500x0.75 =**375**	1000x0.50 =**500**	1500x0.25 =**375**

Table 3.1: Compressive strength calculation for composite column shown in Figure 3.10.

The approach presented in Figure 3.10 and Table 3.1 can be used for the test case continuum by multiplication of the curve fits from Figures 3.8 and 3.9. The result is the applied stress at which the most poorly aligned sections of the intact section fail. Compressive strength of the test case is the maximum applied stress obtained, as shown in Figure 3.11.

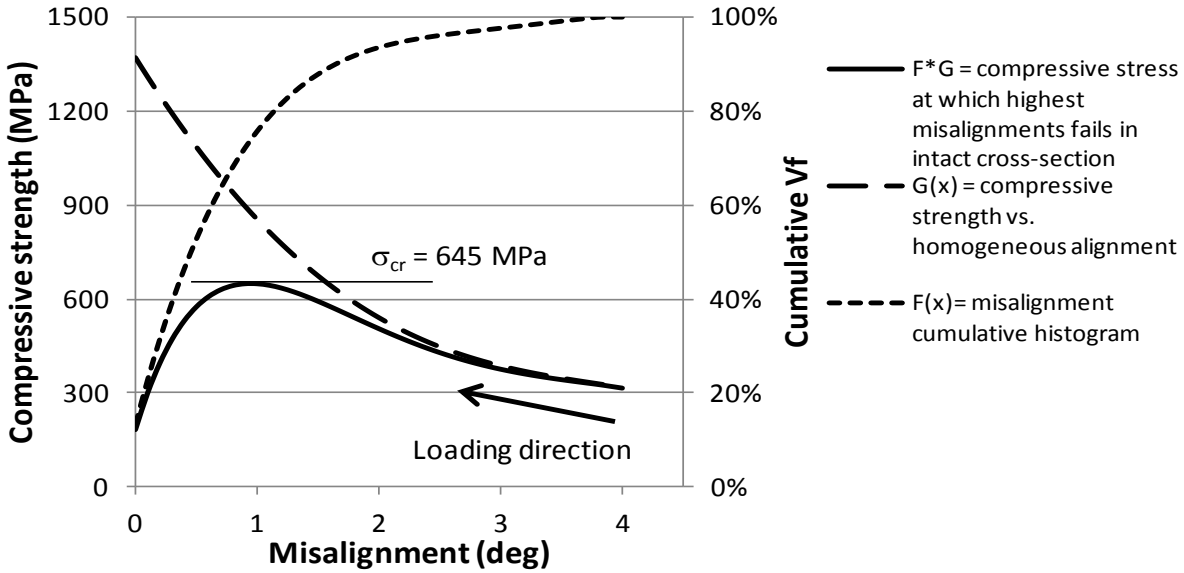

Figure 3.11: Misalignment histogram (F(x)), compressive strength at homogeneous misalignment (G(x)), and test case applied stress (F x G) at which highest misalignments in intact section fail

Figure 3.11 is best understood by considering the compressive loading event. As the test case composite is loaded in compression (solid line, from right to left) imposed matrix shear stress increases most rapidly adjacent to fibers having a large misalignment. Local failure occurs, and the remaining intact section carries higher stress. This is perfectly analogous to the simple case of Figure 3.10, except that the compressive strength continuum is now taken into account.

Regions of poorest alignment locally fail as additional load is applied. For the test case, this continues until applied σ_1 = -645 MPa. With 25% of the section having already failed, the actual stress on the intact section is -860 MPa. This stress is incrementally higher than the critical stress at the most poorly aligned areas of the remaining section. Thus, at -645 MPa, the remaining 75% of the cross section abruptly fails.

Anecdotally, this concept is supported by audible cracking or popping sounds that preceded compression sample failure. It is reasonable to suppose that these sounds were local matrix / fiber failures in areas of higher misalignment. The literature also indirectly supports this, as glass and carbon fiber composites have compressive moduli that decrease prior to failure. [14] Because the fibers have linear moduli and carry the compressive stress, nonlinearity in composite modulus could be explained by a progressive loss of cross-section integrity.

Compressive Strength Measurement

Five validation test case samples were tested in ASTM D6641. The results gave a compressive strength of **565 MPa ± 49 MPa.** The failure was in the 1-2 and the 1-3 directions for these samples, with some interlaminar failure noted. The model prediction of 645 MPa is 14% higher, which could be considered quite good. The Combined Stress model could be expected to give higher strength estimates, as it assumes no interlaminar effects. Also, this value of compressive stress was consistent with literature values, suggesting that prototyping methodology and quality were consistent with historical practice. From the literature, compressive strength values for similar glass-resin composites range from 590 MPa to 630 MPa.

G_{12} *vs.* σ_1

Test case results are more meaningful when seen in the context of the Combined Stress Model step stress operation of Figure 3.2 This is most easily represented in a graphical sense by plotting the matrix stress and G_{12} as functions of applied compressive stress. One complicating factor is that the test case consisted of a continuum of fiber misalignments.

However, there exists a homogeneous misalignment which gives the same compressive strength as the continuum of misalignments. For the test case, this "*equivalent misalignment*" is about 1.5 degrees. Figure 3.12 shows the matrix stress state and G_{12} as functions of applied compressive stress at this equivalent misalignment.

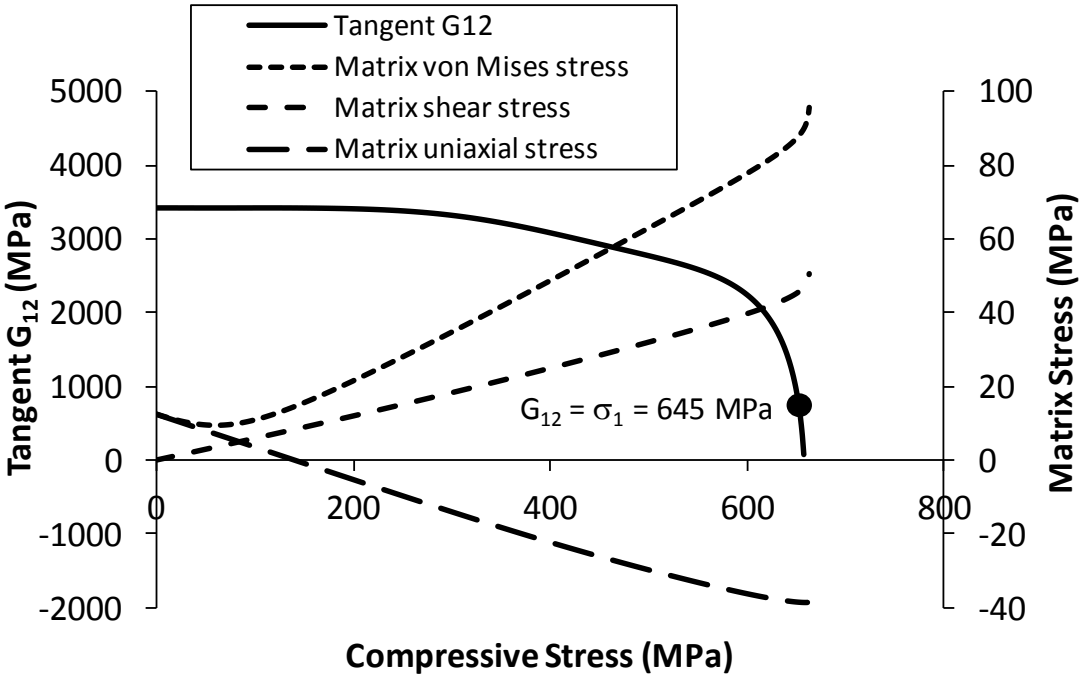

Figure 3.12: G_{12}, τ_m, σ_{1m}, and σ_{vmm} vs σ_1, for test case equivalent misalignment = 1.5 deg.

Figure 3.12 shows:

- Matrix shear stress, τ_m , increases slightly faster than linearly, becoming unbounded just after the point of instability. This is due to fiber rotation and matrix nonlinearly.
- Matrix longitudinal stress , σ_{1m} , begins slightly positive, due to thermal prestress. It decreases slower than linearly as a compressive strain is imposed. Matrix modulus decreases with deformation; under imposed strain, stress varies with modulus.

- Matrix von Mises stress, σ_{vmm} , becomes dominated by the shear stress at higher deformation. It becomes unbounded just after the point of instability.
- A high initial composite G_{12} of 3400 MPa is calculated, yet a compressive strength below 700 MPa. The combination of matrix nonlinearity and fiber misalignment push the matrix von Mises stress to 88 MPa at a compressive stress of 645 MPa. The matrix tangent modulus rapidly decreases at this point, which results in an abrupt drop in G_{12}. Instability results.

These results and trends are the result of (a) the operation of Equations (5) through (15), (b) composite constituent properties, and (c) test case misalignment measurement.

Parameter sensitivity

Using stress vs. strain behavior measured for Atlac 590, thermal prestress, filament modulus, and filament misalignment effects were mapped. For these comparisons, the misalignment can be considered equal to the equivalent misalignment, as previously defined.

The impact of matrix residual strain was modeled for two levels of fiber modulus, as a function of fiber misalignment. Volume fraction was held constant at $V_f = 0.50$. An upper bound for the value of thermal residual strain was calculated using a reasonable limit case. Given a $\Delta T = 155$ C and $CTE_m = 3 \times 10^{-5}$, the maximum matrix tensile prestrain is obtained by assuming an infinitely stiff fiber with CTE = 0. This gives a matrix prestrain slightly less than 0.50%. This was compared to a residual strain of zero for glass fiber ($E_f = 80$ GPa) and carbon fiber ($E_f = 220$ GPa). Results are shown in Figure 3.13 as a function of equivalent misalignment

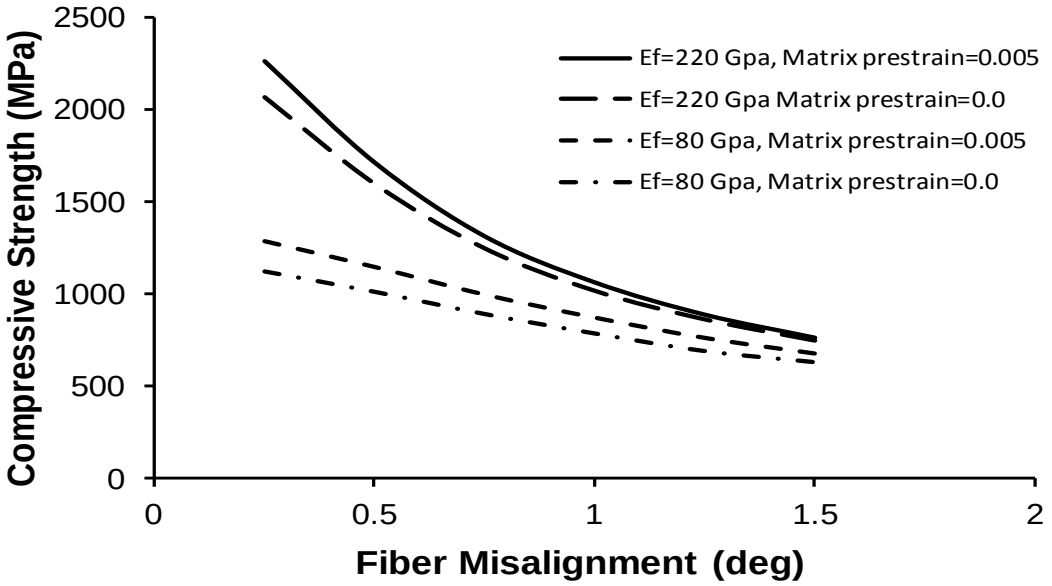

Figure 3.13: Effect of matrix prestrain; $V_f = 0.5$

Thermal prestrain provides a moderate beneficial effect, particularly for the case of highly aligned fibers. For $E_f = 220$ GPa at misalignment = 0.25 deg, the compressive strength increased by 200 MPa. Better alignment results in less induced shear stress; thus, the longitudinal matrix stress is a more significant

component of the von Mises stress. A tensile residual strain reduces matrix compressive stress for a given compressive load, thereby increasing the tangent shear modulus. As misalignment increases, shear stress becomes dominant and residual strain becomes less significant.

While not studied here, matrix characteristics could play a larger role in the sensitivity of residual strain on compressive strength. For example, a high modulus, low ultimate strain matrix would benefit even more from a residual tensile strain. This is especially when used in the context of highly aligned, high modulus fibers, where even small tensile residual strains would be favorable.

To map the effect of filament modulus, thermal prestrain was set equal to zero, as this varies widely depending on production methodology. For consistency, filament shear stiffness was held constant at 20 GPa, which is an approximate average of glass and carbon fiber shear stiffness. Compressive modulus was assumed equal to tensile modulus. Equivalent fiber misalignment was held constant at 1.0 degrees. With these values used as inputs, changes in compressive strength for various filament moduli were mapped as a function of volume fraction, as shown in Figure 3.14.

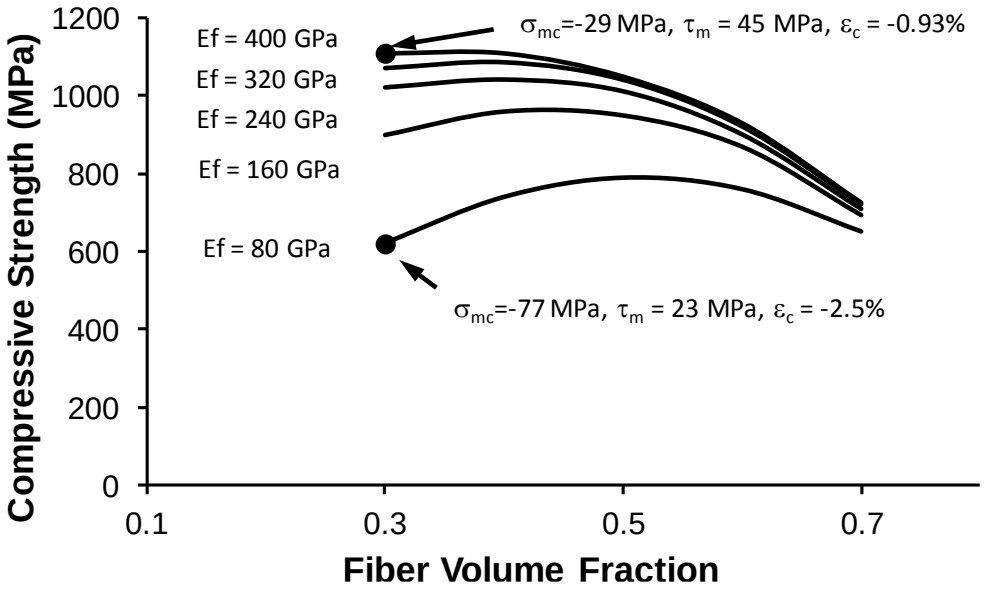

Figure 3.14: Effect of fiber modulus, with misalignment = 1 degree

A fiber modulus of 80 GPa corresponds to Advantex glass filament, while 400 GPa is that of boron fiber. The model predicted large increases in compressive strength at low V_f with increasing E_f, with progressively less increase as V_f increased. Stiffer fibers result in lower matrix compressive stress. At V_f = 0.3, a glass composite would have a matrix compressive stress of 77 MPa and a compressive strength of 610 MPa. A boron composite would have a matrix compressive stress of 29 MPa and a compressive strength of 1160 MPa.

As volume fraction increases, the effect of induced shear becomes more pronounced, due to the stress concentration factor k_τ of Equation (7). Conversely, compressive stress becomes proportionately less pronounced with increasing volume fraction due to the increased compressive stiffness of the composite. At iso fiber alignment, the advantage of a very stiff reinforcement becomes less at high volume fraction.

Fiber stiffness is not directly present in the combined stress model. Rather, the effect of fiber stiffness on the matrix stress state, and thus tangent modulus, drives the model prediction. For this reason, a stiffer fiber results in higher composite compressive stiffness.

The effect of fiber misalignment at constant fiber modulus was also mapped as a function of volume fraction, as shown in Figure 3.15.

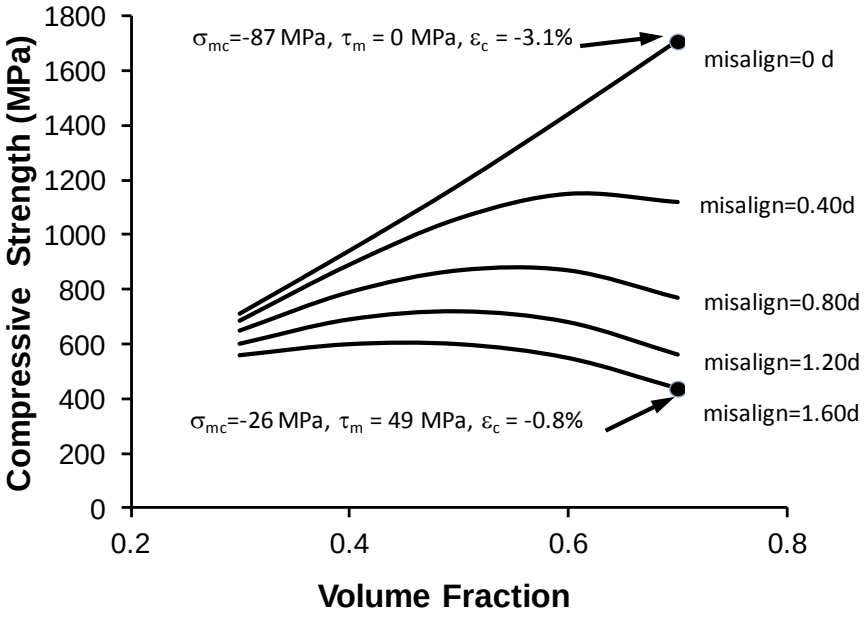

Figure 3.15: Effect of fiber alignment, with E_f = 80 GPa

At low V_f, fiber misalignment is predicted to reduce compressive strength less than at higher V_f. The reason for this is that k_T is lower for low V_f, and the matrix stress is dominated by compression. At higher V_f, matrix compressive stress is reduced because of the increase in composite compressive stiffness. Matrix stress is thus dominated by induced shear, which increases with increasing misalignment.

One important observation regarding Figure 3.15 is that increasing V_f gives diminishing returns for compressive strength. Except for the case of perfect alignment, there is an optimum V_f, and further increases result in little improvement, or even a decline in compressive strength. This is counter-intuitive, yet relates to the cumulative effect of Equations (5) through (15), as G_{12} is calculated as a function of σ_1. Matrix shear drives the problem at high volume fraction, even for relatively small fiber misalignments of 0.4 degree.

Comparison with literature values

Direct comparison with literature values is challenging since matrix stress vs. strain is generally not provided. Matrix data is usually limited to initial extensional or shear modulus. Furthermore, fiber alignment measurements similar to what was done for the test case in this study are not provided. To compare model results with literature values, the following actions were taken:

- The measured stress vs. strain character of vinyl ester resin Atlac 590 was used, and scaled according to the initial modulus. This resin has an initial modulus of 3500 MPa (shear modulus = 1250 MPa). Thus, for comparison to a composite having a matrix modulus of 4000 MPa, the stress was scaled up by 14% for each strain value.
- Equivalent misalignment for the Advantex glass fiber test case = 1.5 degrees. Stiffer filaments should have better alignment. The following comparisons assume carbon fiber and boron fiber are more highly aligned. Assumed misalignment values are given.

- For each case, the sensitivity of misalignment magnitude is shown by providing compressive strength estimates for more than one misalignment.
- Matrix residual strain is held constant at 0.35%. This is an average value for glass composites similar to the test case, for volume fractions of 0.3 to 0.65.

Figure 3.16 shows model predictions compared to historical values for E-glass composites over a range of V_f. Results are favorable in magnitude and trend. Both historical data and model predictions suggest an optimum V_f for highest compression strength. For polyester resin, this occurs around $V_f = 0.50$, while for epoxy resin the optimum is perhaps 0.65. This is reasonable, as epoxy resins will generally have a higher ultimate strength and higher tangent modulus when highly stressed. Precise data regarding resin modulus and misalignment could significantly improve model prediction, yet it performs reasonably even with the approximate input data.

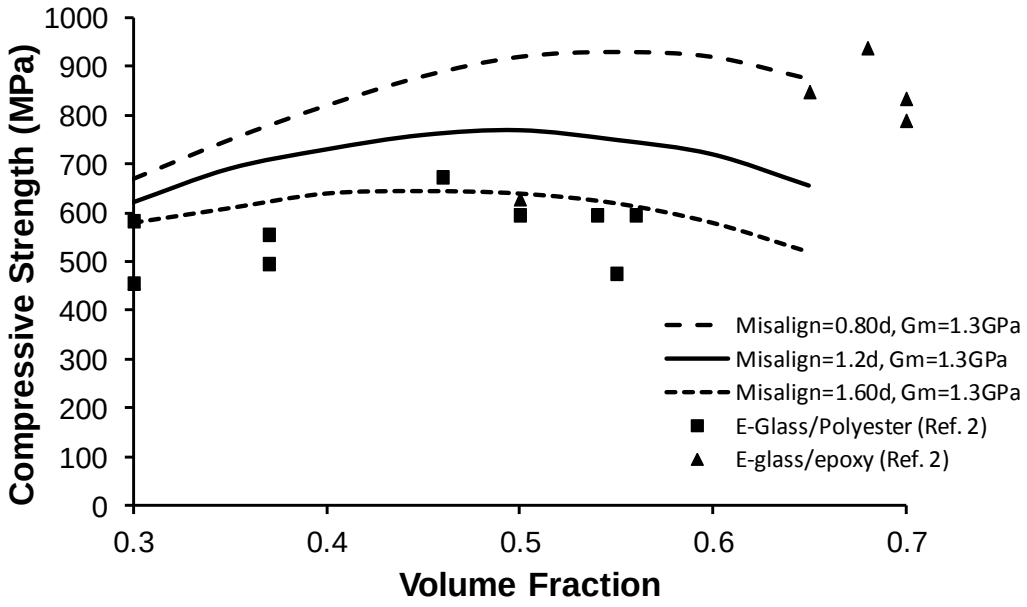

Figure 3.16: E-glass fiber / resin: model results and empirical data

Figure 3.17 shows predicted and literature results for carbon fiber composites. Compared to glass, carbon composites have over twice the compressive strength. This is predicted by the combined stress model, even though the prediction is based on the stress state and modulus of the matrix. As with glass composites, there is apparently an optimum V_f for compressive strength. Empirically, this value is around $V_f = 0.60$ for both T300/5208 and AS4/3501-6. With misalignment between 0.5 and 0.8 degrees, the model predicts this optimum V_f.

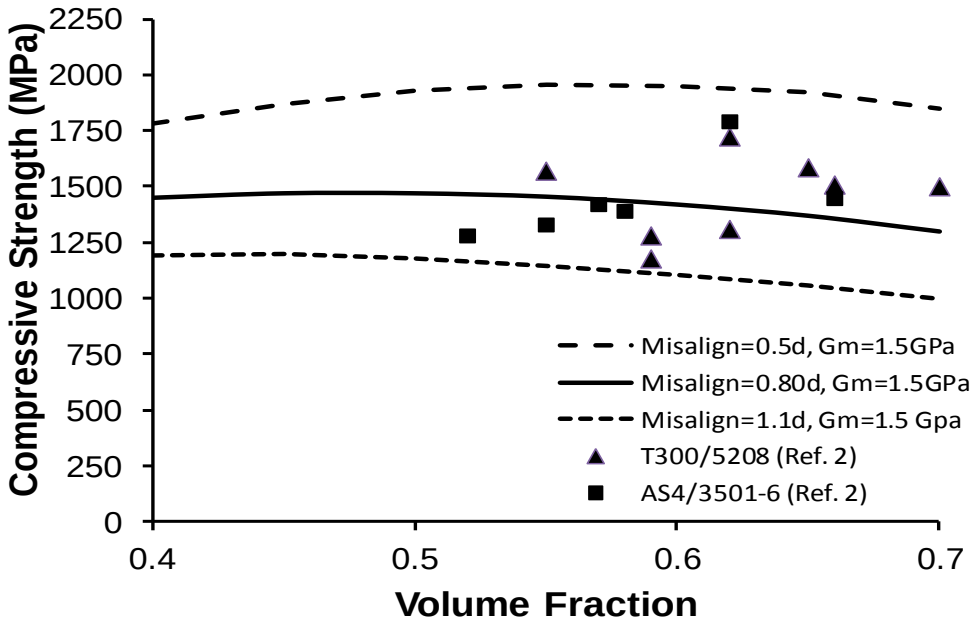

Figure 3.17: Carbon fiber / resin: model results and empirical data

Boron fiber composite predictions and literature values are shown in Figure 3.18 over a wide range of V_f for two resin moduli. Boron, which has a modulus of E_f = 400,000 MPa, obtained measured compressive strength values that were high even for moderate V_f levels. The combined stress model predicted both the trend and magnitude of compressive strength over the range of V_f for both modulus levels. Again, the model did not rely at all on fiber bending stiffness, but only matrix stress as a function of fiber modulus and alignment.

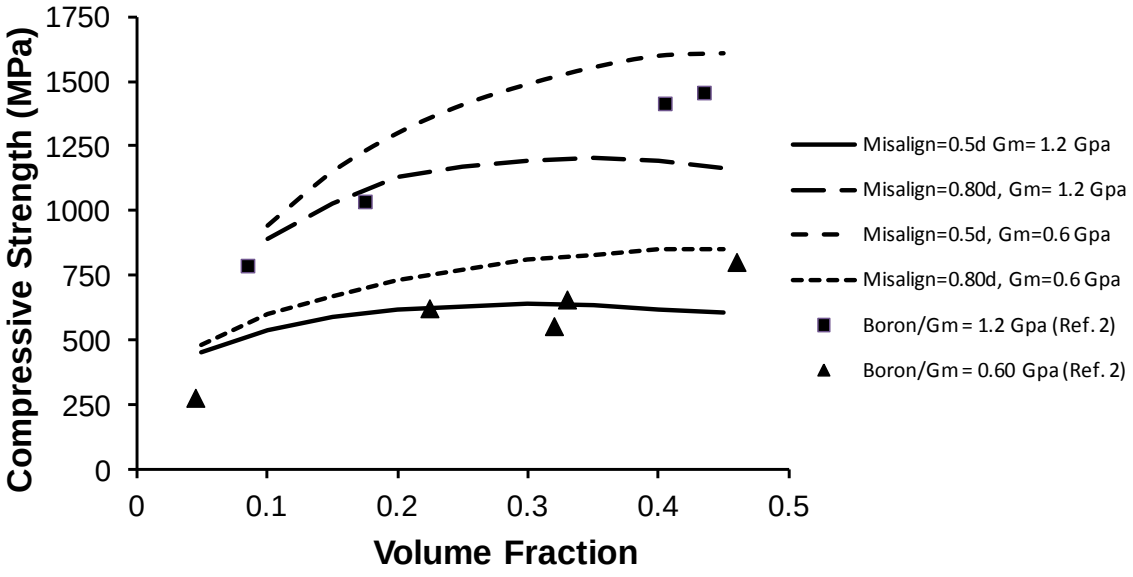

Figure 3.18: Boron fiber / resin: model results and empirical data

Finally, Figure 3.19 compares predictions and historical values for three specific composites having large differences in fiber modulus. Resin modulus and volume fraction are similar for each case, as noted. The analysis assumes that fiber alignment improves with increasing fiber stiffness, as also noted. Thermal prestrain was held constant at 0.35%. For each case, the combined

stress model slightly over predicted the compressive strength by 2 – 15%. The trend of increasing compressive strength with increasing fiber modulus is very well predicted.

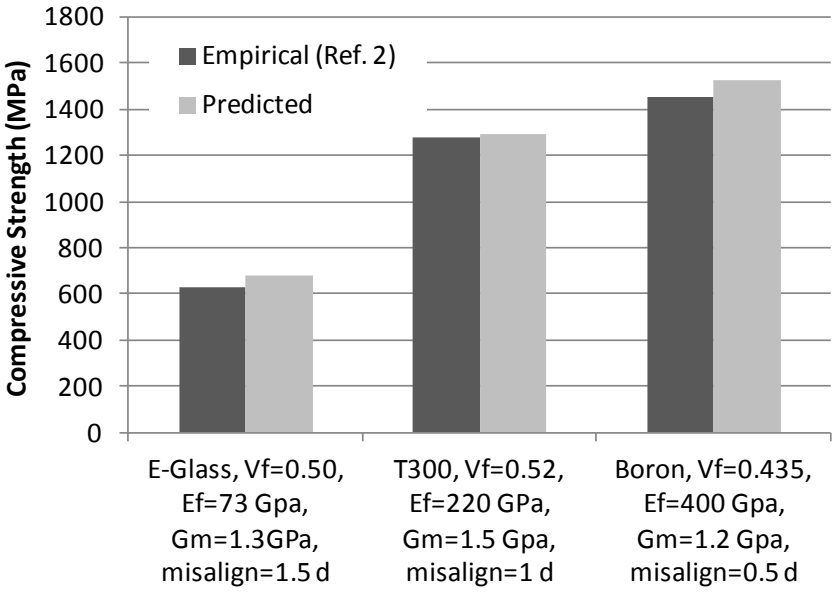

Figure 3.19: Model results and measurements for 3 levels of fiber stiffness.

Discussion

A new model should offer new compelling explanations for observed phenomena. In a limited fashion, the combined stress model offers an original rationale for the difference in compressive strength of boron, carbon, and glass fiber composites. The literature recognizes that boron composites offer the highest compressive strength, while glass is the lowest; yet explanations generally center on the compressive strength of the reinforcement itself, or of the size of the elementary filament and therefore the filament bending stiffness. This study suggests Rosen's original treatise is essentially correct for the shear mode;

i.e., neither filament bending nor compressive stiffness plays a direct role. Rather, a stiff reinforcement results in less matrix compressive stress and thus higher tangent matrix shear modulus for a given compressive stress. Higher tangent matrix modulus and higher matrix ultimate stress and elongation emerge as delineating factors. This is complementary to, not inconsistent with, Rosen's development.

According to the study here, the diameter of boron fiber (100 μm) compared to glass (10 μm) does not play a direct role in compressive strength. Indeed, at equal volume fraction the initial G_{12} stiffness of boron and glass fiber composites are comparable, whereas the compressive strength of the boron composite is 250% higher[15]. There are two potential reasons that give boron an advantage. First, the much higher boron compressive stiffness greatly reduces matrix compressive stress, as mentioned above. Second, the larger filament diameter and modulus greatly increase filament bending stiffness, which potentially improves alignment. *Alignment is a first order effect*, as this induces matrix shear strain, with even local misalignments of 0.5 degrees having a profound impact on compressive strength. Again, it is the stress state of the matrix which truly governs the compressive performance, yet reinforcement modulus and geometry play a vital role in determining matrix solicitation under compression.

Small misalignments also add another dimension to the problem*: the matrix stress state has a stress imposed component.* Thus, modeling the matrix

as an elastic-plastic material becomes problematic. With decreasing G_{12}, Equations (5) and (6) suggest fiber rotation $\Delta\varphi$ becomes large; accordingly, the current model results in rapidly increasing imposed shear stress as fibers rotate and matrix shear modulus decreases. Shear instability results.

Finally, models generally contain simplifying assumptions. As developed in this study, one of the assumptions of the combined stress model is that matrix nonlinearity can be characterized by the equivalent Von Mises stress. This study characterized the matrix with a bending solicitation, which contained tension, shear, and compression. This is different from pure compression, and inaccuracies could occur for some types of matrix materials under certain combined stress loadings. For example, for the case of perfect alignment the matrix stress is pure compression, yet some matrix materials have an ultimate compressive strength that is higher than the ultimate tensile strength. For these cases, the approach used in this paper would perhaps over estimate the modulus loss for a given compressive stress. The model performance is conditioned by the accuracy of the algorithm used to predict tangent modulus for a given stress state.

Conclusion

1. The stress vs. strain behavior of the resin is non-linear. When a composite is compressed, the resin is subject to compressive stress and shear strain. G_{12} is a function of matrix modulus; thus, G_{12} decreases as a function of compressive stress.

2. A model has been developed that calculates composite G_{12} as a function of compressive stress for a unidirectional composite having a given fiber misalignment. Thermal residual stress is included. Matrix stress is calculated as a function of compressive stress, along with the associated drop in tangent modulus.
3. A method of measuring and characterizing the fiber misalignment continuum was developed.
4. A method for calculating the compressive strength of a composite having a fiber misalignment continuum was developed. Model predictions agreed well with test data for a specific test case.
5. Model predictions agreed well with historical data from the literature, in both magnitude and trend. A range of fiber properties, matrix properties, and volume fractions were investigated.
6. Model predictions indicate a very high sensitivity of compressive strength to fiber alignment.
7. The model suggests that observed differences in compressive strength of composites having boron, carbon, or glass reinforcement come from the combined stress state of the resin. Fiber modulus intervenes as it affects matrix stress and therefore matrix tangent modulus.
8. The combined stress model preserves initial G_{12}, while suggesting that compressive strength is indeed driven by G_{12}, as it decreases with increasing compressive stress.

References

[1] Dow, N.F., Rosen, B.W. (1965). Evaluations of Filament-reinforced Composites for Aerospace Structural Applications*, NASA CR-207*.

[2] Lo, K.H., Chim, E.S-M., (1992). Compressive Strength of Unidirectional Composites. *Journal of Reinforced Plastics and Composites*, *11*, 838-96.

[3] Xu, Y.L. and Reifsnider, K.L. (1993). Micromechanical Modeling of Composite Compressive Strength. *Journal of Composite Materials*, *27*, 572-588.

[4] Budiansky, B. (1983). Micromechanics*, Comput Struct*, *16*, 3-12.

[5] Daniel, I.M., Ishai, O. (2006*). Engineering Mechanics of Composite Materials, 2nd Ed.***,** Oxford University Press, Inc., New York, pp. 107-109.

[6] Cho, J., Chen J.Y., Daniel, I.M. (2007). Mechanical enhancement of carbon fiber/epoxy composites by graphite nanoplatelet reinforcement. *Acta Materialia Inc*., Elsevier Ltd.

[7] Dharan, C.K.H., Lin, C.L. (2007). Longitudinal Compressive Strength of Continuous Fiber Composites, *Journal of Composite Materials*, *41*, 1389.

[8] Vasiliev, V.V., Morozov, E. (2001). *Mechanics and Analysis of Composite Materials*, Elsevier Science, pp. 88-90.

[9] Chapman, T.J. Gillespie, J.W., Pipes, R.B., (1990). Prediction of Process-Induced Residual Stresses in Thermoplastic Composites. *Journal of Composite Materials, 24*, 616-643.

[10] Hahn, H.T. (1976). Residual Stresses in Polymer Matrix Composite Laminates. *Composite Materials, 10*, 264-277.

[11] Anagnostopoulos, G., Parthenios, J., Galiotis, C. (2008). *Thermal Stress Development in Fibrous Composites.* Materials Letters, Volume 62, issue 5, pp. 341-245.

[12] Frost, S.R. (1992). Compressive behavior of long-fibre unidirectional composites. *Journal of Composite Materials*, *26*, 1151-72.

[13] Rosen, B.W. (1964). Tensile Failure of Fibrous Composites. *AIAA preprint No. 64-73*.

[14] Vasiliev, V.V., Morozov, E. (2001). *Mechanics and Analysis of Composite Materials*. Elsevier Science, pp. 97-99.

[15] Jones, R.M., (1999). *Mechanics of Composite Materials, 2nd Ed***,** Taylor & Francis, pp 485-494.

CHAPTER FOUR

THEORETICAL AND EXPERIMENTAL COMPRESSIVE STRENGTH OF A GLASS-RESIN PULTRUDED COMPOSITE

Introduction

Prediction and measurement of unidirectional composite longitudinal compressive strength has been actively studied for almost 50 years. In 1965 Rosen, *et al*.[1] were the first to propose microbuckling as a failure mechanism of a unidirectional composite. There have been many contributions in the ensuing years, the most notable addressing fiber misalignment and matrix nonlinearities. Argon[2] first added initial fiber misalignment to explain kinking. Budiansky[3] proposed a model that unified Argon and Rosen models, with Budiansky and Fleck[4] adding elastic-perfectly plastic matrix assumption effects. Daniel, *et al*.[5] proposed a straightforward method to integrate initial fiber misalignment with measured composite in-plane shear modulus G_{12}. The approach accounted for matrix nonlinearity and misalignment. These studies all showed that initial fiber misalignment plays a dominate role in compressive strength.

The study presented in Chapter 3 proposed the Combined Stress Model to estimate the compressive strength of unidirectional continuous fiber composites. The approach incorporated a fiber misalignment continuum, matrix nonlinearity, thermal prestress, fiber elastic properties, and fiber volume fraction. The study used one validation case having a fiber volume fraction of 0.50, for which the fiber misalignment continuum was measured, and from which

compression test samples were prototyped. Good agreement was achieved between the model estimate for compressive strength (645 MPa) and ASTM D6641 measurements (565 +/-49 MPa).

Chapter 3 also supplied variable sensitivity plots. Hypothetically, the model suggested that a glass-resin composite of identical constituents as the test case, but perfect fiber alignment, would have a compressive strength of 1.3 GPa. This is much higher than values reported in the literature for unidirectional glass-resin compressive strength,[6] This prediction for a volume fraction of 0.50 is about two times higher than any literature value of which the authors are aware.

This study addresses this theoretical prediction by executing the following steps:

1. Prototyping a continuously protruded glass-resin monofilament using the same constituents as the test case presented in Chapter 3.
2. Measuring the fiber misalignment continuum within the monofilament
3. Estimating the monofilament compressive strength with the Combined Stress Model from Chapter 3.
4. Developing a test methodology for measuring monofilament compressive strength.
5. Measuring monofilament compressive strength.
6. Comparing and discussing model predictions and experimental results.

The study also provides electron microscope images of failed monofilament samples, which sheds light on the failure mechanism.

Monofilament prototyping

A monofilament, continuously pultruded glass/resin composite was prototyped and supplied by Michelin Tire Corporation. While details of the pultrusion process were not available, the constituents were identical to the laminate composite test case used in Chapter 3, which are:

- Avantex Owens Corning glass fiber, 16 μm diameter
- Atlac 590 vinyl ester resin

By density measurements, the composite was determined to have a fiber volume fraction of 0.50, average diameter of 1.04 diameter, and cross sectional area of 0.849 mm^2. The resin was polymerized immediately after it was applied to the glass fiber, at a temperature of approximately 180 degrees Celsius.

Fiber misalignment continuum measurement

To measure fiber misalignment in the pultruded monofilament, a razor was used to split the filament in half. An electron microscope image of the transverse cross section is shown in Figure 4.1a. Several fibers were obviously perturbed by the action of cutting the monofilament, as indicated in the figure. Misalignment of the other fibers was measured using the same protocol presented in Chapter 3. A total of 5 images, with 90 individual fiber measurements, were used to determine the misalignment continuum. The result is shown in Figure 4.1b.

Also shown in Figure 4.1b are misalignment measurements taken from a continuously pultruded carbon fiber rod[7]. In this study, fiber alignments were

measured via an automated image analysis procedure. The data was reported at a low resolution of 0.2 deg; nevertheless, there is good agreement between these results and measurements taken in the present study. Both measurements show very small misalignments for continuously pultruded composites, with similar profiles for the misalignment volume fraction relationship.

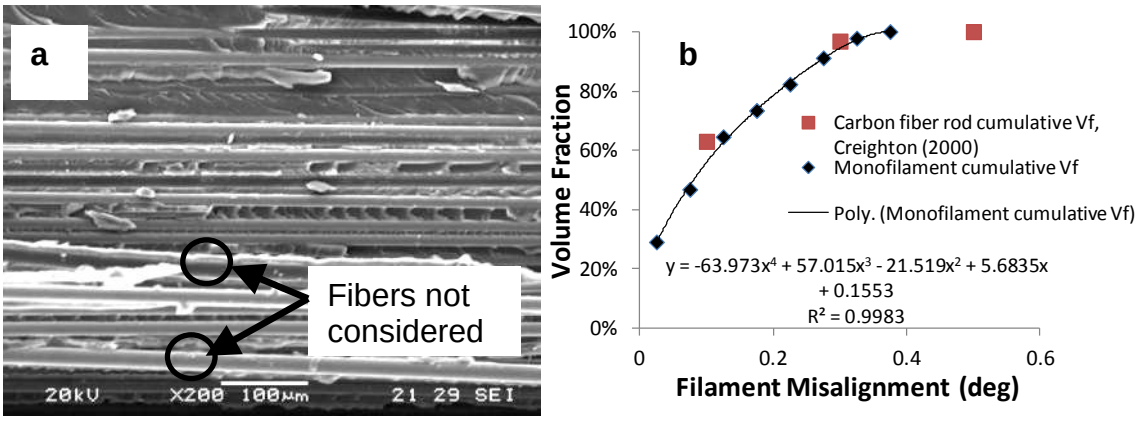

Figure 4.1: Monofilament fiber alignment (a), cumulative volume fraction vs. fiber misalignment, and cumulative volume fraction vs. fiber misalignment from Creighton (2000) for continuously pultruded carbon fiber rod (b)

For continuous pultrusion, approximately 90% of the cross section had a misalignment of 0.25 degrees or less, while for the prepreg laminate, 90% of the cross section had a misalignment of 1.5 degrees or less. These two cases thus represent a large change in one independent variable, as shown in Figure 4.2

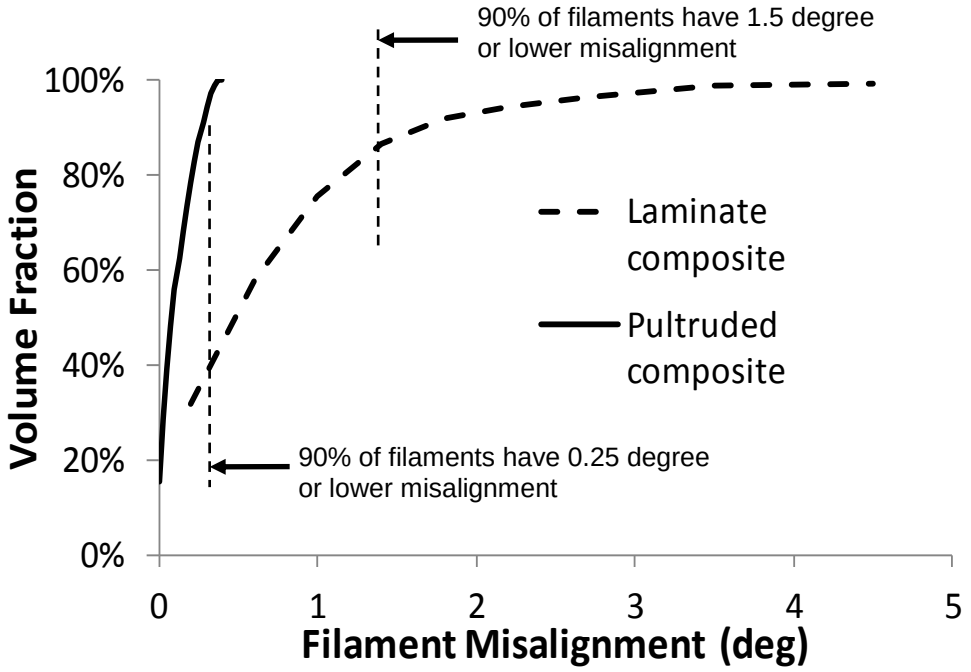

Figure 4.2: Prepreg laminate and pultruded monofilament cumulative volume fraction vs. filament misalignment

Fiber misalignment imposes an in-plane shear stress during longitudinal compression of a unidirectional composite, which interacts with matrix nonlinearity, as noted by Daniel, *et al.* (2006), and verified experimentally by Cho, et al. [8] The induced in-plane shear stress, τ_{12}, relates to the compressive stress, σ_1, and the initial misalignment, φ. For the assumption of small angles, this relationship is defined as given in Equation (1):

$$\tau_{12} = -\sigma_1(\varphi + \Delta\varphi) \qquad (1)$$

This gives rise to additional fiber rotation, $\Delta\varphi$, occurs, as shown in Equation (2).

$$\Delta\varphi = \frac{\tau_{12}}{G_{12}} \qquad (2)$$

The two fiber continuums of Figure 4.2 will result in very different levels of τ_{12}, which in turn results in a matrix shear stress of even higher value. The literature notes that this imposed matrix stress plays an important role in compressive strength, due to matrix nonlinearity; thus, these two composites should behave much differently in compression.

Combined Stress Model calculation

The Combined Stress Model from Chapter 3 was used to calculate test composite compressive strength as a function of homogeneous misalignment. This relationship, reproduced in Figure 4.3, is identical for the laminate test case used in Chapter 3 and the continuously pultrided monofilament considerd in the present study.

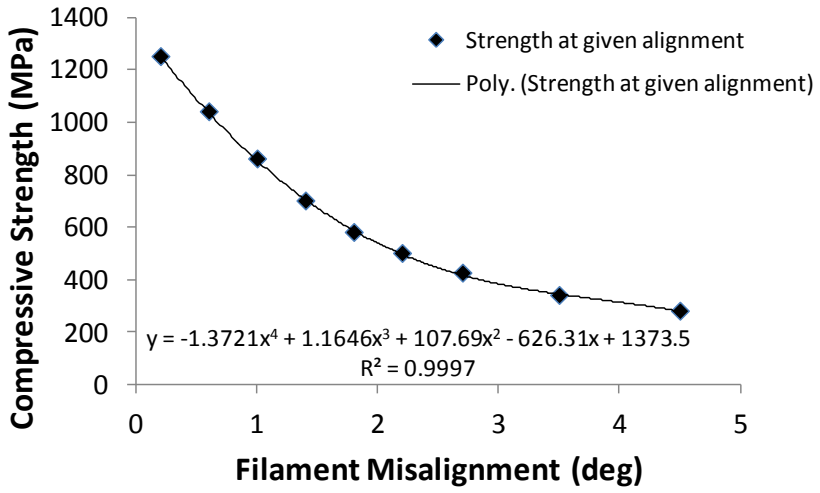

Figure 4.3: Compressive strength vs. homogeneous misalignment for test case from Chapter 3 and the pultruded monofilament

For these calculations, the composite constituent material characteristics were approximated as defined below:

- Vinyl ester resin Atlac 590.
  - Initial tensile modulus E_m = 3.5 GPa.
  - Ultimate σ_t = 90 MPa
  - Stress-strain nonlinearity from measurement and FEA analysis
  - CTE = 3×10^{-5}
- Owens Corning Advantex Glass fiber.
  - E_f = 78 GPa
  - G_f = 30.5 GPa
  - CTE = 5×10^{-6}
  - V_f = 0.50
  - Cure temperature = 180 C, ambient test temperature = 23 C.

The continuously pultruded monofilament used these constituents, volume fraction, and cure temperature as well.

Figure 4.3 presented the compressive strength for uniform misalignment. Calculation of the compressive strength of a composite having a misalignment continuum involves multiplication of the polynomial describing the misalignment cumulative histogram (Figure 4.1b) with the polynomial describing compressive strength vs. homogeneous misalignment (Figure 4.3). This operation is shown in Figure 4.4 for the pultruded monofilament composite.

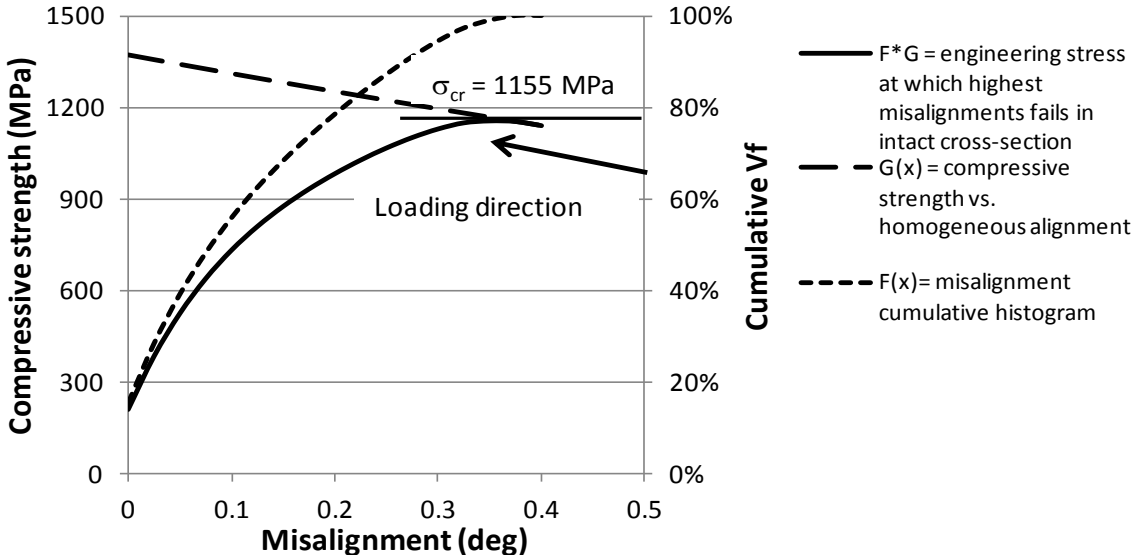

Figure 4.4: Monofilament composite: misalignment histogram (F(x)), compressive strength at homogeneous misalignment (G(x)), and applied stress (F x G) at which highest misalignments in intact section fail

For the pultruded composite, a compressive strength of 1155 MPa is predicted. At this stress, only 1 to 2% of the cross section has already failed. 98% of the cross section abruptly fails at this critical stress.

There exists homogeneous misalignment which gives the same compressive strength as a misalignment continuum. For the laminate composite, this is about 1.5 degrees. With the simplification of a homogeneous

misalignment, the matrix stress state and the composite G_{12} can be represented as functions of applied compressive stress. This is shown for the laminate composite from the test case from Chapter 3 in Figure 4.5.

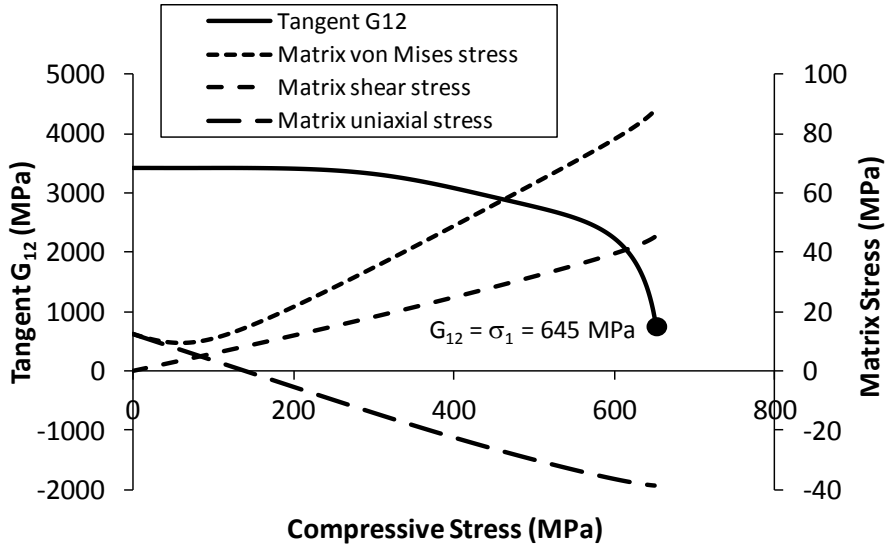

Figure 4.5: G_{12}, matrix compressive, shear, and von Mises stress vs. applied compressive stress for laminate composite misalignment = 1.5 deg.

The equivalent misalignment for the pultruded composite is 0.36 deg. For this case, the matrix stresses and composite G_{12} are shown as functions of compressive stress in Figure 4.6.

The results of Figure 4.5 show that the laminate composite G_{12} equals the applied compressive stress at 645 MPa. In Figure 4.6, this occurs for the pultruded composite at 1155 MPa. The overwhelming difference between the two cases is the induced matrix shear stress. For the laminate case, the matrix shear stress is 45 MPa at the point of shear instability. For the pultruded case – at a compressive stress that is 78% higher – this is only 20 MPa. This higher

induced shear results in a much faster increase in matrix von Mises stress for the laminate case compared to the pultruded case. The result is that the tangent matrix modulus, and thus the tangent G_{12}, begins to rapidly decrease at a much lower compressive stress for the laminate composite.

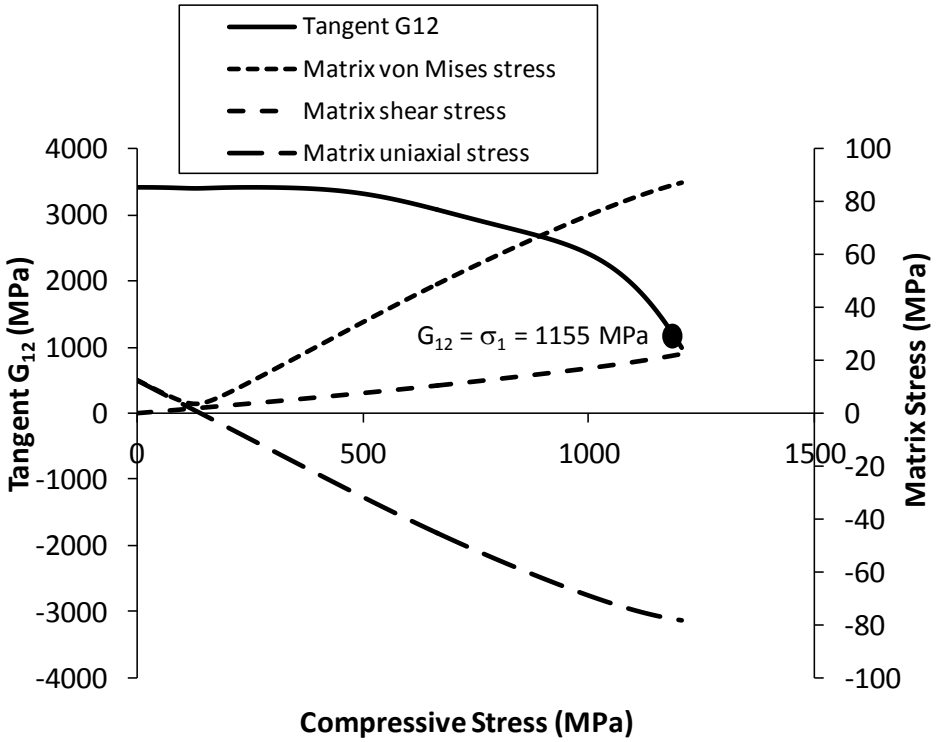

Figure 4.6: G_{12}, matrix compressive, shear, and von Mises stress vs. applied compressive stress for pultruded composite misalignment = 0.36 deg.

Compressive strength test development

Unidirectional compressive strength testing has seen significant evolution over the past several decades.[9] Wegner, *et al*.[10] provided an overview of compression testing methods and results, and then validated a new method which became ASTM-D6641. This method applies the compressive stress to the

composite sample via shear and direct compression. Applying a large portion of the load via shear on the specimen side faces prevents premature failure due to high localized compressive stresses on the ends.

Creighton, *et al*. (2000) developed a novel method of loading a composite rod in compression that used an approach similar to ASTM D6641. A loading support system was designed that included 30 mm long cylindrical holes of slightly larger diameter than the rod specimen. The specimen was adhered with epoxy inside these holes, and end plates were attached. The rod was thus loaded in compression and shear. Various free span lengths were tested.

This study used a method similar to that of Creighton. Compression samples were constructed by adhering the pultruded 1.0 mm diameter monofilament into 6 mm diameter aluminum cylinders that had been drilled with 1.4 mm diameter shaft. This sample was inserted into a test rig that mated to an Instron 5500R machine. Sample and test rig geometry are shown in Figure 4.7.

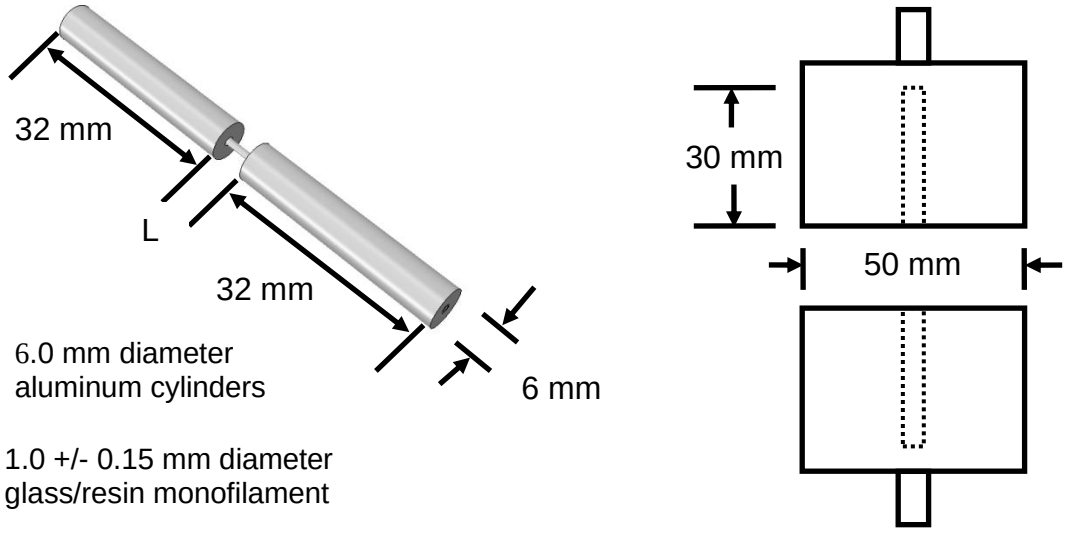

Figure 4.7: Compression sample and test rig construction

A photograph of the test rig with a compression sample inserted is shown in Figure 4.8. Load frame alignment was estimated to be within 0.02 mm. Shimming the bottom fixture gave a slight improvement. The load frame slid with minimal friction up and down the aluminum cylinders of each test specimen.

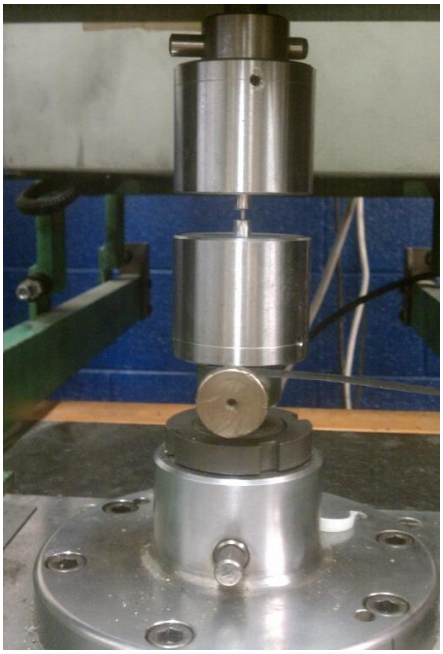

Figure 4.8: Instron machine, test rig, and compression sample

The pultrusion method resulted in constant cross-section area. This was controlled as a result of the constant fabrication speed and fixed die cross-section. However, slight torsions due to fiber unwind resulted in dimensional variation after resin polymerization. The cross section varied from circular to elliptical, with differences between major and minor axes of up to 0.25 mm. Additionally, when the filament was cut to length, a small amount of fraying occurred. For these reasons, the internal cylinder diameter was 1.4 mm.

Materials used in sample prototyping are shown in Figure 4.9.

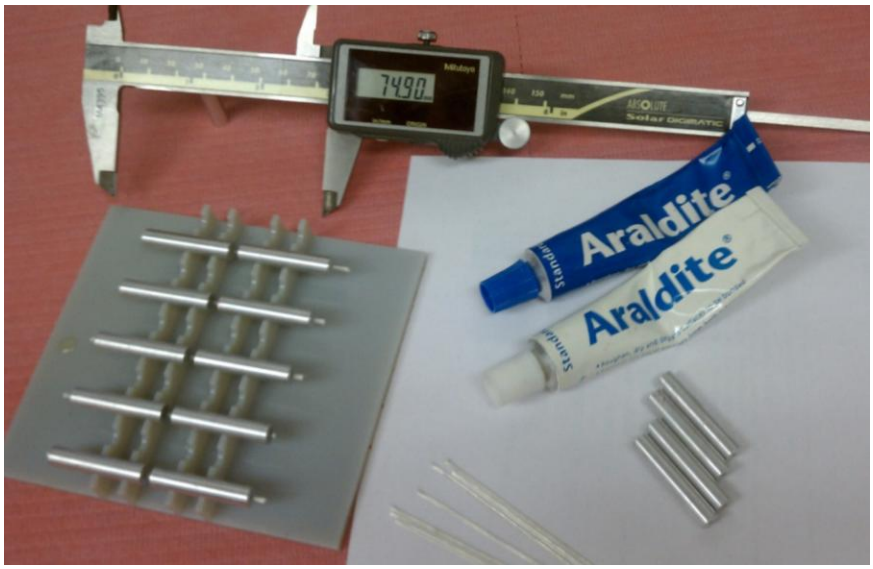

Figure 4.9: Monofilament samples, aluminum cylinders, epoxy, and digital ruler used in sample construction

Three different free span lengths, L, were prototyped: 2, 3 and 4 mm. The reason for this experimentation related to buckling load calculation. The Euler column buckling formula can be modified to include shear deformation. Engesser's formula for critical buckling load provides one approximation, as given in Equation (3)[11]:

$$P_{cr} = \frac{P_{euler}}{1 + \frac{P_{euler}}{GA}} \qquad (3)$$

where P_{euler} is the Euler critical buckling load, G = column shear modulus, A = column cross section area. Assuming a circular cross section, E = 40 GPa, G = 3.3 GPa, and engineering effective free span length = 0.65L, buckling loads and stresses are shown in Table 4.1.

Free Span (mm)	Buckling load, N	Buckling stress, MPa
2	1692	1990
3	1131	1331
4	773	909
5	549	646

Table 4.1: Buckling load and stress for four different free span lengths

Since the Combined Stress Model predicted a critical stress of 1155 MPa, a free span length of less than 4 mm was needed. However, with the longer span of 4 mm, an alignment error would be less penalizing. On the other hand, the values for buckling stress in Table 4.1 may be liberal, as Figure 4.6 indicates that G decreases with increasing compressive stress.

Test alignment variations were related to at least three parameters: (1) the alignment of the test load frame and fixtures; (2) the precision with which the 1.4 mm shaft was drilled in the cylinder center; and (3) monofilament centering in the shaft. Alignment errors due to (1) were considered very small. Variations from (2) were also quite small, as a lathe-mounted drill was used to drill the shaft in the center of commercially obtained aluminum bar stock. However, (3) could result in alignment variations of as much as +/-17 μm. Monofilament dimensions varied, as previously noted, and the cylinder shaft was 35 μm larger than the average monofilament diameter.

For small gauge lengths, alignment error becomes more significant. At 4 mm, a 17 μm error would give a misalignment of only 0.25 degrees. At 2 mm, the error grows to 0.5 degrees. This error is exacerbated because the

compressive force further reduces gauge length. For all of these reasons, three spans were prototyped: 2, 3, and 4 mm. Longer spans reduce misalignment effects, while shorter spans inhibit Euler buckling.

Compressive strength test results

Four 4 mm span samples were tested. Displacement vs. stress is shown in Figure 4.10. The average stress at failure was 0.692 GPa. While three samples were grouped around a compressive failure stress of 0.6 GPa, one sample achieved 0.93 GPa, which was consistent with the results of Table 4.1. Small differences in sample preparation and alignment certainly could play a role, as sample geometries were small and forces were high.

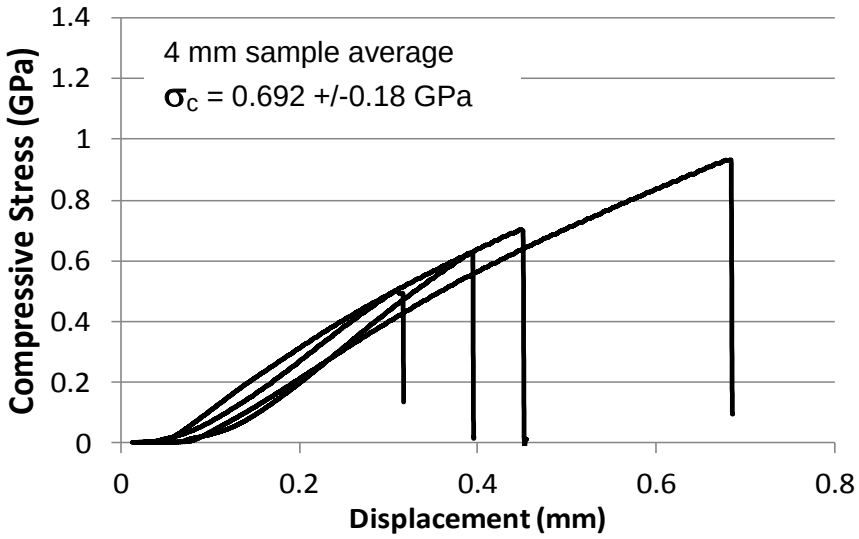

Figure 4.10: Pultruded monofilament stress vs. displacement for 4 samples of 4 mm free span lengths

Four 3 mm span samples gave compressive strength measures shown in Figure 4.11.

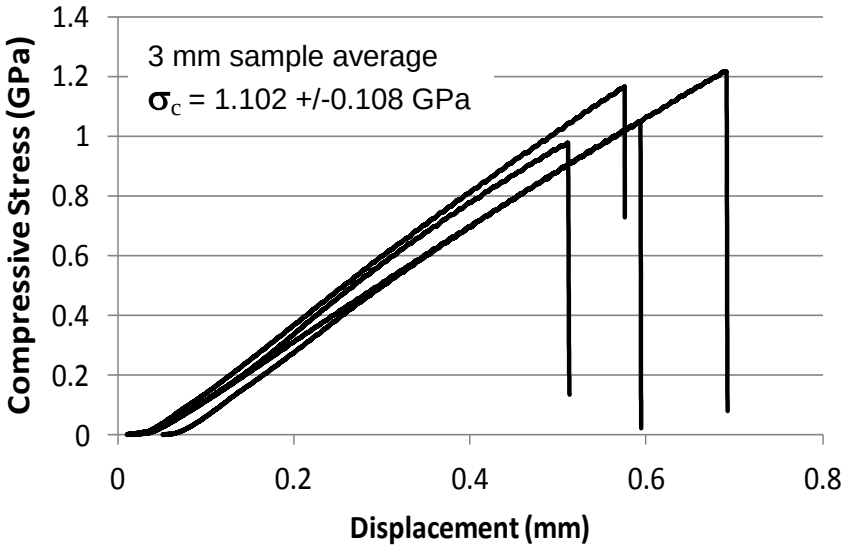

Figure 4.11: Pultruded monofilament stress vs. displacement for 4 samples of 3 mm free span lengths

Four 2 mm span samples gave compressive strength measures shown in Figure 4.12.

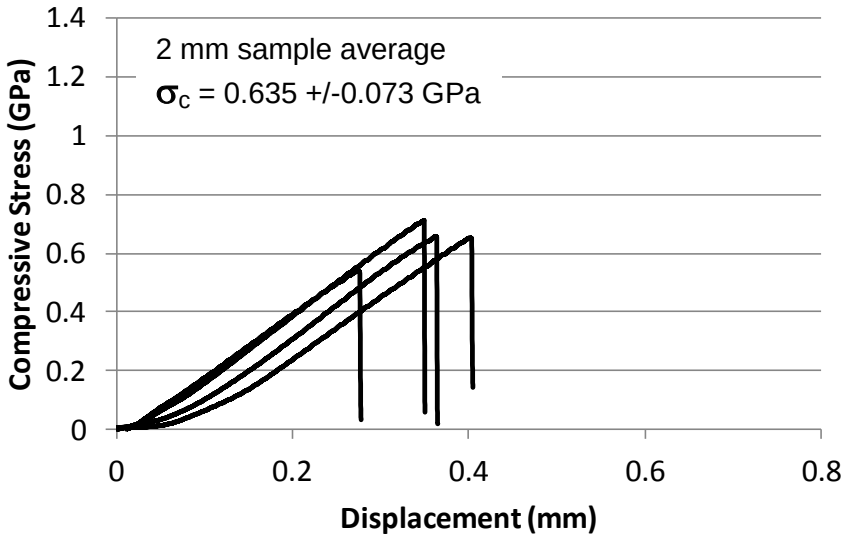

Figure 4.12: Pultruded monofilament stress vs. displacement for 4 samples of 2 mm free span lengths

Significant variations in results were noted as a function of span length, as compiled in Table 4.2.

Compressive span length (mm)	Compressive stress at failure (GPa)	Highest value of any sample (GPa)
2	0.635 +/-0.073	0.714
3	**1.102 +/-0.108**	**1.216**
4	0.692 +/-0.180	0.931

Table 4.2: Buckling load and stress for three different free span lengths

Both average failure stress and maximum failure stress was maximized using the 3 mm free span length. It is theorized that the longer span penalized compressive strength due to columnar buckling, while alignment imperfections penalized the shorter span. For this particular test apparatus, protocol, and monofilament dimensions, the 3 mm span was therefore taken to most accurately represent the true compressive strength of this particular pultruded composite.

Table 4.3 compares the laminate composite from Chapter 3 and the monofilament 3 mm span results to predictions from the Combined Stress Model.

	Model Prediction	Test Result Average	Model / test result
Laminate composite	0.645 GPa	0.565 GPa	+14.1%
Pultruded composite L = 3 mm	1.155 GPa	1.102 GPa	+5%

Table 4.3: Compressive strength measurement and Combined Stress Model prediction for laminate and pultruded samples

For the laminate composite, the model overpredicted compressive stress by about 14%. For the pultruded composite, the model overpredicted

compressive stress by only 5%. For both model and measurement results, the pultruded composite outperformed the laminate composite by almost a factor of 2. Taking into account the reasons why the level of theoretical strength is difficult to achieve, the results of Table 4.3 are excellent. For example, interlaminar effects could degrade the compressive strength of the laminate composite, and this is not considered in the combined stress model. Furthermore, this failure mechanism is more likely to be significant in the laminate composite.

Using a scanning electron microscope, two 3 mm test specimens from the pultruded composite were analyzed. Two images are shown in Figure 4.13. The first specimen (4.13a) achieved a compressive strength of 0.955 GPa. The second specimen (4.13b) had a compressive strength of 1.17 GPa. A very distinctive 45 degree failure plane is evident across the majority of the section in (4.13a) and across the entire section in (4.13b). This indicated sudden failure in pure shear, suggesting that the sample preparation and test protocol successfully eliminated Euler buckling in the 3 mm sample.

While SEM images are not available from the laminate composite after ASTM D6641 testing, a close-up photo of the failed region is shown in Figure 4.14. Four 45 degree failure lines can be seen. However, there are obvious signs of some interlaminar failure and splitting. As previously noted, this is not taken into account by the Combined Stress Model.

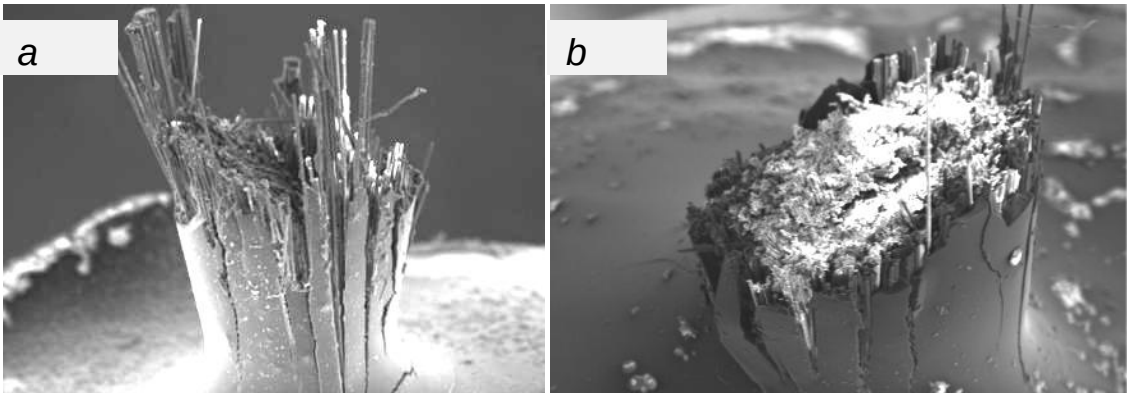

Figure 4.13: SEM images from two failed 3 mm pultruded composite. Measured compressive strength was 0.995 GPa (13a) and 1.17 GPa (13b)

Figure 4.14: Laminate composite specimen after ASTM D6641 testing. Measured compressive strength was 0.56 MPa

Compressive strength values of the putruded Avantex/vinyl ester 3 mm span monofilament are much higher than those reported in the literature, as far as the authors have been able to determine. This is shown in Figure 4.15, as well as the laminate composite from Chapter 3. Combined Stress Model predictions of Avantex/vinyl ester composite with perfect alignment are also provided. The pultruded composite empirical result approaches the theoretical maximum.

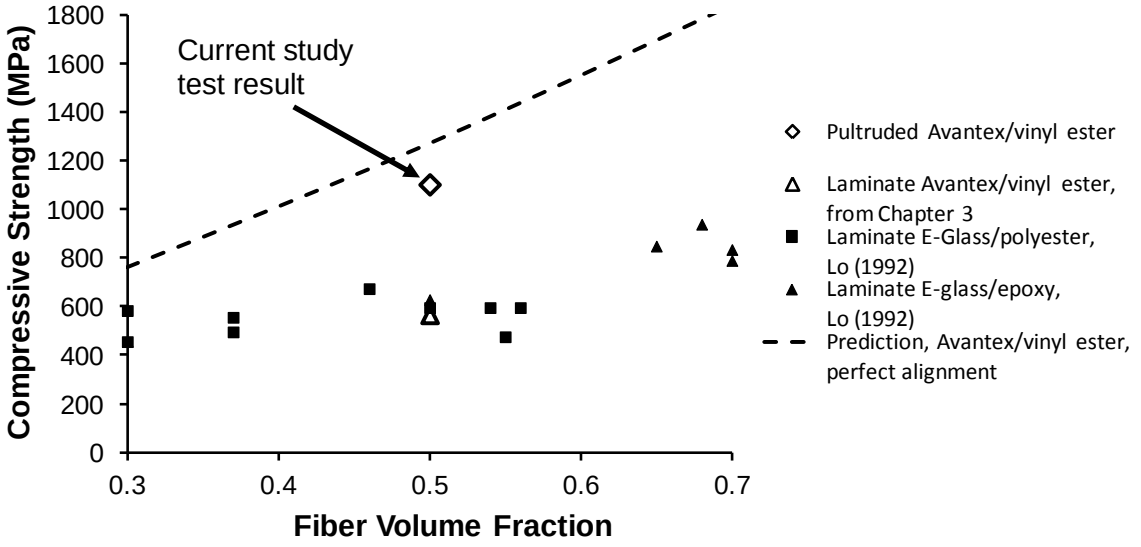

Figure 4.15: Compressive strength of glass-resin composites from Lo (1992), Chapter 3 test case, current study pultruded composite, and Combined Stress Model prediction for the case of perfect alignment

Discussion

The literature often associates unidirectional compressive strength with fiber characteristics. These include fiber bending stiffness[12], a low-modulus interphase between fiber and matrix that varies in importance relative to fiber size[13], size effect on collimation[14], and fiber anisotropy.[15 16] This study shows

that an isotropic, amorphous, relatively low modulus, and small diameter glass fiber composite is capable of high compressive strength.

The study provides two different validation aspects to the Combined Stress Model. First, the model correctly predicted the magnitude of gain in compressive strength of a glass/resin composite when fiber alignment was improved. Second, the model posits that compressive failure occurs via matrix shear instability, with the obvious caveat pertaining to highly anisotropic fibers that have poor shear strength, such as aramid. Microscopic images of the failed pultruded sample show a shear failure, not a buckling failure. This was the case, even though the glass fibers had a compressive strain of about 2.8% at the compressive load of 1.1 GPa. Indeed, the pure shear failure suggests that matrix shear strength was the weak link, not glass compressive strength.

Theoretical developments and experimental validations can be particularly valuable when they inform practical engineering considerations. This study quantifies gains in one important performance – compressive strength – to measureable, quantifiable variables linked to process. Reducing fiber misalignment and interlaminar thickness necessitate process improvements, which require capital investment. Gains in performance can be quantified, and cost-benefit analyses can be performed.

Finally, this study highlights the difficulties associated with unidirectional compressive strength testing. With this particular unidirectional pultruded monofilament, test span differences of 1mm were shown to have a major impact

on measured results. Through experimentation across a range of reasonable values, a particular free span length was found that gave measured compressive strengths that approached a theoretical maximum.

Conclusions

1. A test method has been developed that permits accurate compressive strength testing of a 1 mm diameter monofilament glass/resin pultruded composite.
2. This pultruded glass/resin composite was measured to have very low fiber misalignments, with 90% of the cross section having misalignments lower than 0.25 degrees.
3. Using a 3 mm free span, or length to diameter ratio of 3, compressive strength of this pultruded glass/resin composite was measured at 1.10 GPa.
4. The Combined Stress Model successfully predicted the large difference in compressive strength of this pultruded composite vs. an equivalent laminate composite on an absolute scale. The relative difference compared to a laminate composite having the same constituent materials was also well predicted.
5. The pultruded monofilament failed in what appears to be pure shear.
6. These results supply additional validation of the Combined Stress Model proposed in Chapter 3.

References

[1] Dow, N.F., Rosen, B.W. (1965). Evaluations of Filament-reinforced Composites for Aerospace Structural Applications. *NASA CR-207.*

[2] Argon A.S.(1972) Fracture of Composites in Treatise on Materials. *Science and Technology*. Academic Press, New York.

[3] Budiansky B. (1983) Micromechanics, *Comput Struc 16, 3-12.*

[4] Budiansky B., Fleck N.A. (1993). Compressive failure of fiber composites, *J. Mech Phys Solids* 41:183-211.

[5] Daniel, I.M., Ishai, O. (2006*). Engineering Mechanics of Composite Materials*, *2nd Ed.,* Oxford University Press, Inc., New York, pp. 107-109.

[6] Lo, K.H., Chim, E.S. (1992). Compressive Strength of Unidirectional Composites. *Journal of Reinforced Plastics and Composites*, 11: 838-96.

[7] Creighton, C., Clyne, T. (2000). The compressive strength of highly-aligned carbon-fibre/epoxy composites produced by pultrusion. *Composites Science and Technology 60*, 525-533.

[8] Cho, J., Chen J.Y., Daniel, I.M. (2007). Mechanical enhancement of carbon fiber/epoxy composites by graphite nanoplatelet reinforcement. *Acta Materialia Inc*., Elsevier Ltd.

[9] Wolfe R., Weiner, M. (2004). Compression Testing – Comparison of Various Test Methods, Composites 2004 Convention and Trade Show, American Composites Manufacturers Association, October 6-8, Tampa, FL.

[10] Wegner, P., Adams, D. (2000). Verification of the Combined Load Compression (CLC) Test Method, U.S. Department of Transportation, Federal Aviation Administration, Office of Aviation Research, Washington DC 20591, Grant 94-G-009, Report DOT/FAA/AR-00/26.

[11] Attard, M., Hunt, G. (2008). Column buckling with shear deformations – A hyperelastic formulation*. International Journal of Solids and Structures*, *45*, 4322-4399.

[12] Vasiliev, V.V., Morozov, E. (2001). *Mechanics and Analysis of Composite Materials*. Elsevier Science, pg 112.

[13] Dharan, C.K.H., Lin, C.L. (2007). Longitudinal Compressive Strength of Continuous Fiber Composites. *Journal of Composite Materials*, *41*,1389.

[14] Rosen, B.W. (1987). Analysis of Material Properties, In *Composites, Volume 1: Engineered Materials Handbook* (pp 197-198). ASM International.

[15] Diefendorf, R. J. (1987). Carbon/Graphite Fibers, In *Composites, Volume 1: Engineered Materials Handbook* (pp 50-52). ASM International.

[16] Daniel, I.M., Ishai, O. (2006*). Engineering Mechanics of Composite Materials*, *2nd Ed.,* Oxford University Press, Inc., New York, pg 29.

CHAPTER FIVE

FINITE ELEMENT MODELING OF UNIDIRECTIONAL COMPOSITE COMPRESSIVE STRENGTH

Introduction

Unidirectional composite compressive strength is recognized to be less than tensile strength. Many theories have been advanced to explain this, beginning with Rosen and Dow[1] in 1965. This work advanced the idea of fiber microbuckling as a compressive failure mechanism. The ensuing 45 years have seen many studies that refine and supplant Rosen and Dow's original treatise, with fiber alignment[2 3], matrix nonlinearity[4], and matrix modulus gradients[5] being proposed as deleterious elements that reduce strength in composites.

A number of studies have applied finite element analysis to investigate composite compressive behavior. Compressive instability and compressive modulus have been modeled with FEA in a variety of methods. Wisnom[6] used a 2D approach to predict compressive strength that relied on test measurement of actual composites for shear and transverse stiffness, yet showed the influence of boundary conditions on compressive strength. Lee and Waas[7] discretized fiber and matrix in 2D modeling, predicting a splitting failure mode for glass composites. Yerramalli and Waas[8] developed a 3D approach for compressive analysis and suggested that fiber size could influence compressive strength. Garnich and Karami[9] used a 3D unit cell approach to predict compressive stiffness of composites having fiber waviness.

The current study starts with a two-dimensional analysis of Rosen's development, making use of a 2D unit cell FE model that gives the same results as Rosen. A key point is the recognition of the kinematics associated with deforming a continuous fiber unidirectional composite in compression, resulting in the implementation of appropriate boundary conditions. In successive fashion, modeling complexities corresponding to physical realities are added, including an improved method of modeling the nonlinear compressive behavior of the matrix. Finally, a 3D unit cell FE model is presented that is comprehensive in nature. Straightforward examples are provided that show the capability to quantify effects of many factors linked to changes in compressive strength: fiber alignment, uniformity of fiber spacing, fiber cross-section shape, fiber modulus, and matrix nonlinearities. Comparison to experimental results from the literature is provided.

This FE modeling verifies several of Rosen's assumptions, such as the appropriateness of ignoring fiber bending stiffness. Using ABAQUS perturbation analysis, this study shows that the in-phase shear mode is indeed the dominant mode for compressive instability. Higher modes are series assemblages of the shear mode, with inconsequential change in bifurcation eigenvalues.

Thermally induced matrix prestress can influence compressive behavior. For common matrix and fiber properties, thermal prestress can have a low to moderately beneficial impact on compressive strength[10]; yet, this depends greatly on manufacturing methods. While FEA can certainly model thermal effects, they are not considered in this study.

Unit Cell Boundary Conditions

Imposing a shear deformation

Chapter 3 showed that a composite unit cell could be analyzed using a simple statics approach, taking into account the imposed deformation field. This is easily extended to a 2D fiber / matrix unit cell, as shown in Figure 5.1.

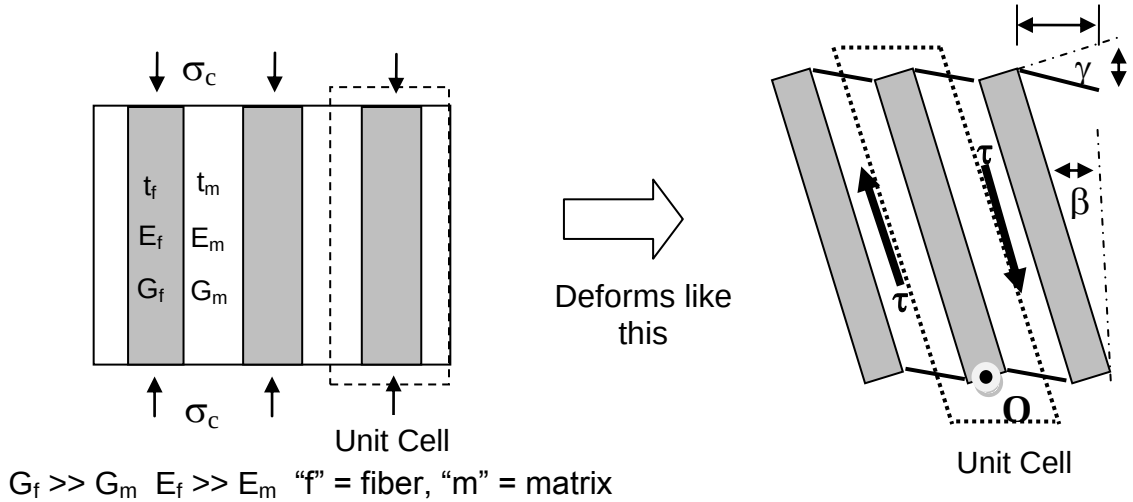

$G_f >> G_m$ $E_f >> E_m$ "f" = fiber, "m" = matrix

Figure 5.1: Shear instability for idealized 2D composite

Employing Rosen's assumptions of a long buckled wavelength and very high fiber shear stiffness, Rosen's original result of Equation (1) can be reproduced via summation of moments:

$$\sigma_c = G_m \frac{1}{1 - V_f} \qquad (1)$$

The kinematics presented in Figure 5.1 and the resulting expression of Equation (1) are central to understanding the compressive behavior of composites. Taken together, they state that:

a) At the micro level, a unidirectional composite deforms only in shear. In Euler beam theory, shear stiffness is high compared to bending stiffness; thus, deformation is in bending alone. The physics of the problem at hand are exactly the opposite; i.e.:

$$\frac{EI}{L^2} \gg GA \tag{2}$$

For an infinite foundation width, noting that composite E in the fiber direction is driven by fiber and in-plane G is driven by matrix stiffness, and noting that moment of inertia varies as width cubed and area varies as width, Equation (2) is true from inspection.

b) The composite in-plane shear stiffness equals the compressive strength. As noted in Chapter 3, Equation (1) is a 2D idealization; the general form is:

$$\sigma_c = G_{12} \tag{3}$$

Equations (2) and (3) inform physical understanding and modeling approach. It is understood that pertinent deformation will occur in shear, and composite shear stiffness is fundamentally important. Modeling must only allow shear deformation and it must accurately model shear stiffness.

It follows that a unit cell finite element boundary conditions should be consistent with the deformation field shown in Figure 5.1. To accomplish this, the following objectives should be met:

a) Individual fibers must freely rotate on the top and bottom boundaries. This agrees with observations made by Cho, *et al.* [11].

b) The left and right unit cell sides must be tied together such that it approximates an infinite domain that deforms only in shear and compression at the micro level. Figure 5.2 shows a method by which this can be achieved, with discretization of fiber and matrix.

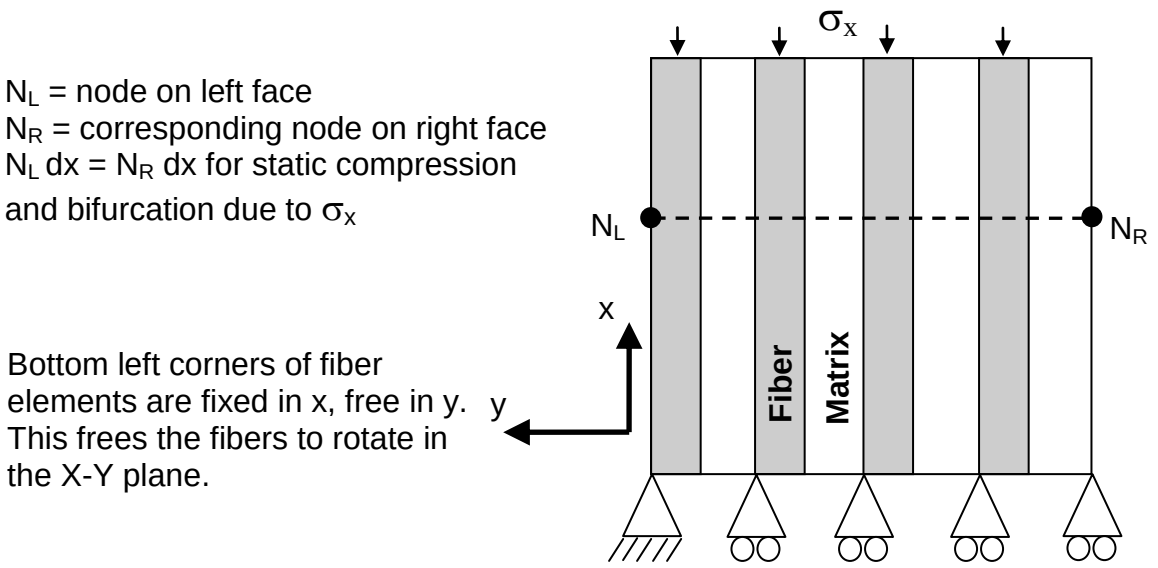

Figure 5.2: Boundary conditions for fiber rotation and unit cell shear

These boundary conditions allow the deformation modes on the unit cell as shown in Figure 5.3. In Figure 5.3a, which depicts pure static compression, left and right face nodes are tied in X. This enables the Poisson effect. Figure

5.3b shows that this boundary condition also allows simple shear, which can be combined with compressive deformation, as shown in the illustration. Horizontal sections remain horizontal, and the unit cell is only free to compress and shear. There is no bending deformation because, as demanded by Equation (2), bending stiffness is very large compared to shear stiffness.

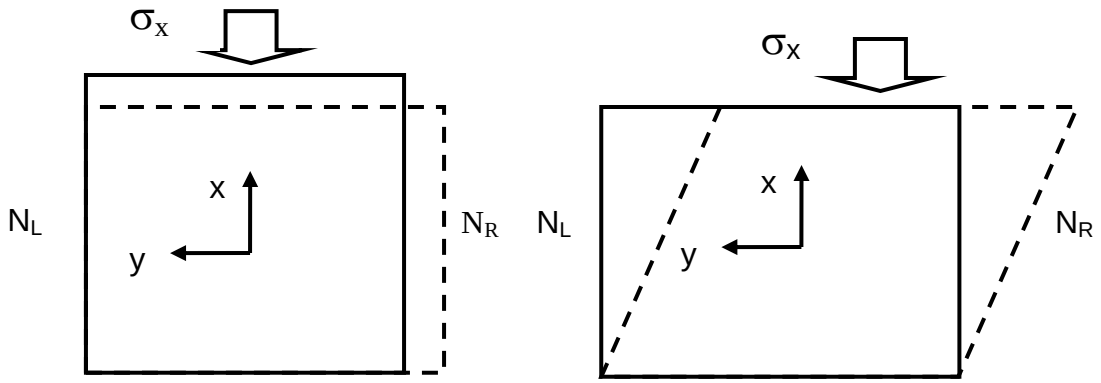

a: compression: left face and right face nodes tied in X, permitting Poisson effect.

b: shear: left face and right face nodes are tied in X, permitting shear, not bending.

Figure 5.3: Deformation mode imposed by left and right face B.C.

While more complicated, 3D discretization and appropriate boundary conditions are analogous.

Use of Saint Venant's principle

Figures 5.1 and 5.2 conveniently depict the compressive stress, σ_x, as being applied only on the reinforcement. For the most common unidirectional composites, the reinforcement is at least 20 times stiffer than the matrix, and this is a reasonable approximation. However, it is not rigorously correct; moreover,

the next section will reveal the importance of matrix nonlinearity, which depends on the matrix deformation state. For this reason, boundary condition effects were carefully studied.

When modeling composites, other researchers have faced this problem. Francescato, et al[12] modeled the torsional behavior of composite beams using FEA, with uncertainty in the appropriate support boundary conditions. In comparing results to closed form solutions, they found several boundary condition specifications that gave global response similar to the Saint Venant solution for beams that were suitably slender. Alpdogan, et al[13] studied transitional effects of joined composite beams. They noted that transitional effects decayed to the Saint Venant solution at about z/a = 2, where z = axial distance from the joint and a = beam thickness.

Most similarly to the present study, Wongsto, *et al*.[14] addressed the effects of randomly spaced fibers within the cross-section of a unidirectional composite. They separately discretized fiber and matrix in a micromechanical modeling approach. With randomly spaced fibers, the boundary condition is neither stress nor displacement controlled. Their goal was to determine the necessary distance between an incorrectly prescribed boundary condition and a representative volume element (RVE), in order for the RVE to behave as though the boundary condition was correct. As per the Saint Venant principle, the stipulation was that the incorrect boundary conditions be statically equivalent to those in the exact system. They found that boundary condition effects became negligible at a

distance of twice the center-to-center fiber spacing away from the boundary. For the most common glass and carbon fiber composites, this gives a distance on the order of 30 to 40 μm.

To study boundary condition effects, the model shown in Figure 5.4 was used. A 2D unit cell was defined having V_f = 0.50, and matrix and fiber of 10 μm thickness. The matrix was placed in the unit cell center, the fiber was split into two halves, and left/right symmetry was imposed. The bottom face was fixed in X, and free to slide in Y. Figure 5.4a defines boundary stresses and material moduli for 4 study cases, and Figure 5.4b shows model geometry.

	σ_F (GPa)	σ_M (GPa)	E_F (GPa)	E_M (GPa)
Case 1	1.0	1.0	40.0	40.0
Case 2	2.0	0.0	40.0	40.0
Case 3	1.925	0.075	77.0	3.0
Case 4	2.0	0.0	77.0	3.0

a

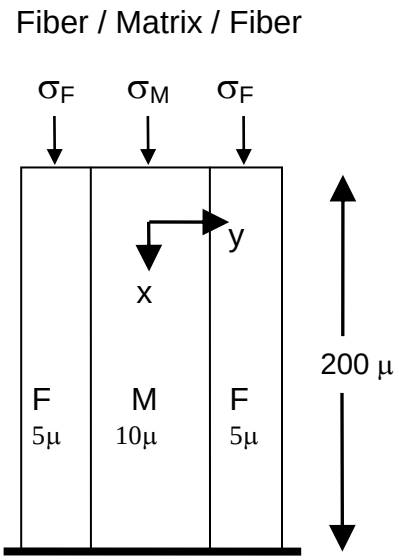

b

Figure 5.4: FEA model used to study boundary condition effects: Model parameters (a) and model geometry (b)

Case 1 is homogeneous for both stress and modulus. With a modulus of 40 GPa and applied stress of 1.0 GPa, the engineering strain in X equals -0.025.

Abaqus reports Green-Lagrange strain, which equals -0.0246. Case 2 represents a most severe case for boundary condition error. E_F and E_M are equal, yet all the stress is applied to the fiber. Case 3 has material properties that approximate those of a glass-resin composite. The moduli are defined such that the composite stiffness in X is identical to that of Cases 1 and 2. The strain results of

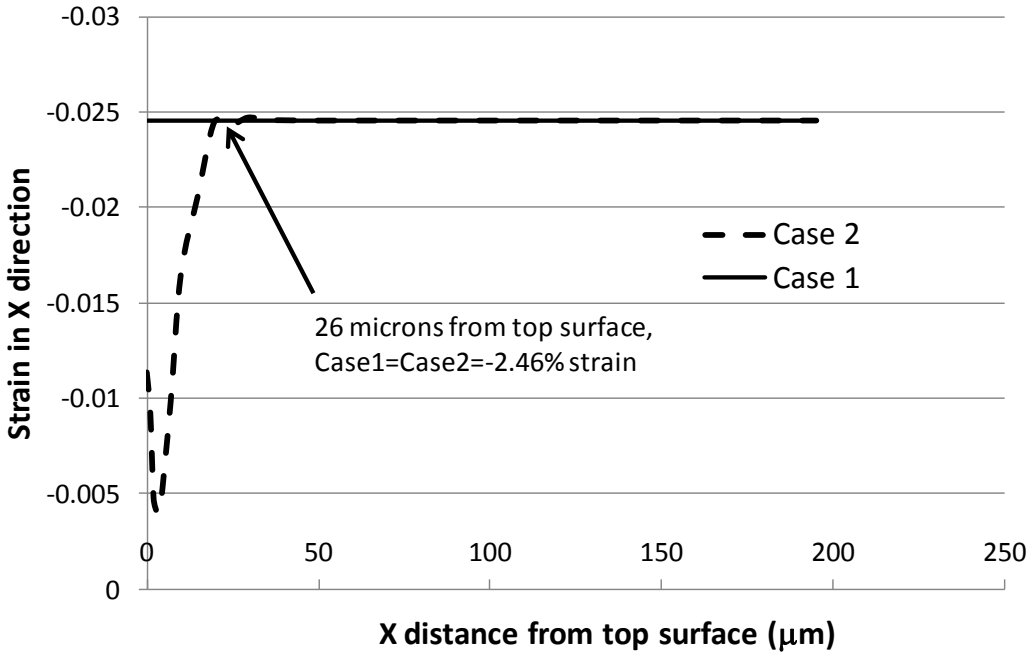

Figure 5.5: FEA results for Cases 1 and 2: matrix X strain as function of distance from boundary condition

Case 3 should be identical to Case 1, as the applied pressures are scaled according to the moduli. Case 4 has the loading condition proposed in Figures 1 and 2, and is a linear modulus approximation of a glass-resin composite.

The matrix strain in X is shown in Figure 5.5 for Cases 1 and 2. Case 1, with homogeneous material and applied stress, has constant X strain of -0.0246,

which agrees with theory. Matrix compressive strain reaches the homogeneous value at a distance of 26 μm from the applied stress.

Results for Cases 3 and 4 are shown in Figure 5.6. Case 3 gave identical matrix strain results as Case 1, as expected. Case 4 obtained the same value of compressive strain at a distance of 35 μm from the top surface.

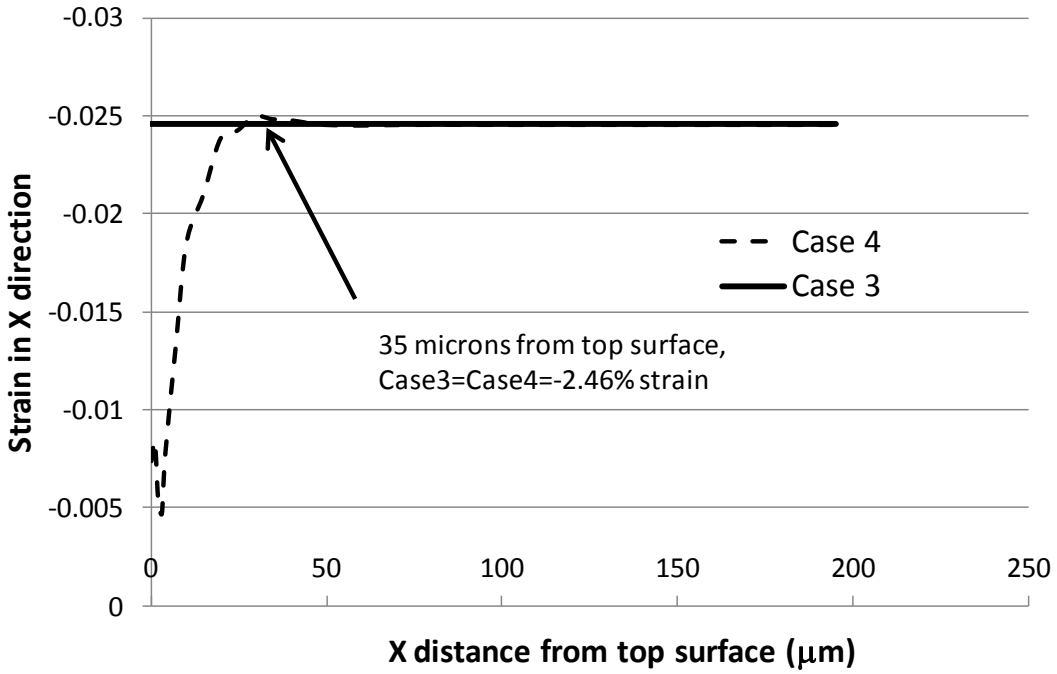

Figure 5.6: FEA results for Cases 3 and 4: matrix X strain as function of distance from boundary condition

The results of this simple study agreed with the findings of Wongsto, *et al.* (2005). At a distance of around 2 times the center-to-center fiber distance, the matrix strain and stress state match the far-field value, provided the Saint Venant condition of static equivalence is met. Therefore, in this study, stresses will be applied only on the fiber cross sections. Model length will be large compared to fiber diameter, such that these boundary effects are negligible

Matrix Material Law

The literature acknowledges the importance of the nonlinearity of the matrix when modeling compressive strength of unidirectional composites. When FEA has been applied to this problem, a common material law has been the von Mises plasticity model with isotropic hardening. This law, usually employed for non-ferrous metals, is implemented in several commercial codes, including ABAQUS. An elastic uniaxial modulus and Poisson's ratio are entered, as well as multiple uniaxial yield stresses. A plastic strain corresponding to each yield stress is given, thereby enabling a fit to uniaxial nonlinear behavior. This classical plasticity approach was taken by Xu *et al*.[15], Lee, *et al.* (1999), and Yerramalli, *et al.* (2004) in micromechanical modeling of composites of polymeric resins and fibers. This approach gave very good matrix uniaxial performance, by definition. Lee, *et al.* (1999) also verified that the approach gave reasonable agreement to experimental measures for loading in pure shear.

In a unidirectional composite having very high fiber stiffness, such as carbon or boron, along with moderate to high fiber volume fraction, there is very little strain in the fiber direction. Therefore, the matrix experiences relatively little compressive strain. However, with low fiber volume fraction, or a lower modulus fiber, such as glass, fiber compressive strain can be significant. For these cases, it is vital to correctly model the shear stiffness of the matrix under combined compressive and shear loading. This is especially true if parametric modeling

comparisons are made, by which the effects of fiber modulus, alignment, and volume fraction on compressive strength are estimated.

Studies providing empirical measurements of resin shear modulus as a function of compressive stress are quite limited, as far as the authors have been able to determine. One paper by Liang *et al*.[16] reported effects of superimposing compression on shear for an epoxy resin sample. The load vs. displacement slope decreased as shear increased. However, stress and strain information was not provided. Most germane to the current study, Hayashi[17] specifically addressed the evolution of shear modulus under compression for Epikote 828, which is an epoxy resin. Using a novel test specimen and fixture, initial shear stiffness was measured at increasing levels of compressive stress. Normalizing matrix shear modulus, G_m, by the stress-free initial shear modulus G_0, he found the shear modulus evolution of four samples as reproduced in Figure 5.7.

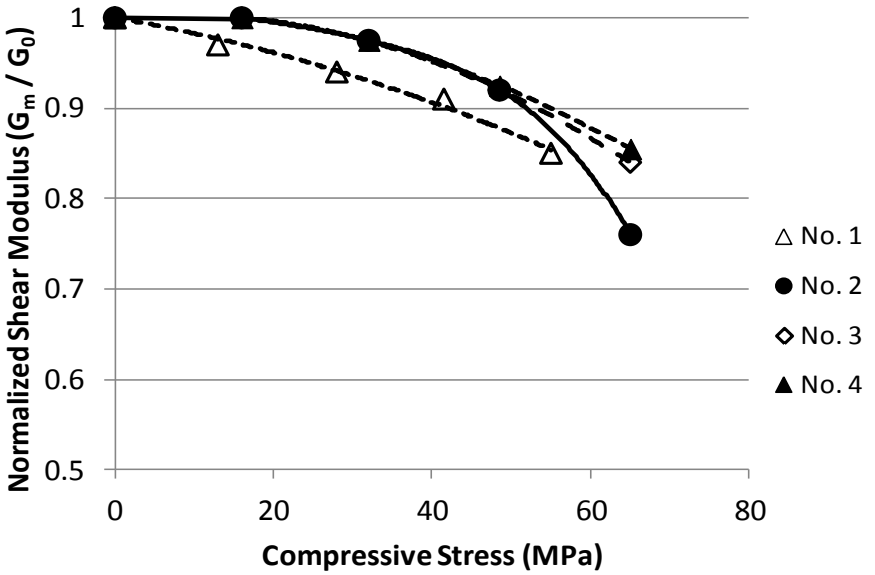

Figure 5.7: Normalized shear modulus reduction as a function of compressive stress for epoxy Epikote 828, Hayashi (1985)

Figure 5.7 shows a drop in shear modulus of 15 to 25% at a compressive stress of 60 MPa. To put this in the context of a unidirectional composite, consider an E-glass- resin composite with $V_f = 0.50$. The fiber axis modulus is about 38 GPa. A compressive strength of 700 MPa – a reasonable value from the literature - would result in fiber (and matrix) compressive strain of around 1.9%. With an initial Young's modulus of 3.23 GPa, Epikote 828 develops a stress of 60 MPa at 1.9% strain. Thus, the results of Figure 5.7 are quite pertinent in understanding and modeling compressive strength.

Using plastic deformation with isotropic hardening, the two elastic constants, E and υ, explicitly define the elastic shear modulus, G, per Equation (4). E and G are thus directly related because υ is a constant.

$$G = \frac{E}{2(1+\upsilon)} \qquad (4)$$

However, polymers are viscoelastic in nature, with significant loss angle and creep at room temperatures.[18] [19] More significant for the current study, Poisson's ratio is not a constant. O'Brien, *et al*.[20] showed that creep and Poisson's ratio were related for an epoxy. Under constant stress, Poisson's ratio increased, approaching 0.50 for long creep times. Usual Poisson's ratio values reported for polymeric resins vary from 0.30 to 0.40.

Maksimov *et al.* [21] measured Poisson's ratio as a function of compressive stress for a vinyl ester resin. Poisson's ratio was found to vary significantly under compressive stress. Their results were reported in a graphical form, which is reproduced in Figure 5.8. Poisson's ratio was found to linearly increase with increasing compressive stress, until the compressive strength of 125 MPa was approached. At this point, Poisson's ratio rapidly increased to 0.50, representing an incompressible state. With reference to Equation (4), such an evolution in Poisson's ratio would decrease shear modulus with compressive stress, even for a constant Young's modulus. From this perspective, Maksimov, *et al.* (2005) offers a partial explanation to the empirical results reported by Hayashi (1985).

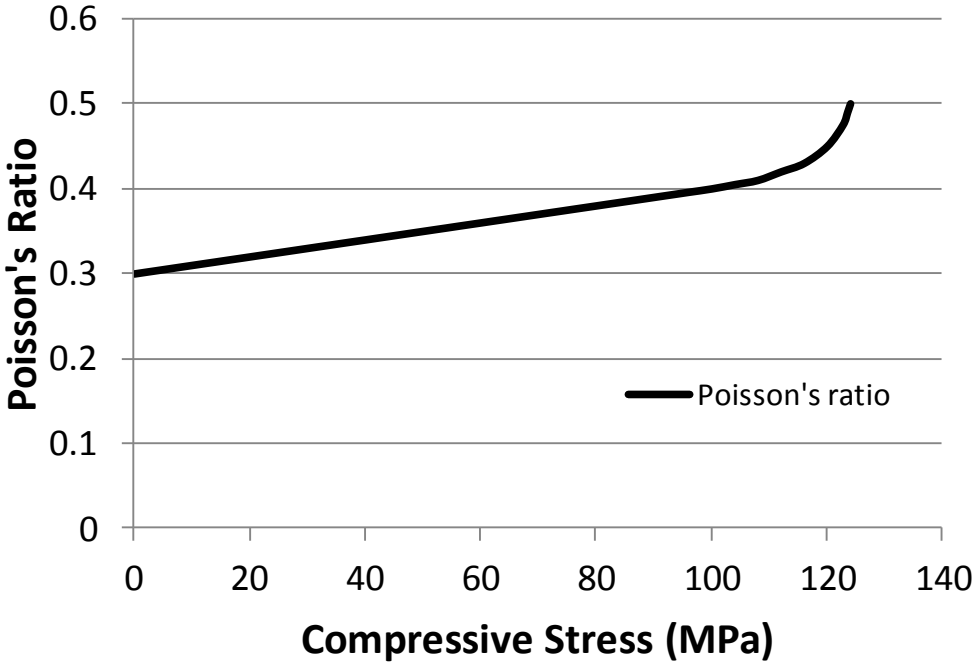

Figure 5.8: Poisson's ratio vs. uniaxial compressive stress for a vinyl ester resin, Maksimov (2005)

ABAQUS offers the ability to add user defined fields to material laws. With this feature, one can define multiple paired values of Young's modulus and Poisson's ratio, enforcing values relative to the defined field. If this field is the von Mises stress, the elastic constants can be assigned as a function of this one positive, scalar quantity. Figure 5.9 shows how the material properties can be implemented into ABAQUS using the measured uniaxial stress vs. strain of Epikote 828 supplied by Hayashi (1985), and Poisson's ratio evolution of Figure 5.8. Poisson's ratio evolution is scaled to account for differences in resin ultimate compressive strength from Hayashi (100 MPa) and Maksimov (125 MPa). Uniaxial stress is the von Mises stress, making implementation straightforward.

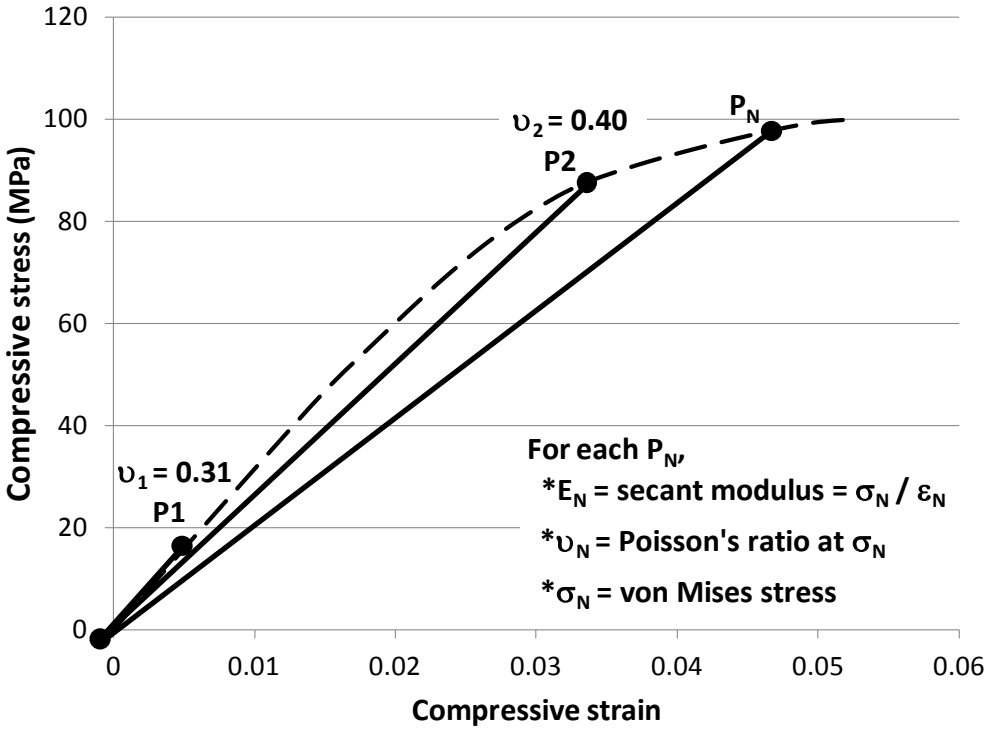

Figure 5.9: Compressive stress vs. strain for Epikote 828, Hayashi (1985), with several secant modulus and Poisson ratio values shown. Uniaxial stress equals von Mises stress.

In the Elastic material card, one therefore has “N” lines of material constants. Any number of points can be used. A user defined subroutine in Fortran 77 returns von Mises stress, as defined in Equation (5). The user subroutine and material constants E_N and υ_N at each σ_N for Epikote 828 are given in Appendix B, along with further ABAQUS implementation details.

$$\sigma_v = \sqrt{\frac{1}{2}[(\sigma_{11}-\sigma_{22})^2+(\sigma_{22}-\sigma_{33})^2+(\sigma_{33}-\sigma_{11})^2+6(\sigma_{12}^2+\sigma_{23}^2+\sigma_{31}^2)]} \quad (5)$$

Using this characterization of Epicote 828, a linear plane stress one element model (CPS4) was solicited in simple shear. Element response was compared to the response achieved from the elasto-plastic assumption with isotropic hardening. Results for pure shear solicitation are shown in Figure 5.10.

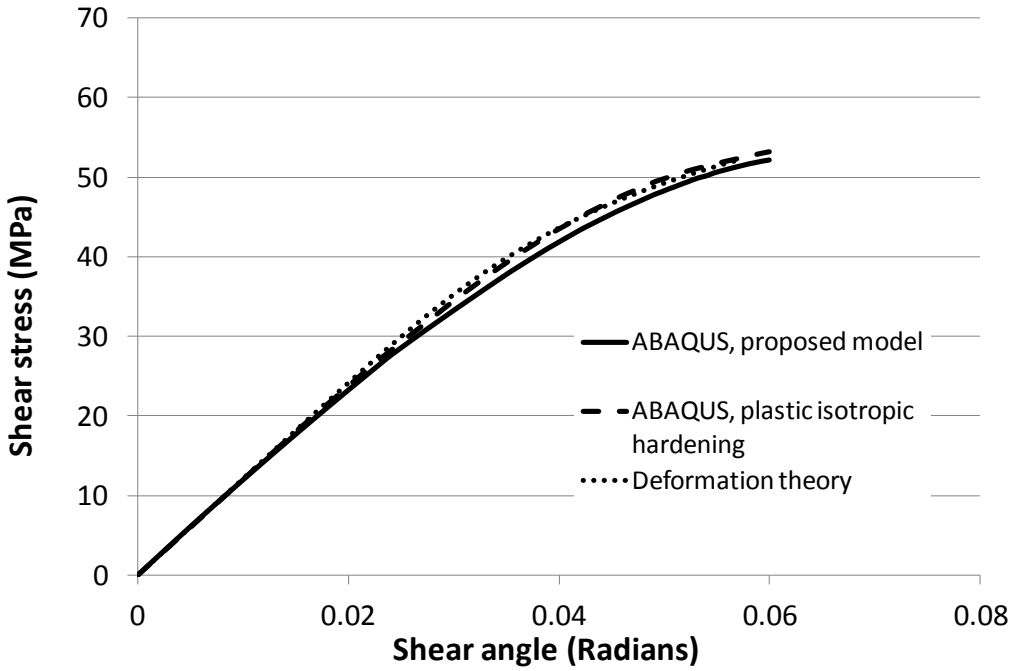

Figure 5.10: Shear stress vs. shear strain for Epikote 828 as predicted by ABAQUS using the proposed model, deformation theory, and ABAQUS using isotropic hardening

Also provided is the result for classical plastic deformation theory, as employed by Lee, *et al.* (1999) for comparisons between ABAQUS and closed form solutions. The results of Figure 5.10 show that ABAQUS matches classical plastic deformation theory for simple shear. When implemented in ABAQUS, the proposed model gives shear stress vs. shear strain response that is very similar, with a 1 to 2% reduction in shear stress at larger shear angles.

Next, the one element ABAQUS model was solicited in combined compressive and shear loadings using the assumption of plastic isotropic hardening and using the proposed model. The shear modulus at zero shear strain was predicted as a function of compressive stress, thus modeling data from Hayashi (1985), as shown in Figure 5.11. Sample No. 1 from Figure 5.7, which was quite different from the other samples, was not included.

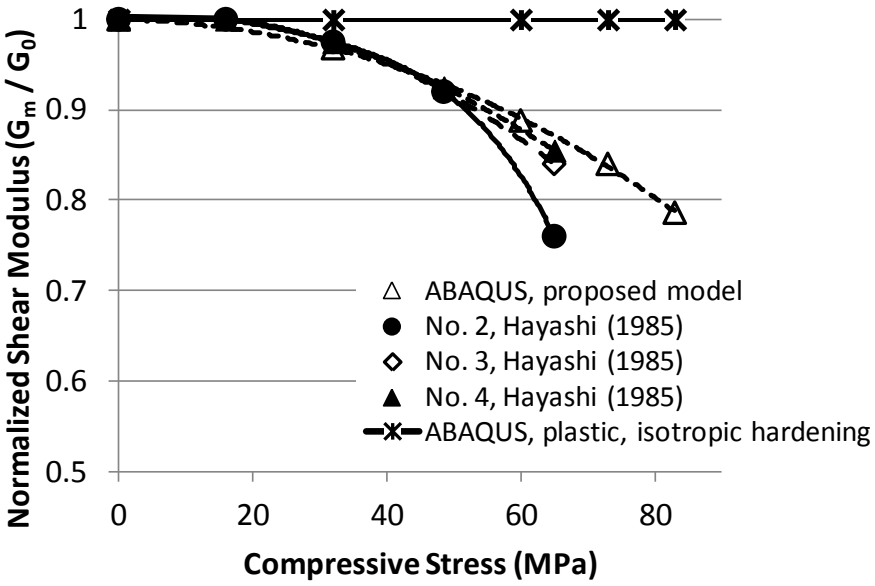

Figure 5.11: Shear modulus vs. compressive stress for Epikote 828. Measurements from Hayashi (1985), predicted by ABAQUS with proposed model, and ABAQUS with plastic isotropic hardening

With plastic isotropic hardening, no shear softening with compressive stress occurred. Using the proposed model, the element response closely tracked the experimental results. At 60 MPa, the initial shear modulus had decreased by 14%, while at 80 MPa, a 22% reduction was predicted. This was due to the increase in Poisson's ratio as well as the moderate reductions in secant uniaxial modulus as the resin ultimate strength was approached.

The relative importance of Poisson's ratio change to secant modulus change will vary depending on the non-linear character of the matrix. For this particular epoxy resin, 55% of the drop in shear modulus at 80 MPa was due to uniaxial softening, while 45% was due to the increase in Poisson's ratio.

This reduction in shear modulus with increasing compressive stress is fundamentally important for modeling shear instability. That G_{12} is directly related to matrix shear modulus, G_m, is well-known, and is shown in the widely used Halpin-Tsai equation for composite G_{12}. This is given in Equation (6) with the assumption of round reinforcement fibers.

$$G_{12} = G_m \frac{1 + \eta V_f}{1 - \eta V_f} \text{ where } \eta = \frac{\frac{G_f}{G_m} - 1}{\frac{G_f}{G_m} + 1} \qquad (6)$$

Taken with Equation (3) and Figure 10, it is apparent that compressive strength is a function of matrix compressive stress. This aspect of constituent modeling must be adequately modeled, or strength predictions may be in error.

Using this approach for matrix characterization, and the boundary condition specification presented in the prior section, 2D and 3D unit cell

ABAQUS finite element modeling was used to study parametric effects associated with fiber reinforcement.

2D and 3D FEA Modeling Results

This FEA study first models the problem Rosen considered and compares results to his prediction. Then, modeling technology is incrementally improved. Successive results are used to enhance understanding of the physics involved and model parameter sensitivities.

2D Unit Cell

Using plane stress quadratic elements (CPS8), an FE model of a 2D idealized composite was created. Boundary conditions of Figure 5.2 were used; other model geometric data is provided in Figure 5.12a. The appropriateness of model dimensions is discussed in the following points:

- Fiber element width = 10 μm. This is an approximate value for both glass and carbon fiber. Boron fiber diameter is about 100 μm.
- Model length = 2000 μm = 2 mm. Fiber length to width ratio = 200. Fiber bending stiffness is thus negligible. This physical situation exists when the free span in compression is of the order of 1 mm or higher for glass and carbon composites, and on the order of 10 mm for boron. The commonly used ASTM D6641 compression test free span is 12.7 mm; thus, the model dimensions here are appropriate for carbon, glass, and boron fibers.
- Model width = 20 μm. Effective width is infinity due to the boundary condition.

2D bifurcation analysis

With the material law approach previously defined, using Epikote 828, boundary conditions of Figure 2, glass fiber E = 73 GPa, υ=0.20, and V_f = 0.5, a linear bifurcation analysis was done with the 2D **undeformed** geometry. Mode shapes and eigenvalues are given in Figures 5.12b – d.

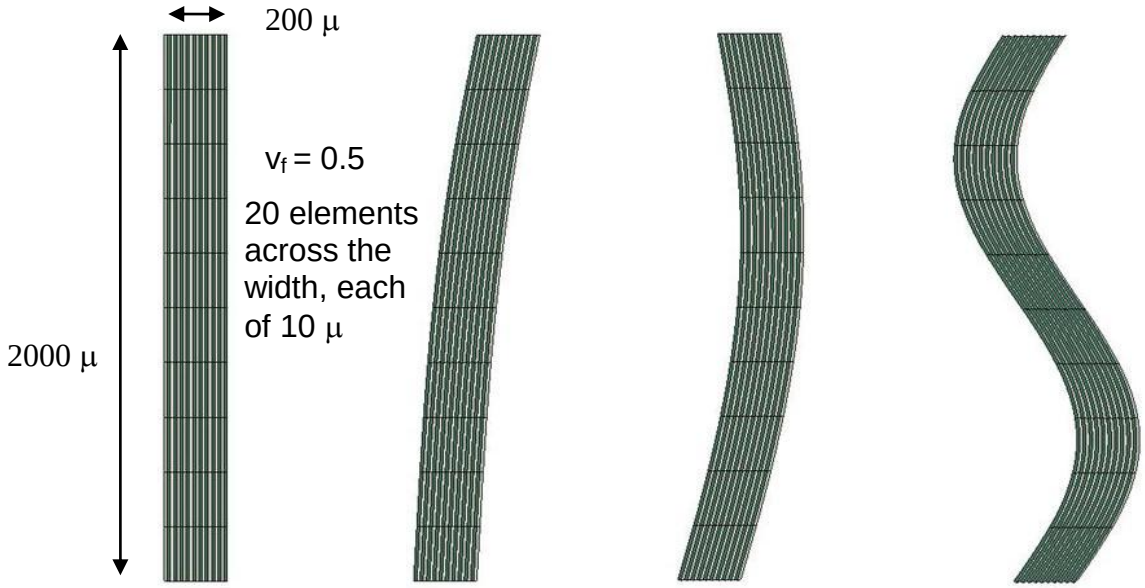

(a) undeformed (b) Mode 1 2.280 GPa (c) Mode 2 2.282 GPa (d) Mode 3 2.286 GPa

Figure 5.12: Undeformed and buckled geometries and eigenvalues for 2D model, E-glass and epoxy resin,CPS8 elements

With the matrix G_0 = 1.18 GPa and V_f = 0.50, Equation (1) gives σ_c = 2.36 GPa. The FEA prediction was 2.28 GPa, giving an agreement of **97%** with Rosen's equation. However, Rosen assumed infinite shear stiffness fibers. With properties used here, G_f = 30.0 GPa, which is high, but not infinite. Using the rule of mixtures for materials in parallel, the idealized 2D G_{12} = 2.28 MPa. Thus, with

respect to Equation (3), the FEA accuracy = **100%.** This FEA verification step may seem trivial. However, the authors have not found it in the literature. With this step, the boundary conditions previously discussed are validated.

An Euler column is a bending problem, whereas compression of a unidirectional composite is a shear problem. Figures 5.12b – d contain negligible bending stress; *each mode is a shear mode, with higher modes being assemblages of the first mode.* Associated eigenvalues are essentially identical. Plane sections do not remain plane; rather, horizontal sections remain horizontal.

Figure 5.12 showed that shear modulus decreases with compressive stress. This assures that composite shear stiffness will decrease relative to bending stiffness as compressive stress is added. It is therefore certain that the lowest eigenvalues for almost any unidirectional composite of moderate to high volume fraction will correspond to the shear mode of Figure 5.12b.

2D Riks analysis

ABAQUS offers multiple avenues for instability analysis. With the RIKS method, a step-load approach can be employed, in which load is incrementally added and the deformed geometry calculated for each load. The maximum load is achieved at the bifurcation load. Fiber alignment and modulus effects were modeled using this approach.

As shown by Cho *et al.* (2007), filament misalignment results in an imposed shear stress. This shear stress combines with matrix compressive

stress, as detailed in Chapter 3, which further increases matrix von Mises stress and thus matrix shear stiffness.

Assuming small angles, modeling fiber misalignment is simple, as the shear deformation mode is essentially linear. Rather than creating an imperfection that corresponds to a certain mode, the applied pressure can be simply represented as surface tractions in X and Y, as shown in Figure 5.13. The undeformed geometry thus remains identical for all cases.

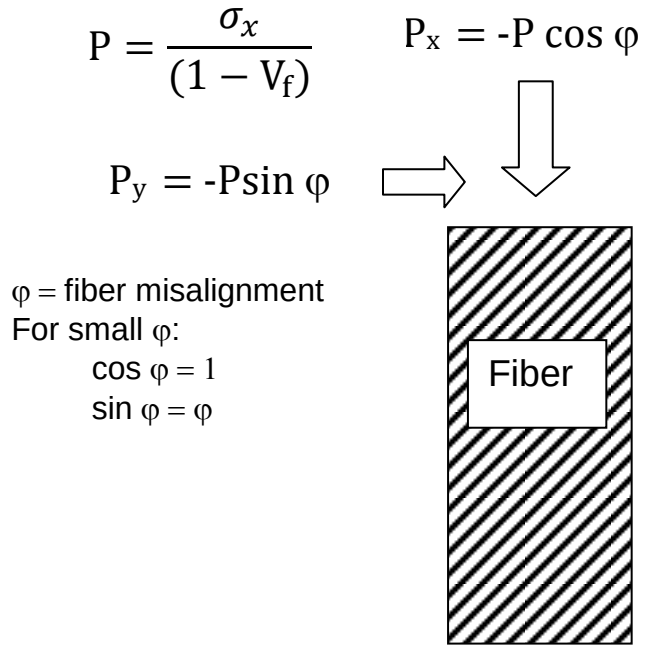

Figure 5.13: Applied load to simulate fiber misalignment Ψ, while using undeformed mesh

Using this loading method, model response to changes in fiber stiffness and misalignment was studied. Two levels of fiber extension modulus corresponding to boron (E_f = 400 GPa) and E-glass (E_f = 73 GPa) were studied across a range of misalignment levels. Results are shown in Figure 5.14.

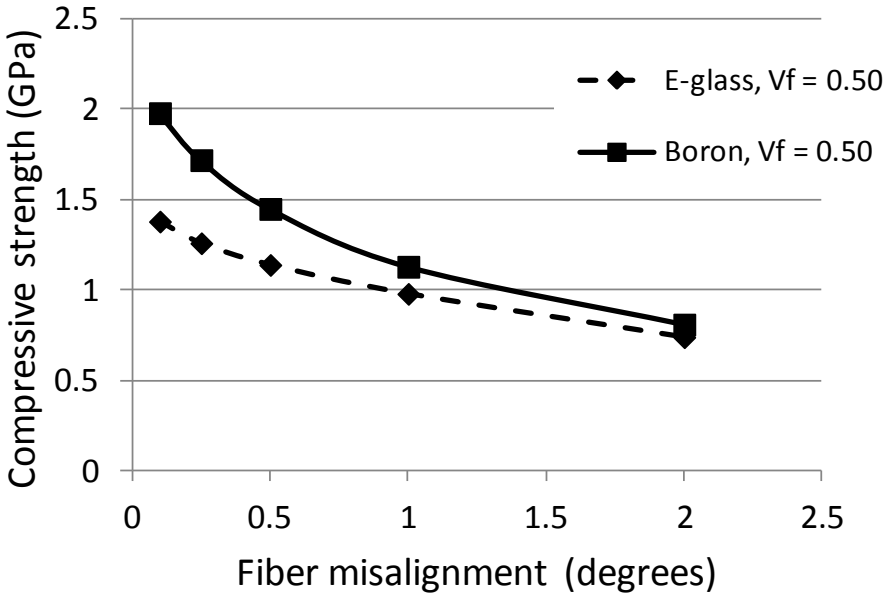

Figure 5.14: Predicted compressive strength for boron and E-glass composites with Epikote 828, $V_f = 0.5$, as function of misalignment

The 2D FEA model predicted the boron-reinforced composite compressive strength to be almost 2.0 GPa at a misalignment of 0.20 degrees. This value decreased to around 0.8 GPa with a misalignment of 2 degrees. Changing only the fiber modulus from 400 to 73 GPa, compressive strength fell to 1.4 GPa at 0.2 degrees, and to 0.75 GPa at a misalignment of 2 degrees.

As misalignment increases, the problem becomes dominated by induced shear stress, with relatively low compressive stress. For good alignment, the problem is driven by the degree of matrix compressive stress, which decreases shear modulus. Thus, boron and glass behave similarly for high misalignment, yet differently at low misalignment. In fact, the boron composite approaches 2.3 GPa at perfect alignment, which is Rosen's prediction, because the fiber strain is

small. The glass composite does not approach Rosen's prediction, because the glass fibers do strain, which results in matrix compressive stress. Rosen did not allow for reduction in matrix shear modulus as a function of compressive stress.

Boron composites with $V_f = 0.50$ and a matrix initial $G_0 = 1.2$ GPa have compressive strength of around 1450 MPa. Glass composites with $V_f = 0.50$ and a matrix initial $G_0 = 1.2$ GPa have compressive strength of around 650 MPa.[22] This simple FEA 2D linear element model suggests the improvement with boron is related to its greater compressive stiffness. This reduces matrix stress and preserves G_m/G_0. It is not directly due to the increased diameter of boron fiber. Increased fiber diameter could impact compressive strength if it resulted in better fiber alignment during composite manufacturing. This would be an indirect effect, however, and not directly related to fiber mechanical properties.

3D Unit Cell

2D idealization of the fiber/matrix composite yields Equation (1) as an estimate for σ_c. Equation (3) defines this as equal to G_{12}. It is well known that this under predicts measured G_{12} of unidirectional composites, as can be readily seen from the Halpin Tsai estimate of in-plane G_{12} given in Equation (6). For this reason, Rosen's original estimate is actually an *underprediction* of idealized compressive strength. 3D model discretization is necessary to more fully understand the phenomena at work.

3D meshing and boundary conditions

3D unit cell definition parallels the 2D unit cell definition. As shown in Figure 5.15, the 3D unit cell retains the left-right boundary treatment, thus imposing the shear mode. In ABAQUS, this was accomplished by constraint equations that tied each left side node to the corresponding right side node. Also retained from 2D is the treatment on the bottom face. Fibers are constrained such that the bottom face can rotate around the 2 axis, but not translate in the 1 direction. A plane stress condition is created in the 2 direction by fixing the rear 1-3 face, with the front face unconstrained.

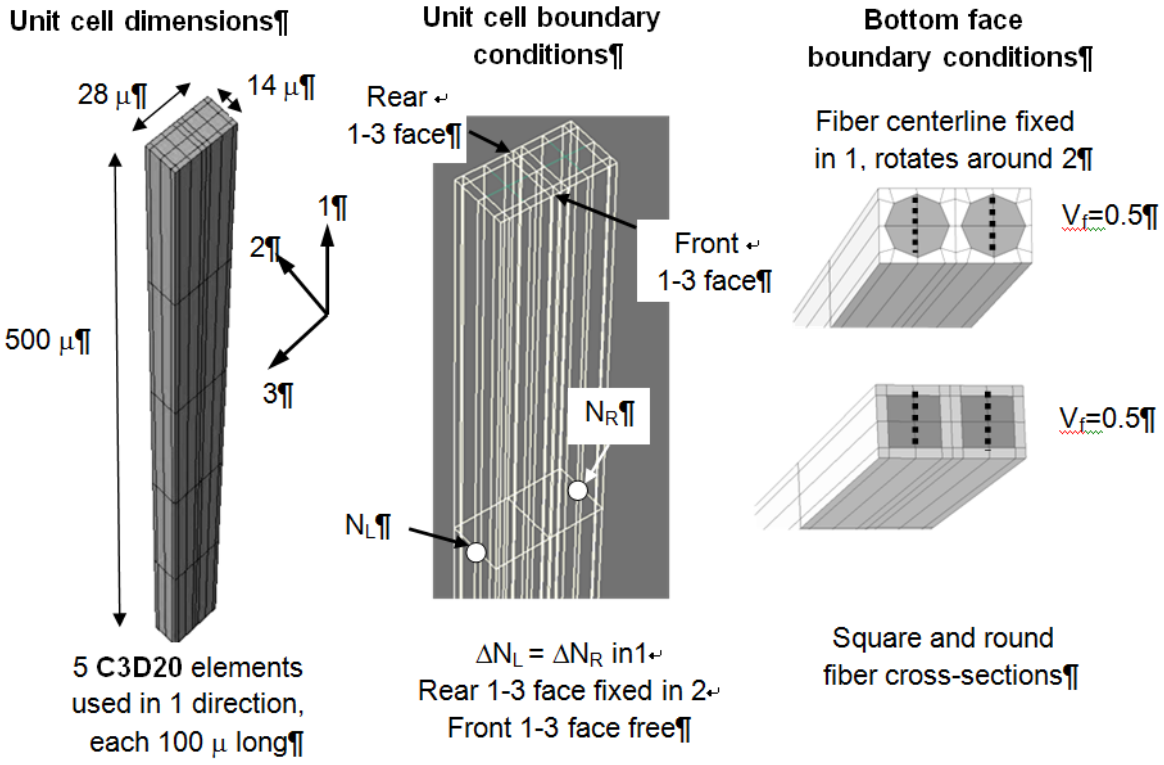

Figure 5.15: 3D unit cell definition, showing global dimensions and boundary conditions and meshing for square and round fibers

The 3D model has a length of 500 μm, compared to 2000 μm used for the 2D model. This reduction is justified by the results of the 2D analysis, which verified that all modes are essentially the shear mode, and therefore length has little effect on the results. The 3D model uses 20 node quadratic elements, C3D20, thus giving capability to predict matrix stress variations in the 2-3 plane. The boundary stresses are applied in the same manner as for the 2D model.

3D bifurcation analyses

Using a square cable array, with $V_f = 0.5$, both round and square fiber cross sections were analyzed with a linear bifurcation on the undeformed geometries. E-glass / epoxy properties were identical to those in 2D analyses. The deformed geometries and calculated eigenvalues for the first three modes are given in Figure 5.16. Multiple unit cells are shown together, thus illustrating the continuous nature of the deformation field.

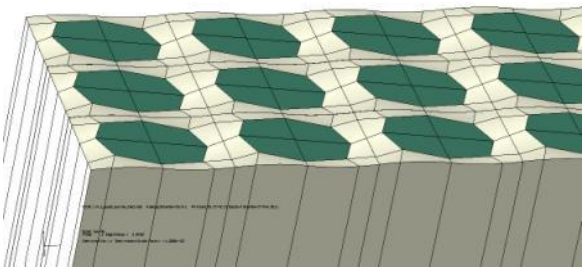

Round fiber: Mode1: 3.73 MPa
Mode 2: 3.75 MPa, Mode 3: 3.79 MPa

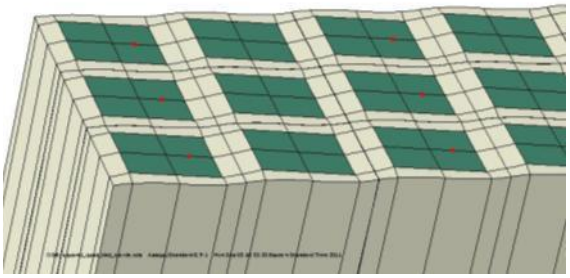

Square fiber: Mode 1: 3.66 MPa
Mode 2: 3.67 MPa, Mode 3: 3.71 MPa

Figure 5.16: 1st mode deformed geometries for square and round fibers, E-glass fibers with Epikote 828 resin, $V_f = 0.5$

Figure 5.16 shows the non-homogeneous nature of matrix deformation. The shear strain is high between cables in the 1-3 plane, yet small between cables in the 1-2 plane. While this is of little importance for this linear bifurcation analysis, it will affect matrix stress in compressive and shear loading. For this linear analysis, there is little change between square and round fiber sections. The 1st, 2nd, and 3rd eigenvalues were nearly identical, paralleling what was seen in 2D analyses. This result also validates the reduction in model length. Even higher order modes gave negligible bending contribution to the eigenvalues.

Using the Halpin Tsai relation of Equation (6), with G_m = 1.18 GPa, and G_f = 30 GPa, the composite G_{12} = 3.21 GPa. Keeping in mind that $G_{12} = G_c$, the FEA prediction is therefore about 16% stiffer than the Halpin Tsai prediction. However, Halpin Tsai tends to underpredict G_{12} of actual composites. For composites having fibers of large shear stiffness and V_f = 0.5, measured normalized G_{12} / G_0 values vary from 3.4 to 4.3[23]. Therefore, the FEA predictions fall at the low end of measured values while being slightly higher than Halpin-Tsai predictions.

This linear bifurcation analysis thus serves to validate the boundary conditions for the 3D unit cell. The predictions generally agree with other theory that predicts in-plane composite shear stiffness. It also gives a true theoretical maximum of compressive strength. While the 2D idealization gave 2.36 GPa, the 3D unit cell resulted in shear instability at 3.75 GPa. This is about a 50% increase, which is the difference between Equations (1) and (6) at V_f = 0.50.

3D Riks analyses

Bifurcation analysis of the stress-free model established that G_{12} estimates were reasonable. However, as shown with 2D modeling, actual critical stress calculation involves modeling the evolution of matrix shear modulus as compressive stress is applied. To extend this to 3D modeling, the RIKS method was employed in a manner similar to that described for the 2D case.

Using the square fiber idealization with square fiber array, 2D and 3D results were compared for boron and E-glass composites using $V_f = 0.50$. Results are shown in Figure 5.17.

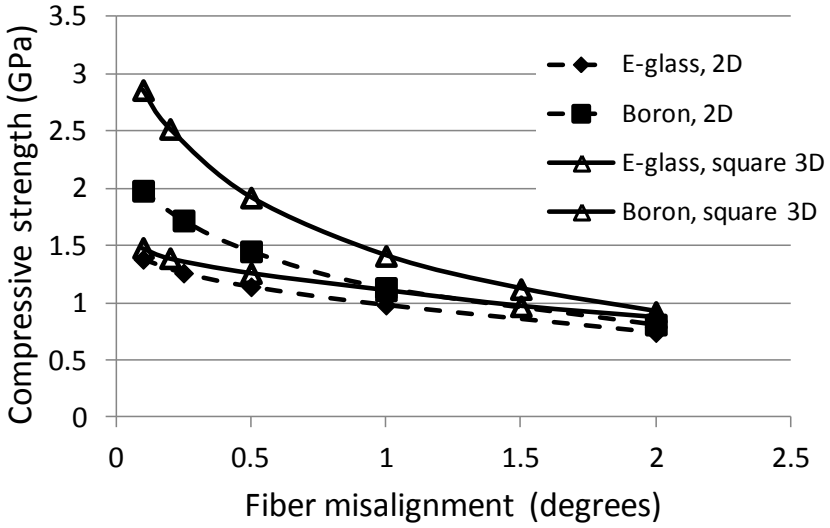

Figure 5.17: 2D and 3D predicted compressive strength for boron and E-glass composites with Epikote 828, $V_f = 0.5$, using square fiber cross section with square array for 3D idealization

The effect of moving to 3D was quite different for boron and E-glass. This is because almost all the matrix shear modulus loss of a boron composite comes from misalignment-induced shear. Because the 3D G_{12} (Equation 6) is much

higher than the 2D idealization (Equation 1) the 3D boron model has much higher compressive strength at low misalignment. The boron 3D model tends towards a compressive strength of 3.75 GPa for perfect alignment. Such is not the case for the E-glass 3D model, as the matrix looses shear modulus even at perfect alignment, due to axial shortening of the fibers. Matrix compressive stress results, and shear modulus drops. As with 2D, the problem is driven by induced shear at high misalignment, for which Boron and E-glass behave similarly.

Two fiber geometries were compared. A round cross section using a square array was modeled, and a square cross section with paired fiber array. Round and square cross section results are provided in Figure 5.18.

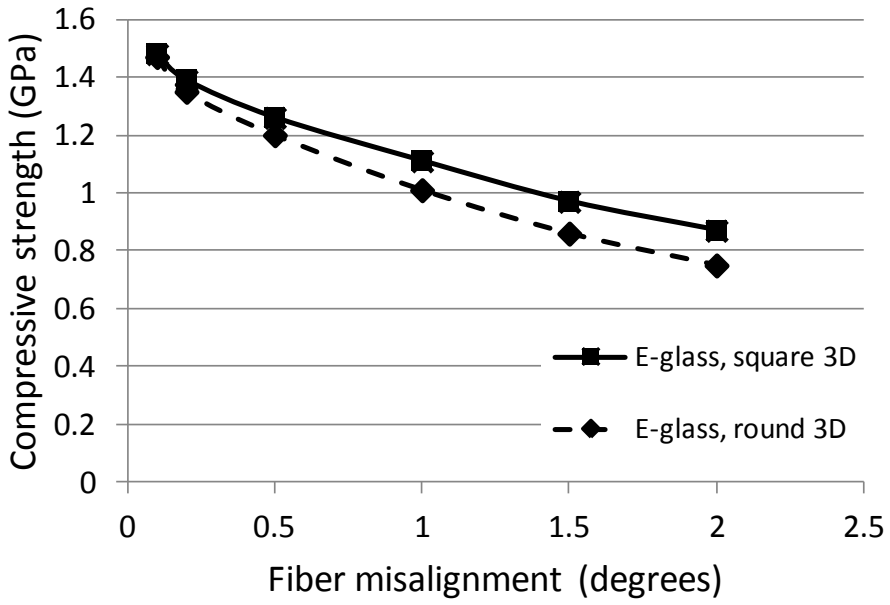

Figure 5.18: Predicted compressive strength for a range of fiber misalignments assuming square and round fiber cross sections with E-glass and Epikote 828, $V_f = 0.5$

Round and square fibers behave similarly for very low misalignment. This is to be expected, judging from the results of the bifurcation analysis previously presented. With increasing misalignment, the round fibers are more heavily penalized. The physical reason for this is best understood by postprocessing of 3D shear stress results. Figure 5.19 shows the in-plane shear stress for square and round E-glass composites with a 1 deg. misalignment, at a compressive stress of 850 MPa. At equal V_f, a round fiber in a square array results in a smaller in-plane distance between fibers than a square fiber in a square array. The result is increased matrix shear stress for a given level of compressive stress. When misalignments become large, this effect begins to be significant.

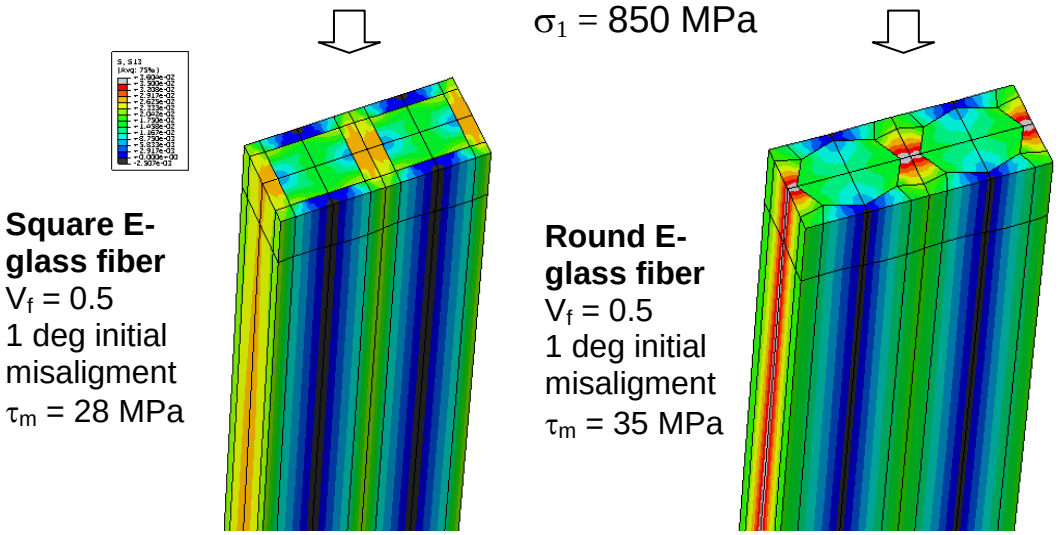

Figure 5.19: 1-3 stress for square and round fibers, σ_1=850 MPa, misalignment = 1 deg, V_f = 0.5

Finally, the effect of nonhomogeneous fiber spacing was studied by considering fiber pairing. Results are shown in Figure 5.20a. Fibers were paired in the 3 direction, as shown in Figure 5.20b. For small misalignment, the cases are identical; for larger misalignment, the paired case looses compressive strength.

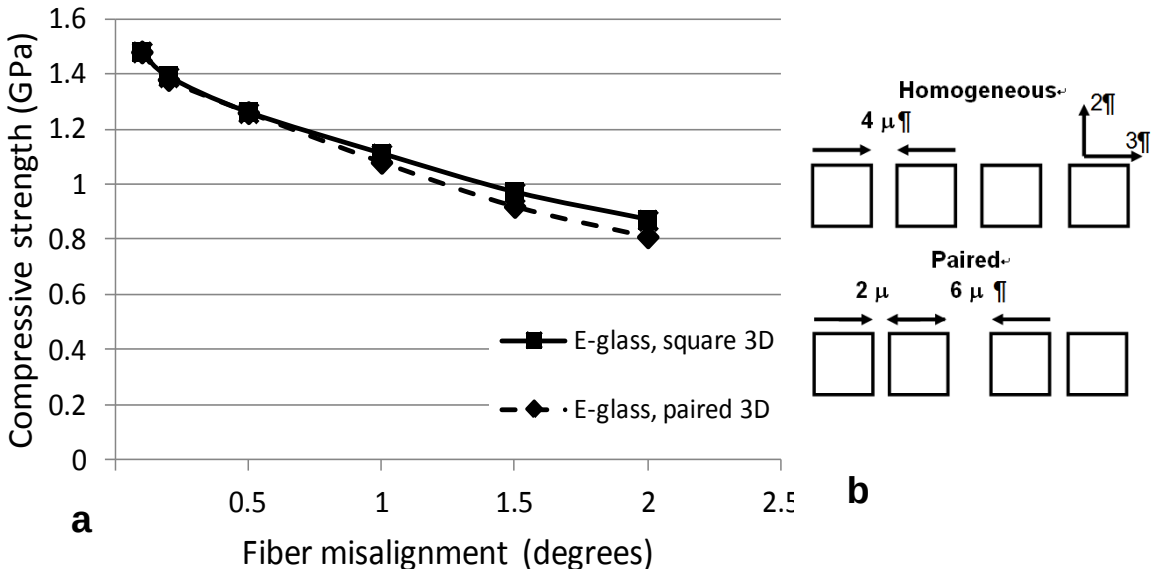

Figure 5.20: FEA Compressive strength vs. fiber misalignment for homogeneous and paired square fiber, $V_f = 0.5$

The results are similar to those noted for the comparison between square and round fiber cross sections. The physical reason for the trends is similar as well: fiber pairing results in higher non-homogeneity of the matrix shear stress at a given compressive stress. This higher stress results in a lower shear modulus, due to matrix non-linearity, which in turn increases fiber rotation. Increased fiber rotation increases in-plane shear stress for a given compressive stress, which

further reduces matrix shear modulus. 3D shear stress results are shown in Figure 5.21 for these two models at 750 MPa compressive stress, with 2 degrees of initial misalignment.

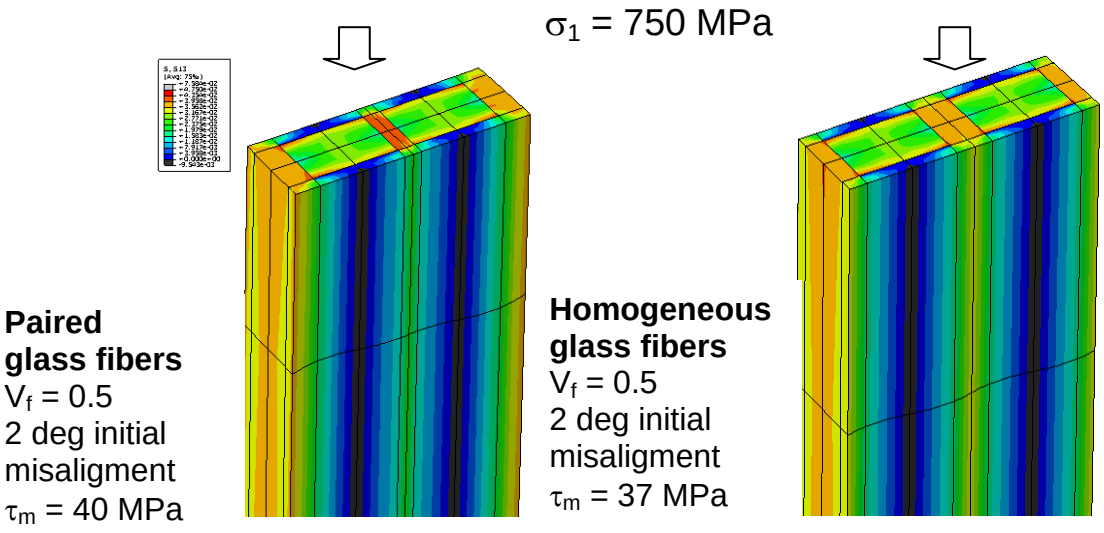

Figure 5.21: 1-3 stress for homogeneous and paired square fiber, σ_1=750 MPa, misalignment = 1 deg, V_f = 0.5

Physical realities of imperfect fiber spacing and round instead of square cross sections tend to reduce compressive strength predictions. Superimposing the effects of these physical realities, a glass fiber composite with a misalignment of 1.5 degrees is predicted to have a compressive strength of around 750 MPa. 1.5 degrees was the equivalent misalignment reported in Chapter 3 for a standard laminate glass-resin composite having V_f = 0.50. Literature values for compressive strength for such composites are around 550 to 650 MPa. However, other physical realities, such as interlaminar effects, were not accounted for in this model. These effects could be integrated using this unit cell approach, and accuracy could be further improved.

Discussion

Finite element analysis is a powerful tool. Yet, it should be viewed as only a tool, not as a substitute for engineering judgment and insight. While this study focused on the application of FEA to a specific problem, great care was taken to first correlate the modeling approach to a simple case for which the answer was known. Complexities were incrementally added, and the FEA results were examined and understood at each step.

As a result, the physics of the problem are better understood. The results underline the centrality of matrix shear modulus in compressive strength of unidirectional composites. Indeed, all the variables studied here were shown to impact compressive strength only to the extent that matrix shear modulus – and thus composite shear modulus - was affected.

While not addressed in this study, other failure criteria and modeling complexities could be considered. In addition to calculating shear instability stress, fracturing of the matrix at some threshold stress could be modeled. Unit cell definition that included other types of imperfections, such as voids, matrix modulus gradients, or interply thickness, could be considered. These would all be functions of particular processes used in composite construction.

Conclusions

1. 2D and 3D unit cell micro-mechanical finite element models have been developed that predict compressive strength of a unidirectional composite.

2. The 2D modeling approach gives exact agreement to Rosen's original equation when his assumptions are modeled.
3. 2D and 3D boundary conditions have been developed that impose a pure shear deformation on the unit cell, yet allow free in-plane fiber rotation.
4. The second and third bifurcation modes are shown to be equivalent to the first shear mode.
5. A key innovation regarding matrix material modeling has been developed. Variation of Poisson's ratio with compressive stress is included. This results in a reduction in matrix shear modulus with compressive stress. As matrix shear modulus is fundamental to this problem, this is a key innovation.
6. A parameter sensitivity study was performed that showed how and why fiber misalignment, modulus, cross section geometry, and pairing affected composite compressive stress. Any factor that resulted in greater matrix compressive strain or higher matrix stress concentration in in-plane shear tended to reduce compressive strength.

References

[1]Dow, N.F. Rosen, B.W. (1965). Evaluations of Filament-reinforced Composites for Aerospace Structural Applications, *NASA CR-207.*

2 Budiansky, B. (1983). Micromechanics. *Comput Struct,16*, 3-12.

3 Budiansky B, Fleck N.A. (1993) Compressive failure of fibre composites, *J Mech Phys Solids, 41*,183-211.

4 Daniel, I.M., Ishai, O. (2006). *Engineering Mechanics of Composite Materials, 2nd Ed*., Oxford University Press, Inc., New York, pp. 107-109.

5 Dharan, C.K.H., Lin, C.L. (2007). Longitudinal Compressive Strength of Continuous Fiber Composites, *Journal of Composite Materials*, *41*,1389.

6 Wisnom, M., (1994) Finite Element Modeling of Shear Instability under Compression in Unidirectional Carbon-Fiber Composites. *Journal of Thermoplastic Composite Materials, 7*, 352.

7 Lee, S., Waas, A. (1999) Compressive response and failure of fiber reinforced unidirectional composites. *International Journal of Fracture, 100,* 275-306.

[8] Yerramalli, C., Waas, A. (2004). The effect of fiber diameter on the compressive strength of composites – a 3D finite element-based study. *Computer Modeling in Engineering & Sciences*; *6*, 1-16.

[9] Garnich, M., Karami, G.(2004). Finite Element Micromechanics for Stiffness and Strength of Wavy Fiber Composites. *Journal of Composite Materials. 38*, 273.

[10] Thompson, R., Joesph, P., Delfino, A., Meraldi, JP, (2012) Critical Compressive Stress for Continuous Fiber Unidirectional Composites, *Journal of Composites.*

[11] Cho, J., Chen J.Y., Daniel, I.M. (2007). Mechanical enhancement of carbon fiber/epoxy composites by graphite nanoplatelet reinforcement, *Acta Materialia Inc*., Elsevier Ltd.

[12] Francescato, P.,Pastor, J., Enab, T. (2005). Torsional Behavior of a Wood-based Composite Beam. *Journal of Composite Materials,39*, 865.

[13] Alpdogan, C., Dong, S., Taciroglu, E. (2010). A method of analysis for end and transitional effects in anisotropic cylinder. *International journal of Solids and Structures, 47*, 947-956.

[14] Wongsto, A., Li, S. (2005). Micromechanical FE analysis of UD fiber-reinforced composites with fibres distributed at random over the transverse cross-section. *Composites Part A: applied science and manufacturing, 36*, 1246-1266.

[15] Xu, S., Weitsman, Y. (1996). Three-Dimensional Effects in Fiber-Reinforced Composites Under *Compression. Composites Science and Technology. 56,* 113-118.

[16] Liang Y., Liechti, K, (1994). On the Large Deformation and Localization Behavior of an Epoxy Resin Under Multiaxial Stress States**.** *International Journal of Solids and Structures, 33*, No 10, pp 1479-1500.

[17] Hayashii, T. (1985), Shear Modulus of Epoxy Resin Under Compression, *Recent Advances in Composites in the United States and Japan, ASTM STP 664*, American Society for Testing and Materials, Philadelphia, pp. 676-684.

[18] Mondragon, I., Remiro, P., Martin, M., Valea, A., Franco, M., Bellenguer, V., (1998) Viscoelastic Behavior of Epoxy Resins Modified with Poly(methyl Methacrylate), *Polymer International, 47*, 152-158.

[19] Ericksen, R., (1976) Room temperature creep of Kevlar 49/epoxy composites, *Composites,* July Edition.

[20] O'Brien, D., Sottos, N., White, S., (2007) Cure-dependent Viscoelastic Poisson's Ratio of Epoxy*, Experimental Mechanics, 47*, 237-249.

[21] Maksimov, R., Plume, E., Jansons J. (2005) Comparative Studies on the Mechanical Properties of a Thermoset Polymer in Tension and Compression, *Mechanics of Composite Materials*, *41*, No. 5.

[22] Lo, K.H., Chim, E.S-M., (1992). Compressive Strength of Unidirectional Composites, *Journal of Reinforced Plastics and Composites, 11*, 838-96.

[23] Vasiliev, V.V., Morozov, E. (2001). *Mechanics and Analysis of Composite Materials*, Elsevier Science, pp 88-90.

CHAPTER SIX

PATENT APPLICATION OVERVIEW

This chapter shares parts of a patent application filed by Michelin Tire Corporation that is based on this work. As of the writing of this dissertation, the application had not yet published. Thus, specific solutions and associated claims have been omitted. Michelin has graciously agreed to allow the general approach and aim of this patent application to be made public.

Problem Statement and Idea for Solution

Non pneumatic tires carry load via structural means. By necessity, compressive stresses result. Precedent exists in other industries (i.e., aviation) for design of benign buckling behavior, such that compressive members buckle without yielding. Structural integrity is maintained even in the post-buckling regime, with no permanent damage sustained by the structure.

In the Michelin Tweel™ Tire a circumferential beam develops contact patch stress via a shear layer encapsulated by two high stiffness membranes[1]. During deflection, one member develops tensile stresses and the opposing layer develops compressive stresses. For very high deflection, two phenomena occur:

- First, as the compressive member becomes highly stressed in compression, it is prone to buckling. Practically, of course, this member is composed of elongate filaments – i.e., very thin columns. When buckling occurs, inter-

filament shear stresses are quite large, and local shear failure of the matrix (rubber or polyurethane, for example) can occur.

- Second, the contact patch becomes long, forcing the shear layer to develop excessive shear strain. Failure can occur in the shear layer.

We can add "intelligence" in the design by creating a membrane that has a lower buckling stress yet develops acceptable post-buckled material strains in the shear layer, the inter-filament areas, and in the filament itself.

Accomplishing this design goal consists of four steps:

- Developing and validating finite element modeling procedures.
- Representation of the beam structure of the Tweel™ Tire in a 2D model.
- 3D modeling of many design possibilities for intelligent membrane buckling.
- Rank improved membrane performance gains in the 2D beam model, choose best practices, and base patent application on these results.

FEA Development and Validation

In 1965 Rosen *et al*.[2] first proposed microbuckling as an explanation for the observed rather low values of compressive strength of unidirectional composites. His work was based on stability equations developed by Timoshenko[3]. Rosens's result is well-known to those familiar with compressive behavior of composites: the now well-known extensional and shear deformation modes of a composite under compression, shown in Figure 6.1.

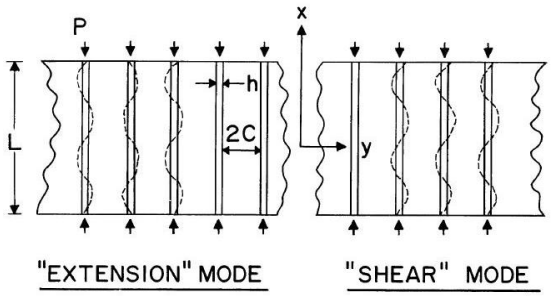

Figure 6.1: Extension and shear modes in composite buckling, Rosen (1965)

For moderately high filament volume fractions ($V_f > 0.4$), the lowest energy mode is the shear mode. Rosen's critical composite stress is:

$$\sigma_c = \frac{G_m}{1-v_f} + \frac{\pi^2 E_f}{12}\left(\frac{mh}{L}\right)^2 v_f \qquad (1)$$

where G_m = resin modulus E_f = fiber modulus

V_f = fiber volume fraction L/m = buckled fiber wavelength

Rosen then introduces a simplifying assumption: L/m (buckled wavelength) is large compared to h (fiber diameter), thus, the second term of equation 1 can be dropped. The shear mode critical stress simplifies to:

$$\sigma_c = \frac{G_m}{1-v_f} \qquad (2)$$

This analytical solution was used as a check for FEA modeling accuracy for in-plane buckling. Using Abaqus 6.9 in-plane critical compressive stress was modeled for a plane stress 2D geometry.

Mimicking Rosen's assumptions, the FEA model geometry shown in Figure 6.2 was used to model critical compressive stress. Model specifics are provided below:

- Filament diameter = 1 mm, length = 1600 mm. Thus, length >> height. Filament bending stiffness can be neglected.
- Filament modulus = 40,000 MPa
- Matrix modulus = 40 MPa, Poisson's ratio = 0.50, thus matrix shear modulus = 13.3 GPa
- Filament volume fraction = 0.5. For an aspect ratio of 1, and given material properties above, $EI/L^2 >> GA$.

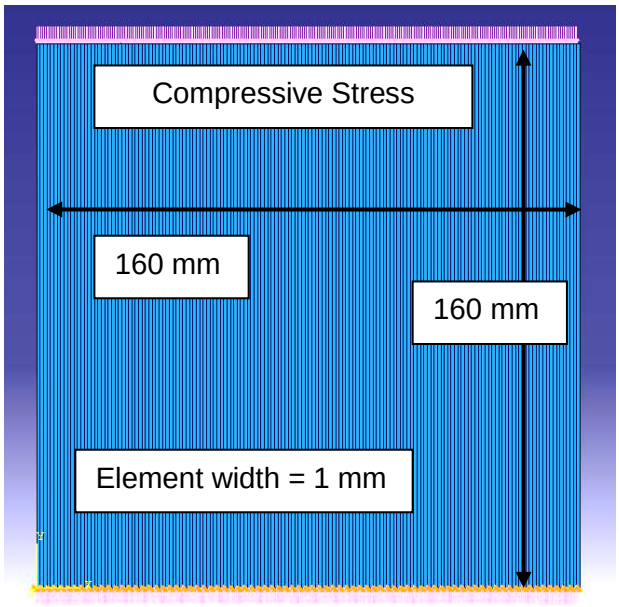

Figure 6.2: 2D Plane stress model for composite buckling

Using quadratic isoparametric elements, a linear perturbation buckling analysis was performed. The first three mode shapes are shown in Figure 6.3, along with the first three eigenvalues, which correspond to the critical

compressive stress. It should be noted that modes 2 and 3 are actually assemblages of the 1st mode, which is a shear instability mode.

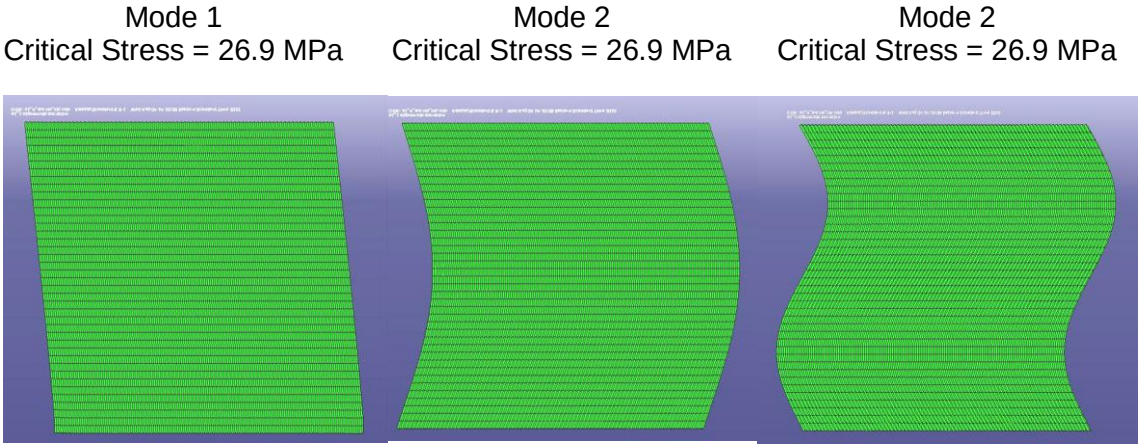

Figure 6.3: Critical stress and mode shapes

From Equation (2), the critical stress = 27.6 MPa, for an agreement of 97.5% compared to the first mode. This showed that Abaqus 6.9 was well capable of predicting in-plane buckling behavior of unidirectional composites.

To judge the ability to model out of plane buckling, a sandwich beam was constructed, with material properties and geometries shown in Figure 6.4. It was tested in a standard 4 point bending test on an Instron 5500R machine. This composite beam was asymmetrically designed such that the neutral fiber occurred close to the 30 mm wide composite plaque. The beam was then oriented in the 4 point fixture such that the 7 mm wide plaque was solicited in compression.

The 7 mm wide plaque failed at a calculated compressive stress = 420 MPa. The failed area is shown in Figure 6.5. The length of the delaminated area

was approximately 20 mm. The failure was due to a buckling event of a beam on an elastic foundation.

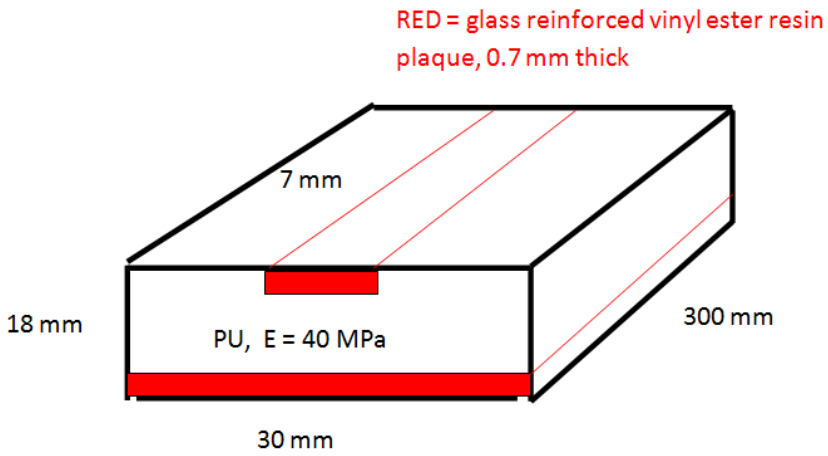

Figure 6.4: Sandwich beam design to validate out of plane buckling

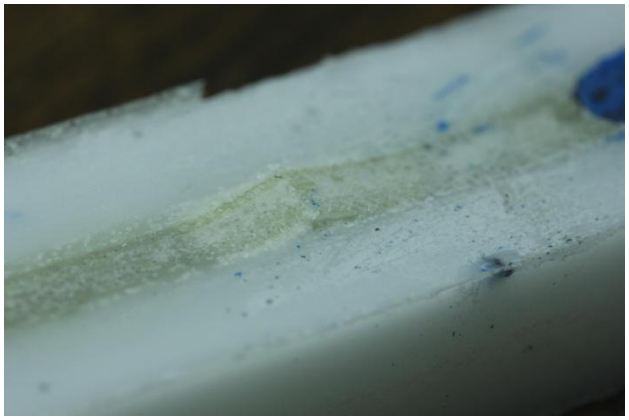

Figure 6.5: Failed area in glass-resin plaque.
Failure compressive stress = 420 MPa

The solution to this problem has been solved analytically,[4] with the general governing equation originally given by Timoshenko, *et al.* (1961) in Equation (3).

$$P_c = n^2 \frac{\pi^2 E_b I}{L^2} + \frac{kL^2}{n^2 \pi^2} \quad (n = 1,2, \ldots) \tag{3}$$

Where L = number of half sine waves to give lowest buckling load
Eb = plaque modulus
I = plaque moment of inertia
k = foundation modulus

These variables are shown in Figure 6.6 for a beam with a plaque on the top surface and a foundation modulus of k.

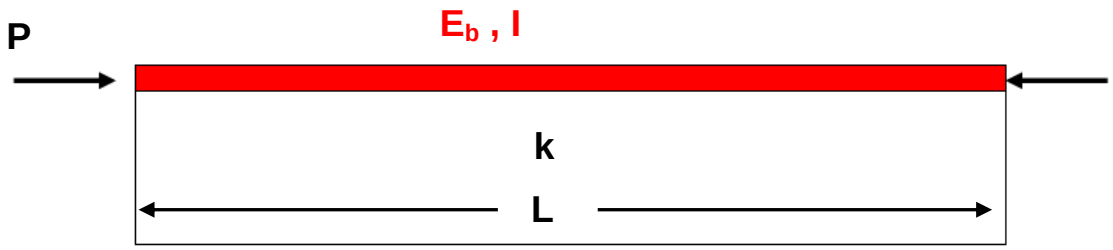

Figure 6.6: Beam design showing variables for Equation (3)

This test geometry resulted in a state of pure moment for a length of 80 mm. For this length, the flexural stress was thus constant. If this value is used for specimen length, and a half-sine distance of 20 mm is assumed, Equation (3) gives:

- P_c = 1773 N
- Stress = P_c / (0.7 x 7 mm^2) = **362 MPa,** thus good agreement to experiment.

Next, a simplified 3D ABAQUS model was constructed to establish FEA accuracy for this out-of-plane buckling behavior. Quadratic elements with

reduced integration were used. Material properties of the glass composite were considered linear and isotropic (E = 40,000 MPa, Poisson's ratio = 0.3). The polyurethane was also considered Hookean and linear (E = 40 MPa, Poisson's ratio = 0.45). A simple linear perturbation buckling analysis was performed. Model geometry with the first mode deformation is shown in Figure 6.7. The buckling stress for the first mode = 380 MPa, which agreed well with both closed form and empirical results. The sinusoidal buckled wave period matched the delaminated region of the sandwich beam – approximately 20 mm for ½ period.

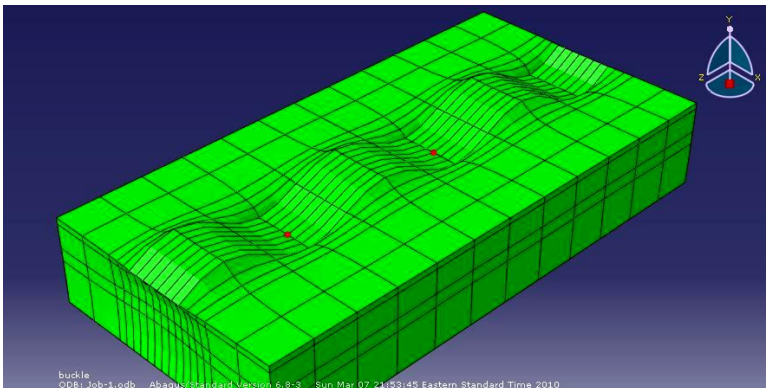

Figure 6.7: First eigenmode of beam with top plaque, σ_c = 380 MPa.

These two examples validate Abaqus 6.9 for computation of in-plane and out of plane buckling behavior of high modulus elements in an elastomeric matrix

Shear beam mechanics

The Michelin Tweel™ Tire contact region is schematically shown at in Figure 6.8. The gray portion is the shear layer, which is bounded by membranes which have high circumferential stiffness. When this curved beam – known as a "shear beam" –deforms to a flat surface, three important stress fields occur:

- Contact pressure acts on the lower surface.
- The shear layer develops shear stress, which increases with X. If the contact length is relatively small compared to the radius R_2, and if the shear layer modulus is constant, then both the shear stress and shear strain increase linearly with X.
- The two high stiffness membranes develop stress. The bottom membrane develops compressive stress and the top member develops tensile stress.

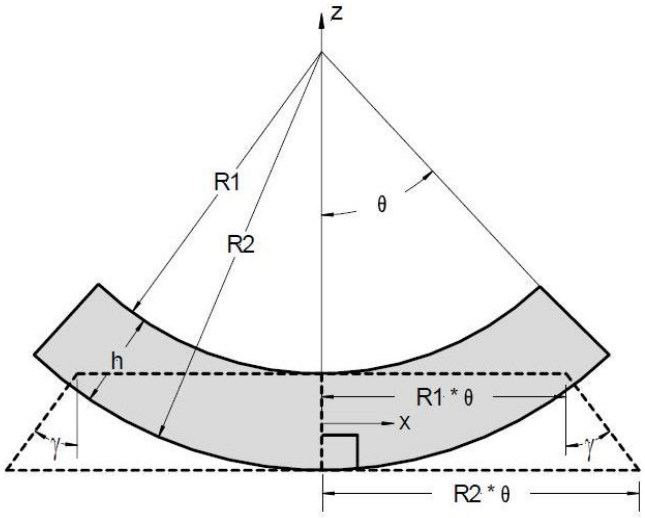

Figure 6.8: Length of a shear beam deformed to a flat surface. Top and bottom reinforcement layers are essentially inextensible; the material between the reinforcement must shear to accommodate the difference in reinforcement layer lengths, Rhyne *et al.* (2006)

An analogous structure will be used for this development. Instead of bending a curved beam onto a flat surface, a straight beam will be deformed onto a curved surface. This is a slightly easier problem to analyze, yet the physics of the two problems are identical. In the case of bending a straight beam onto a cylinder, the radius of the cylinder becomes analogous to the radius of the tire.

An Abaqus 6.9 model was constructed using this approach. Quadratic, isoparametric elements without reduced integration were used to mesh a straight beam. The undeformed beam dimensions and properties were:

- Shear layer thickness – 11 mm, G = 12 MPa
- Top and bottom membranes – 0.4 mm, E = 400,000 MPa
- Beam length = 150 mm
- Cylinder radius = 300 mm

The value for G represents a typical thermoset polyurethane elastomer, such as Vibrathane B-836. The E for the membrane is twice that of steel. It was set that high in order to illustrate the effect of high inextensibility.

The results in Figure 6.9 show the deformed geometry created by applying a force near the right hand side. The beam bends into contact with the cylinder. The color scale represents the level of shear strain in the shear layer.

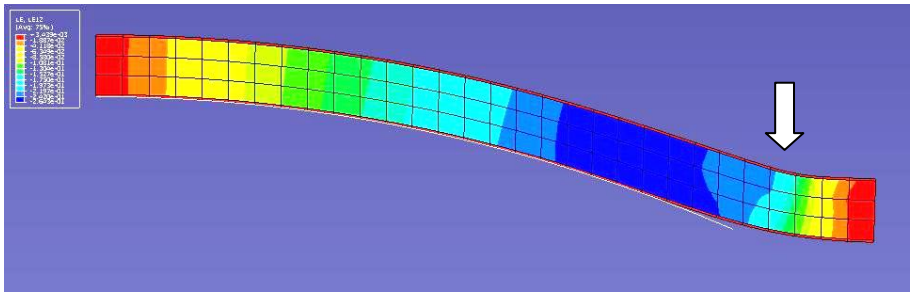

Figure 6.9: Deformed geometry and shear strain of shear beam, deformed around a cylinder with radius = 300 mm

Shear strain for this case is shown in Figure 6.10. The curve is linear until near the point at which the beam leaves contact with the cylinder. In the linear region the shear strain varies as x / R. Thus, at x = 40 mm, the shear strain is 0.13. The maximum shear strain is around 0.26, at an X value of 95 mm.

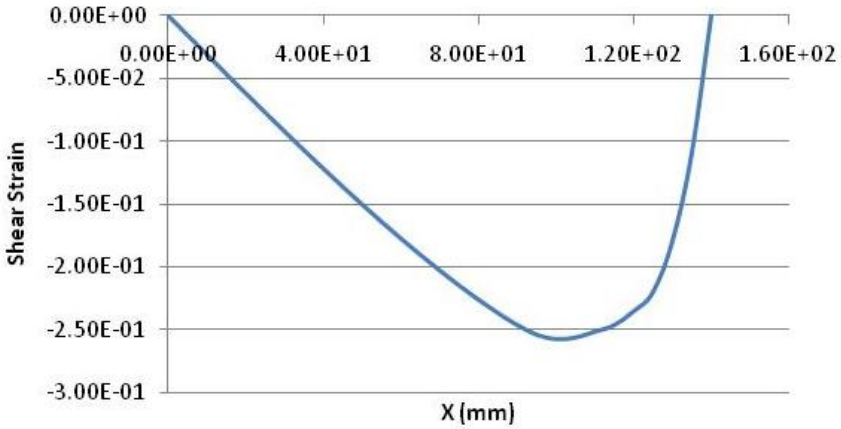

Figure 6.10: Shear layer shear strain vs. X for near-inextensible reinforcements

A thermoset elastomer such as B-836 can withstand repeated strain cycles up to a shear strain of 0.15, without permanent deformation. However, shear strains above 0.15 can result in permanent, plastic deformation. Thus, for this shear beam, a contact patch length of 90+ mm represents a severe, overloaded condition.

The predicted contact pressure for this case is shown in Figure 6.11. As disclosed in previous non-pneumatic tire patents[5], the ground contact pressure will approximately be that of Equation 4.

$$P = \frac{Gh}{R} \qquad (4)$$

where G = shear modulus of shear layer
h = shear layer thickness
R = radius to outer membrane

For this case, using values for G, h, and R previously given: P = 0.44 MPa. This value is almost attained near the beginning of contact, at x = 90 mm.

The contact pressure then slightly decreases as x=0 is approached. The reason for this is that, even with very stiff membranes, some strain occurs.

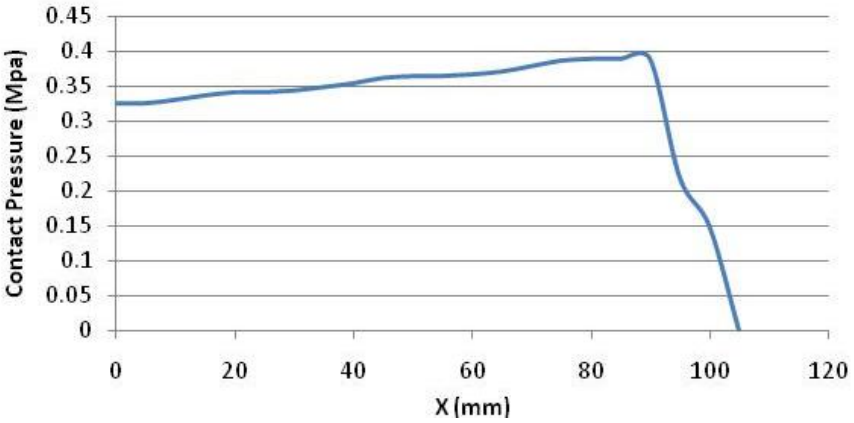

Figure 6.11: Contact pressure vs. X for near-inextensible reinforcement

Figure 6.12 shows the compressive strain in the bottom membrane as a function of x. The strain reaches -0.0027 at the contact center. While small, this strain is not negligible. If the membranes were in fact "inextensible" this strain would be zero, the contact pressure would be very close to 0.44 MPa, and the shear strain would be even higher at the edge of contact.

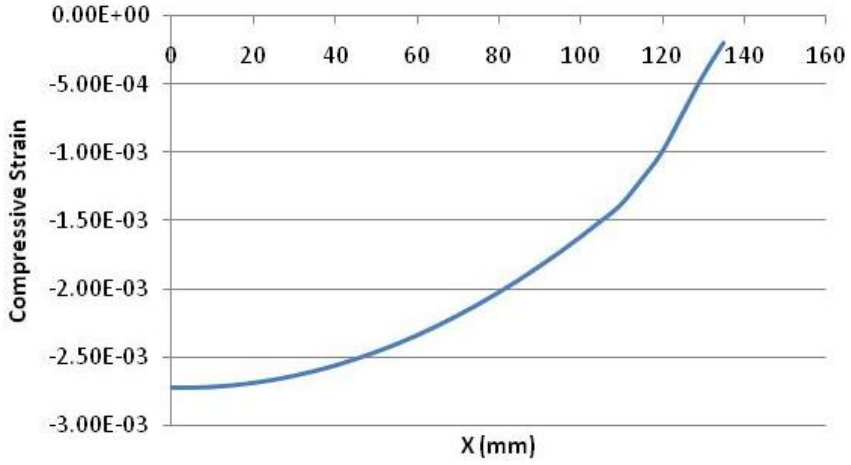

Figure 6.12: Compressive strain vs. X for bottom reinforcement

While efficient, very stiff reinforcement result in high shear in the shear layer, especially as contact patch length becomes large. An ideal reinforcement would have:

- High initial modulus up to a normal operating condition – i.e., efficient for normal use
- Low modulus at higher deflection; thus, less resulting shear in the shear layer
- Capacity for operation at high strains without plastic deformation; thus, return to normal operation after an overload or impact event.

Known materials do not have this character.

Intelligent buckling

The associated patent application disclosed several innovative structures aimed at creating a reinforcement layer that buckled at a designed compressive stress. Further, the maximum stresses inside the reinforcement after buckling was within the elastic limits of a particular glass-resin epoxy material. These structures could not be disclosed at the date this dissertation was submitted. However, the stress vs. strain character of several structures is shared, as well as the method by which this data was generated.

The base model, Model A, represents a current practice. The reinforcement layer consists of round, equally spaced filaments of diameter = 1

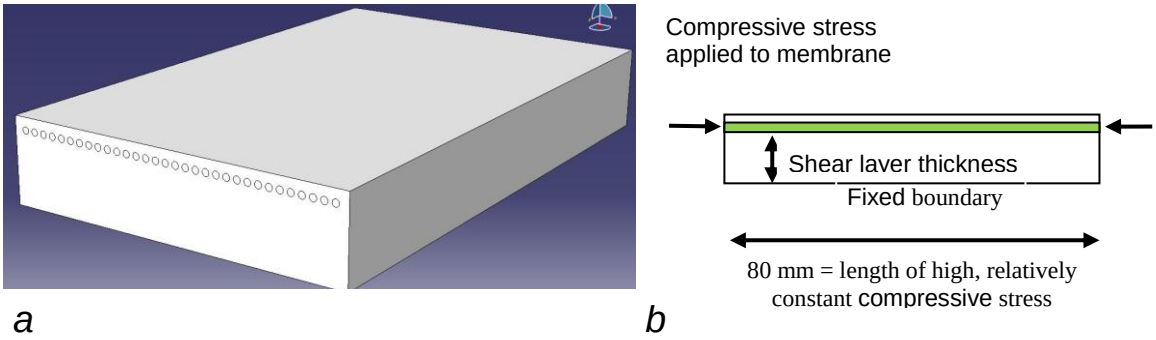

Figure 6.13: Model A geometry and boundary conditions

mm, at a pace = 1.5 mm. The reinforcement has a Young's modulus of 40,000 MPa. Model A is shown in Figure 6.13.

Using the standard linear buckling bifurcation analysis available in Abaqus 6.9, Model A was analyzed. Model length = 80 mm in X was used as this is the length over which the compressive stress maintains a relatively constant, high value. The pertinent buckling mode for Model A is shown in Figure 6.14. This analysis was done for many different reinforcement designs.

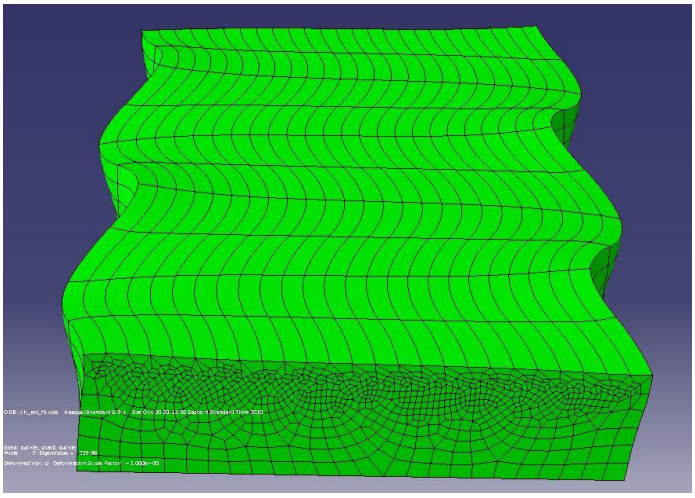

Figure 6.14: Model A geometry after bifurcation at 340 MPa

Next, the Riks method included in Abaqus 6.9 was used to model post buckling behavior. This post buckling methodology involves introducing an imperfection into a model. This imperfection is generally associated with a particular buckling mode of interest. The Riks procedure then incrementally adds a force or a stress, deforming the structure in a prescribed direction until some criterion is reached.

For this case, an imperfection corresponding to the mode previously calculated was added. The maximum imperfection was 0.5 mm, with all other node displacements scaled accordingly. The load was a compressive stress in X applied to the reinforcement. The Riks procedure then returned X displacement as a function of applied stress. Stress vs. strain results are given in Figure 6.15 for 5 reinforcement solutions, all of identical cross-section area.

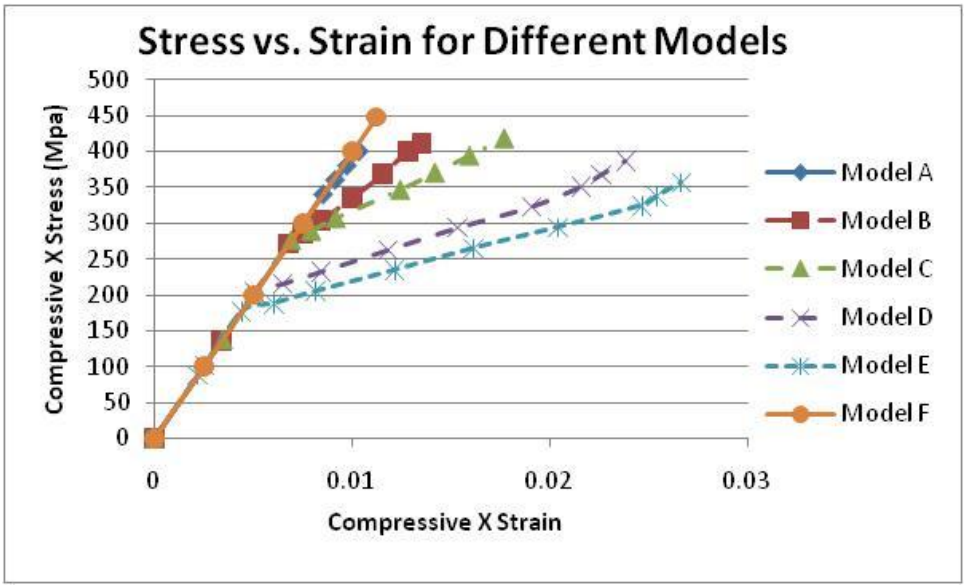

Figure 6.15: Compressive stress vs. strain for reference Model A, and 5 study solutions

Pre buckling stress, each model had the same modulus. Models A through E buckled, then exhibited very different effective compressive moduli. The buckling stress for Model F was so high that it is practically considered that this cable orientation will not buckle.

This information is also shown in Table 6.1.

Model	Pre-buckle modulus	Critical buckling stress	Post buckle effective modulus	Percent modulus reduction compared to A
A	40, 000 MPa	340 MPa	32,300	0%
B	40, 000	272	21,300	34%
C	40,000	277	13,070	59%
D	40,000	203	8,990	72%
E	40,000	177	7,320	77%
F	40,000	448	n/a	0%

Table 6.1: Buckling stress and effective post-buckle modulus

Thus, at iso reinforcement, the compressive behavior is drastically modified. Compared to Model A, Model F increased the critical buckling stress by 32%. Compared to Model A, models C through E showed reductions in effective moduli and/or reductions in critical buckling stress

This compressive behavior has a beneficial effect on shear strain. To demonstrate this, the same 2D beam model was used, as discussed in the first section. Stress vs. strain characteristics for Model A and Model E, shown in Figure 15, were used. The models were identical in extension modulus (40,000 MPA) and differed only in the compressive regime.

Shear strain vs. X is shown for models A and E in Figure 6.16. Because of the bimodulus behavior of model E, the shear strain is reduced – instead of the

shear layer straining, the membrane has buckled and the effective compressive modulus has been greatly reduced.

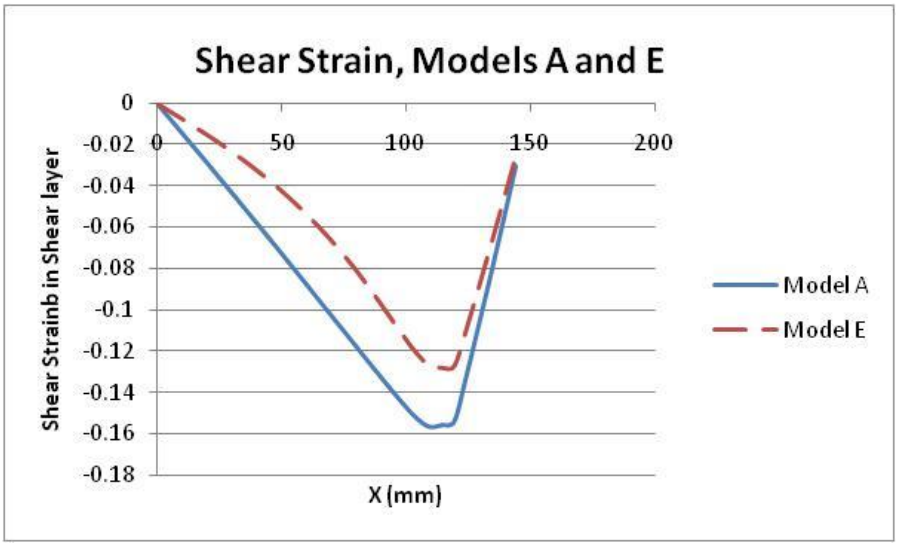

Figure 6.16: Shear strain vs. X for Models A and E

Model A shear strain maximum is 22% higher than Model E maximum shear strain – 0.16 vs. 0.13.

Polyurethanes in the family of Vibrathane B-836 can exhibit permanent deformation and greatly reduced fatigue life at shear strains above 0.15. Thus, a controlled buckling behavior of the reinforcement of the Michelin Tweel™ is a possible improvement on this design. This solution is especially advantageous, as no compromises were made for normal operation, during which no buckling would occur.

References

[1] Rhyne, T., Cron, S. (2006). Development of a non-pneumatic wheel. *Tire Science and Technology*, *vol. 34*, no. 3, pp 150-169.

[2] Rosen, B.W. (1964) Mechanics of Composite Strengthening. *Fiber Composite Materials*, American Society for Metals.

[3] Timoshenko, S. Gere, J.(1961). *Theory of Elastic Stability, 2d ed*., McGraw-Hill Book Co., New York.

[4] Sleight, D., Want, J. (1995). Buckling Analysis of Debonded Sandwich Panel Under Compression. NASA Technical Memorandum 4701.

[5] US Pat. 7201194, US Pat. 6983776.

CHAPTER SEVEN

CONCLUSIONS AND RESEARCH OPPORTUNITIES

Summary

From a global perspective, this dissertation supports and builds on the 1965 pioneering research of Dow and Rosen. This is not evident at first glance, as one main thrust of these current studies was to harmonize theoretical predictions and experimental data of the compressive strength of continuous fiber unidirectional composites. Yet, these studies absolutely support two major premises of Dow and Rosen, as follows: first, that shear instability is the deformation mode governing unidirectional composite compressive strength; and second, that the composite in-plane shear modulus is first order in determining the resistance to shear instability.

These studies add several disparate effects that influence composite in-plane shear modulus, thereby refining the model proposed by Dow and Rosen. These include matrix non-linearity, fiber misalignment, combined shear and compressive matrix stresses, thermal prestress, and a more accurate representation of the relationship between matrix shear modulus and composite in-plane shear modulus. Fundamentally, however, shear instability is still taken as occurring when the compressive stress equals the in-plane composite shear modulus. This is unchanged from Rosen and Dow's original development.

Specific Contributions

Combined Stress Model

The Combined Stress Model combines all known first order effects in computation of compressive strength of a continuous fiber unidirectional composite. Key innovations contained in the model include:

- Use of tangent matrix uniaxial modulus to calculate tangent in-plane composite shear modulus.
- Combination of matrix shear and compressive stresses to calculate matrix von Mises stress. Including matrix compressive stress is a key element, as increases in fiber modulus decrease matrix von Mises stress.
- Use of matrix von Mises stress to calculate matrix tangent uniaxial modulus, given matrix shear and compressive stresses.
- Addition of thermal effects to calculate initial matrix stress state.
- Use of step-stress methodology to calculate in-plane composite shear modulus as a function of applied compressive stress.

Accounting for Fiber Misalignment Continuum

The Combined Stress Model calculates compressive strength for a given composite as a function of uniform fiber misalignment. Then, measurement of the fiber misalignment as a cumulative volume fraction permits compressive strength calculation of a particular composite.

Compressive Strength of a Glass-resin Composite

Experimental procedures were developed that permitted accurate compressive strength measurement of a glass-resin pultruded composite. The compressive strength was measured to be 1.102 GPa, which was an average of 4 samples. This value corroborated the Combined Stress Model predictions, and represented a value of almost twice that noted in the literature for glass-resin composites of equivalent volume fraction. Glass composites are therefore shown to have the potential for very high compressive strength, provided fiber alignment is very good and the matrix has suitable mechanical properties.

FEA Unit Cell Boundary Conditions

The unit cell approach to compressive strength modeling greatly reduced model complexity and size, while enforcing the required deformation mode of pure shear. Boundary conditions applied to fiber elements permitted fiber rotation, while permitting fiber compression.

FEA Matrix Modeling

A straightforward approach for better representation of the matrix mechanical behavior was developed. Experimental studies show that the matrix shear modulus decreases with compressive stress. By accounting for evolutions in Poisson's ratio and secant matrix uniaxial modulus, the proposed method matches this experimentally observed behavior. As matrix shear modulus is first order for composite compressive strength, this is an important advancement.

Research Opportunities

At least four future research directions are suggested from the results of these studies:

- **Fatigue properties of laminate vs. pultruded composites.**

  When a unidirectional composite is solicited in compression, fiber misalignments induce matrix shear stress. Thus, more highly aligned composites should have improved fatigue. This would particularly be true in flex fatigue, during which the outer fiber cycles under compression and tension stress. A highly aligned pultruded composite should have a much better flex fatigue than a more poorly aligned laminate composite of similar constituents. Fatigue testing of the neat resin would supply data necessary to model fatigue difference as a function of fiber misalignment, and results could be compared to experimental measurement.

- **Sub-limit composite damage as function of misalignment**

  The pultruded composite in this study was measured and predicted to fracture abruptly and completely under pure compression. Conversely, a significant percentage of the laminate composite was predicted to fail prior to complete cross section failure. This process could be verified experimentally by loading a laminate composite to an elevated, yet sub-limit compressive stress, then measuring the uniaxial modulus. The drop in uniaxial modulus could be calculated from the predicted loss in intact cross-sectional area, and compared to that predicted from the method developed Chapter 3.

- **More complex finite element unit cell considerations**

  In Chapter 5, the effects of fiber spacing uniformity and fiber cross section shape were studied. A simple square fiber array was used, with constant volume fraction and homogeneous misalignment. Considerations could be expanded to include fiber volume fraction variations, fiber alignment differences within the unit cell, and the interlaminar thickness effects.

- **Additional measurements of laminate composite misalignment continuums**

  Chapter 3 developed a method for accounting for a fiber misalignment continuum, and successfully applied it to one glass-resin laminate composite. Measurement of the misalignment continuum of boron and carbon composites would be valuable, as this study hypothesized that higher fiber stiffness could improve fiber alignment. If so, then the excellent compressive stiffness of boron fiber composites would be further understood.

APPENDICIES

Appendix A

Combined Stress Model

The algorithm uses a step stress approach in which the compressive stress is incrementally applied. Variables used are as follows:

σ	= matrix uniaxial stress from tensile test
ϵ	= matrix uniaxial strain from tensile test
σ_1	= composite longitudinal stress
$\Delta\sigma_1$	= composite longitudinal step stress
σ_m	= matrix longitudinal stress
ϵ_{1mt}	= matrix longitudinal thermal residual strain
ϵ_{1m}	= matrix longitudinal strain
$\Delta\epsilon_{1m}$	= change in matrix longitudinal strain from step stress $\Delta\sigma_1$
τ_m	= matrix in-plane shear stress
σ_{vmm}	= matrix Von Mises stress
ϵ_{vmm}	= matrix uniaxial strain corresponding to σ_{vmm}
E_m	= matrix tangent extension modulus
G_m	= matrix tangent shear modulus
υ	= matrix Poisson's ratio
E_f	= linear filament extensional modulus
G_f	= linear filament shear modulus
G_{12}	= composite in-plane shear modulus
τ_{12}	= composite in-plane shear stress
φ_0	= initial in-plane filament misalignment
$\Delta\varphi$	= additional filament rotation due to shear stress
CTE_m	= matrix coefficient of thermal expansion
CTE_f	= fiber coefficient of thermal expansion
ΔT	= temperature difference between composite cure and ambient

Using the variables defined above, the following equations are equivalent to those given in the main paper, yet formulated for the step-stress algorithm used in the Combined Stress Model.

For all steps:

$$\sigma = C_1\epsilon^3 + C_2\epsilon^2 + C_3\epsilon \quad (A.1)$$

$$\frac{d\sigma}{d\epsilon} = E_m = 3C_1\epsilon^2 + 2C_2\epsilon + C_3 \quad (A.2)$$

$$\epsilon = K_1\sigma^3 + K_2\sigma^2 + K_3\sigma \quad (A.3)$$

$$G_m = \frac{E_m}{2(1+\mu)} \quad (A.4)$$

$$G_{12} = G_m \frac{1+\eta V_f}{1-\eta V_f} \text{ where } \eta = \frac{\frac{G_f}{G_m} - 1}{\frac{G_f}{G_m} + 1} \quad (A.5)$$

$$\sigma_{vmm} = \sqrt{\sigma_{1m}^2 + 3\tau_m^2} \quad (A.6)$$

At i = 0:

$$E_{m(0)} \approx E_m(\boldsymbol{\epsilon} = \mathbf{0}) \quad (A.7)$$

$$\epsilon_{1m(0)} = \epsilon_{1mt} = (CTE_m - CTE_c)\Delta T \quad (A.8)$$

$$\text{where } CTE_c = \text{composite CTE} = \frac{CTE_f E_f v_f + CTE_m E_{m(0)} v_f}{E_f v_f + E_{m(0)} v_m}$$

CTE_m = matrix CTE

CTE_f = fiber CTE

$$\epsilon_{vmm(0)} = \epsilon_{1m(0)} \quad (A.9)$$

$$\sigma_{vmm(0)} = \sigma_{1m(0)} = E_{m(0)}\,\epsilon_{1m(0)} \quad (A.10)$$

At I = 1,2,3 …, given $\Delta\sigma_1$:

$$\Delta\tau_{12(i)} = \Delta\sigma_1 \ \varphi_{(i-1)} \tag{A.11}$$

$$\Delta\varphi_{(i)} = \frac{\Delta\tau_{12(i)}}{G_{12(i-1)}} \tag{A.12}$$

$$\varphi_{(i)} = \varphi_{(i-1)} + \Delta\varphi_{(i)} \tag{A.13}$$

$$\tau_{12(i)} = \tau_{12(i-1)} + \Delta\sigma_1 \ \varphi_{(i)} \tag{A.14}$$

$$\tau_m = \tau_{12} \frac{1 - V_f(1 - \frac{G_m}{G_f})}{1 - (4V_f/\pi)^{0.5}(1 - \frac{G_m}{G_f})} \tag{A.15}$$

$$\Delta\epsilon_{1m(i)} = -\frac{\Delta\sigma_1}{V_f E_f + V_m E_{m(i-1)}} \tag{A.16}$$

$$\epsilon_{1m(i)} = \epsilon_{1m(i-1)} + \Delta\epsilon_{1m(i)} \tag{A.17}$$

$$\sigma_{1m(i)} = \sigma_{1m(i-1)} + E_{m(i-1)}\Delta\epsilon_{1m(i)} \tag{A.18}$$

Example Calculation from Combined Stress Algorithm

A step stress increment of 1 MPa gave good performance in this study. For easier data manipulation, this example uses a step stress increment of 25 MPa. A misalignment of 1.5 degrees is used, similar to the test case composite. All units are SI.

Matrix and fiber information:

- E_f = 80,000 MPa; V_f=0.50, G_f=30,000 MPa, V_m=0.50, υ_m=0.40
- ΔT = 155 C, $CTE_m = 3 \times 10^{-5}$, $CTE_f = 5 \times 10^{-6}$
- (A.1) $\sigma = -1{,}097{,}200\,\epsilon^3 + 12{,}449\,\epsilon^2 + 3500\,\epsilon$
- (A.2) $E_m = -3{,}290{,}000\,\epsilon^2 + 24{,}900\,\epsilon + 3493$
- (A.3) $\epsilon = 7.3e^{-11}\sigma^5 - 1.4e^{-8}\,\sigma^4 + 9.8e^{-7}\,\sigma^3 - 2.7e^{-5}\,\sigma^2 + 5.2e^{-4}\,\sigma$

i = 0: Initial values with $\sigma_1 = 0$:

- $\varphi_{(0)}$=1.5 deg = 0.0263 radians
- (A.7) $E_{m(o)}$ = 3494 MPa
- (A.8) $\epsilon_{1m(0)} = \epsilon_{1mt} = 0.037$
- (A.10) $\sigma_{1m(0)} = \sigma_{vmm}$ = 13.0 MPa
- (A.4) $G_{m(0)}$ = 1248 MPa
- (A.5) $G_{12(0)}$ = 3374 MPa

i = 1 $\Delta\sigma_1$ = 25 MPa

- A.11) $\Delta\tau_{12(1)} = 25 \times 0.0263 = 0.656$ MPa
- (A.12) $\Delta\varphi_{(1)}$ = 1.92E-04
- (A.13) $\varphi_{(1)} = \varphi_{(0)} + \Delta\varphi_{(1)} = 0.0264$
- (A.14) $\tau_{12(1)} = \tau_{12(0)} + \Delta\sigma_1\,\varphi_{(1)} = 0.661$ MPa
- (A.15) $\tau_{m(1)}$ = 1.463 MPa
- (A.16) $\Delta\epsilon_{1m(1)}$ = -0.0006
- (A.17) $\epsilon_{1m(1)}$= 0.0031
- (A.18) $\sigma_{1m(1)}$= 11.0 MPa
- (A.6) $\sigma_{vmm(1)}$ = 9 MPa
- (A.3) $\epsilon_{vmm(1)}$ = 0.0036
- (A.2) $E_{m(1)}$ = 3540 MPa
- (A.4) $G_{m(1)}$ = 1264 MPa
- (A.5) $G_{12(1)}$ = 3413 MPa

Etc, until $\sigma_1 > G_{12}$. Program output follows:

$\Delta\sigma_1$ = 25 MPa

σ_1 MPa	$\Delta\tau_{12}$ MPa	$\Delta\varphi$ rad	φ rad	τ_{12} MPa	τ_m MPa	ϵ_{1m}	σ_{1m} MPa	σ_{vmm}	ϵ_{vmm}	E_m MPa	G_m MPa	G_{12} MPa
0	0.000	0.0E+00	0.026	0.00	0.000	0.0037	13.04	13.04	0.0037	3494	1248	3374
25	0.656	1.9E-04	0.026	0.66	1.463	0.0031	10.95	11.24	0.0036	3540	1264	3414
50	0.661	1.9E-04	0.026	1.32	2.933	0.0025	8.83	10.19	0.0034	3540	1264	3414
75	0.666	1.9E-04	0.026	1.99	4.416	0.0019	6.71	10.17	0.0034	3540	1264	3414
100	0.670	1.9E-04	0.027	2.67	5.910	0.0013	4.59	11.22	0.0036	3540	1264	3414
125	0.675	1.9E-04	0.027	3.35	7.414	0.0007	2.47	13.08	0.0040	3540	1264	3414
150	0.680	1.9E-04	0.027	4.04	8.930	0.0001	0.35	15.47	0.0045	3538	1264	3413
175	0.685	2.0E-04	0.027	4.73	10.45	-0.0004	-1.76	18.20	0.0051	3534	1262	3410
200	0.690	2.0E-04	0.027	5.42	11.99	-0.0010	-3.88	21.14	0.0058	3527	1260	3403
225	0.695	2.0E-04	0.028	6.12	13.54	-0.0016	-5.99	24.22	0.0065	3516	1256	3393
250	0.700	2.0E-04	0.028	6.83	15.11	-0.0022	-8.10	27.40	0.0074	3497	1249	3377
275	0.706	2.0E-04	0.028	7.54	16.69	-0.0028	-10.1	30.66	0.0084	3470	1239	3354
300	0.711	2.1E-04	0.028	8.26	18.29	-0.0034	-12.2	33.98	0.0095	3434	1226	3322
325	0.716	2.1E-04	0.028	8.98	19.91	-0.0040	-14.3	37.35	0.0106	3385	1209	3279
350	0.722	2.2E-04	0.029	9.71	21.56	-0.0046	-16.3	40.77	0.0119	3326	1188	3227
375	0.727	2.2E-04	0.029	10.4	23.22	-0.0052	-18.3	44.22	0.0131	3256	1163	3165
400	0.733	2.3E-04	0.029	11.1	24.92	-0.0058	-20.3	47.71	0.0143	3177	1135	3096
425	0.738	2.3E-04	0.029	11.9	26.64	-0.0064	-22.2	51.22	0.0154	3094	1105	3022
450	0.744	2.4E-04	0.030	12.6	28.39	-0.0070	-24.0	54.75	0.0165	3008	1074	2945
475	0.751	2.5E-04	0.030	13.4	30.16	-0.0076	-25.8	58.31	0.0175	2922	1043	2868
500	0.757	2.6E-04	0.030	14.2	31.96	-0.0082	-27.6	61.88	0.0184	2835	1013	2789
525	0.764	2.7E-04	0.030	14.9	33.78	-0.0088	-29.3	65.47	0.0193	2745	980	2707
550	0.770	2.8E-04	0.031	15.7	35.63	-0.0095	-31.0	69.08	0.0203	2642	943	2613
575	0.778	2.9E-04	0.031	16.5	37.52	-0.0101	-32.6	72.73	0.0215	2510	896	2493
600	0.785	3.1E-04	0.031	17.3	39.48	-0.0107	-34.1	76.44	0.0230	2322	829	2318
625	0.793	3.4E-04	0.032	18.1	41.55	-0.0113	-35.5	80.28	0.0253	2023	722	2038
650	0.801	3.9E-04	0.032	18.9	43.81	-0.0119	-36.7	84.34	0.0287	1500	536	1535
675	0.811	5.2E-04	0.033	19.7	46.49	-0.0125	-37.7	88.92	0.0344	449	160	**474**

Table A.1: Combined Stress Model Output for Test Case, with $\Delta\sigma_1$ = 25 MPa.

Termination, because σ_1 = 675 MPa > G_{12} = 474 MPa. σ_{cr} is between 650 and 675 MPa. Accuracy and precision are improved with a smaller step size of 1 MPa.

Appendix B

ABAQUS Boundary Conditions and Material Law

Boundary Conditions

ABAQUS 6.10 supports tied node constraints. Node equations can be used that tie nodes based on individual degrees of freedom. In CAE node equation constraints can be imposed on individual nodes, surfaces, or on node sets. If imposed by surfaces, all surface nodes on the first surface are tied together with all surface nodes on the second surface. If imposed by node sets, individual nodes must be chosen in a specific order to accomplish the needs of the left-right boundary condition needed for this study. This is tedious in 3D in CAE. Finally, the node set cards must be specified as “unsorted;” otherwise, the constraints will be equally imposed on all nodes simultaneously.

In this study, this problem was solved by taking the following steps:

- Using node visualization in CAE, the nodes on the left face were copied down by hand, starting at the top back corner of the geometry, proceeding forward, then dropping down to the next node row, etc. This is shown in Figure B.1.
- Corresponding Nodes on the right face were written in the identical fashion.
- Node set cards were added to the ABAQUS data file.
- Constraint equation card was added to the ABAQUS data file.

Node set cards and constraint equations used in ABAQUS are as follows:

- Node set cards

  ***Nset, nset=left, instance=Part-1-1, unsorted**
  30,470,29,509,111,515,10,250,12,
  472,471,508,248,247, etc.
  ***Nset, nset=right, instance=Part-1-1, unsorted**
  24,408,21,374,83,378,14,255,13,
  407,375,376,258,257, etc.

- Constraint equations

  **** Constraint: Constraint-3**
  *Equation
  2
  left, 3, 1.
  right, 3, -1.

This single constraint equation then imposes the constraint independently for corresponding nodes in the left and right node set definition. The corresponding model geometry with node numbers is shown in Figure B.1.

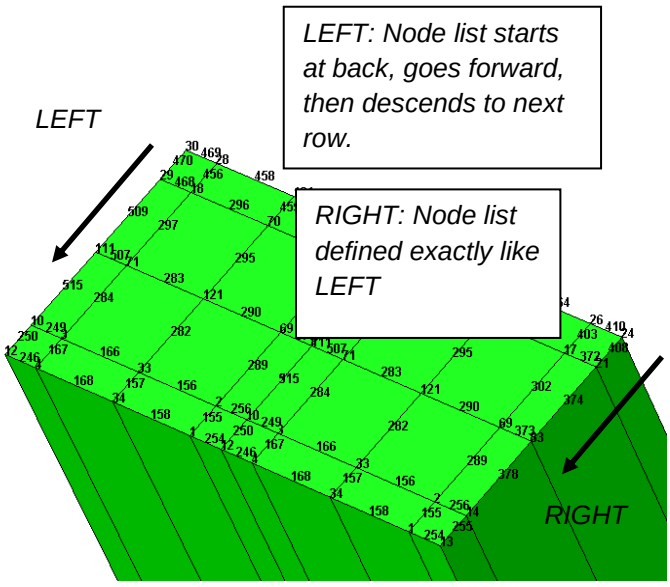

Figure B.1: Unit cell node definition corresponding to node sets

Material modeling

User subroutine

ABAQUS 6.10 requires a compiled dynamic linked library (standardU.dll) file to be placed in the working directory, or in a directory included in the environment path. The Fortran 77 source code that calculates the von Mises stress and returns it to ABAQUS to be used in the matrix material law is given in Table B.1. This file is compiled and then used to generate the dll file.

```
      subroutine usdfld(field,statev,pnewdt,direct,t,celent,time,dtime,
     1 cmname,orname,nfield,nstatv,noel,npt,layer,kspt,kstep,kinc,
     2 ndi,nshr,coord,jmac,jmtyp,matlayo,laccflg)

       include 'aba_param.inc'

      character*80 cmname,orname
      character*3  flgray(15)
      dimension field(nfield),statev(nstatv),direct(3,3),t(3,3),time(2),
     * coord(*),jmac(*),jmtyp(*)
      dimension array(15),jarray(15)

     c Get stress from previous increment
      call getvrm('S',array,jarray,flgray,jrcd,
     $     jmac, jmtyp, matlayo, laccflg)
      temp1 = (array(1) - array(2))**2
      temp2 = (array(2) - array(3))**2
      temp3 = (array(1) - array(3))**2
      temp4 = 6*( array(4)**2  + array(5)**2 + array(6)**2)
      temp5 = temp1 + temp2 + temp3 + temp4
      field(1) = sqrt(temp5 /2.0)

      return
      end
```

Table B.1: Fortran 77 code used to calculate matrix von Mises stress and return it to ABAQUS for matrix material law

Matrix material law

The ABAQUS elastic material card is used for the matrix material behavior, along with a user defined field. The values used for Epikote 828 are shown in Table B.2. The first column is the tangent uniaxial modulus; the second column is Poisson's ratio, and the third column is the von Mises stress at which the corresponding modulus and Poisson's ratio are enforced.

```
*Material, name=matrix
*Elastic, dependencies=1
   3.18,        0.3, ,          0.
   3.18,        0.3048, ,       0.004
   3.18,         0.3096, ,      0.008
   3.18,        0.31908, ,      0.0159
   3.15,        0.3378, ,       0.0315
   3.12,        0.35616, ,      0.0468
   3.05,        0.36588, ,      0.0549
   3.01,        0.372181, ,     0.060151
   2.97,        0.378406, ,     0.065338
   2.93,        0.387, ,        0.070252
  2.88,         0.395, ,        0.074802
  2.82,         0.405, ,        0.078897
  2.75,         0.413, ,        0.082537
  2.68,         0.4225, ,       0.085722
  2.59,         0.433, ,        0.088179
  2.50,         0.44, ,         0.09009
  2.42,         0.448, ,        0.091819
  2.33,         0.455, ,        0.093366
  2.26,          0.462, ,       0.094822
  2.19,         0.47, ,         0.096187
  2.12,         0.478, ,        0.097461
  2.06,         0.491, ,        0.098644
  1.99,         0.5, ,          0.099554
*user Defined Field
```

Table B.2: ABAQUS material card used for Epikote 828 mechanical behavior definition